Imperial College London

Electrochemical Studies of Semiconducting Polymers: Correlation of Energetics and Stability

Daniel Scott Beatrup

Imperial College London

Department of Chemistry

Submitted for the degree of *Doctor of Philosophy*

September 2015

The work described in this thesis was conducted under the supervision of Prof. James Durrant and Prof. Iain McCulloch at Imperial College London.

Except where specific reference is made, all the materials in this thesis are my own work. This thesis has not been submitted in whole or in part for another degree at this or any other university.

Daniel Scott Beatrup

September 2015

Abstract

In order to make organic solar cells commercially viable, it is necessary to design devices with higher efficiency and longer lifetimes than is currently accessible. Energetics of materials used in organic solar cells are already known to play a key role in various aspects of device performance, including charge generation and ambient stability. In order to make progress on either of these fronts, a clear understanding of frontier molecular orbital energy levels in semiconducting polymers is key, which is one issue that this thesis aims to address. Less understood is what role energetics plays in operational stability, which is another issue that this thesis aims to address.

Cyclic voltammetry (CV) was employed to study the effect of relative semiconducting polymer crystallinity on highest occupied molecular orbital (HOMO) energy levels in neat films. Two HOMO energy levels were found, with a difference in energy of *ca* 60 meV, corresponding to relatively ordered and disordered phases in the film. The effect of various thermal treatments on the relative ratio of ordered:disordered phases is investigated.

During solar cell operation, the semiconducting polymers are partially oxidised, with bulk hole polaron densities of *ca* $10^{15\text{-}17}$ cm^{-3}. Chronoamperometry and absorption spectroscopy were combined to develop a methodology for accelerating degradation caused by the presence of hole polarons in neat films. The methodology was initially

employed to investigate the relative stabilities of the hole polarons formed when P3HT and two structurally analogous semiconducting polymers with deeper HOMO energy levels are partially oxidised. The study was extended to include a variety of donor-acceptor polymers. It is shown that stabilising the HOMO results in a less stable hole polaron.

Contents

Acknowledgements

I should begin by acknowledging the time and support lent to me by both of my supervisors; Prof. James Durrant and Prof. Iain McCulloch. James' tireless enthusiasm and genuine curiosity for science has helped create an atmosphere that has been both inspiring and demanding, which has forced me in to being a better scientist. Iain's supportive nature and slightly laid-back approach to leading his research group made it all the more easier to feel comfortable in both an academic and social sense. Getting to this stage has not been an easy process, but it has been eased immensely by the continued support and helpful discussions from both of my supervisors, for which I would like to express my heartfelt gratitude.

I am also very thankful to Dr Laure Biniek for being my mentor and guiding me through my induction in to the lab. During our time together, Laure worked unremittingly to train me in various experimental techniques, some of which were outside of her comfort zone. Nonetheless, much of the work that has inspired this thesis would not have been made possible without the excellent support and level of discussion that Laure contributed. In addition to the support I received from Laure, I am also very thankful to Dr Stoichko Dimitrov, Dr Christian Nielsen, Dr Hugo Bronstein, and Dr Bob Schroeder for their very helpful discussion during my time at Imperial.

I had the great fortune of beginning my time in the McCulloch office at the same time as some excellent people; Pookie, Happy Hollidays, Joe'mer and the Hurhangutan to name a few. I shall look back on our many times spent together in the Holland Club, and later H-Bar, with great fondness.

I would not have made it this far without the continued support of my family, especially from my mam, dad, and grandad, for which I am eternally grateful. And last, but certainly not least, my thanks go to Jane for putting up with me during my write-up period and for getting me this far with my sanity intact – *just*.

List of figures

1

General Introduction

1.1 Motivation and background

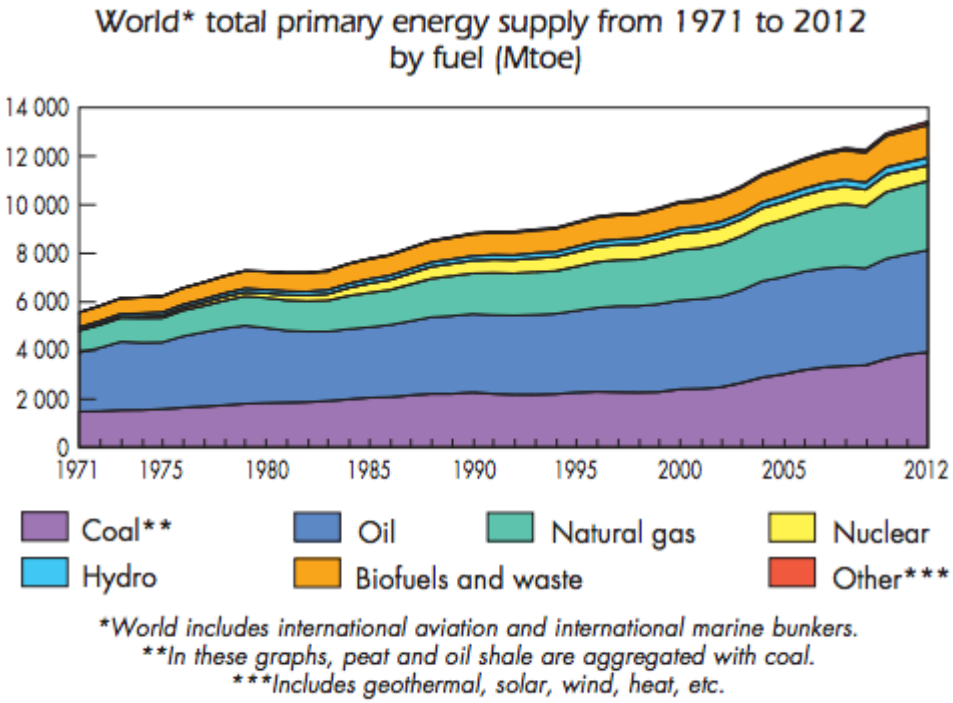

Figure 1.1[1] – Evolution of world total primary energy supply from 1971 to 2012 by fuel, measured in million tonnes of oil equivalent.

Global energy demand has more than doubled in the past 40 years, driven by a growing global population as well as economic and industrial development. More than 80% of this energy is derived from fossil fuels including oil, coal and natural gas.[1] Despite efforts to improve energy efficiency in various processes, it is likely that global energy demand will continue to grow, and thus create an energy shortfall. The technologies to be used to meet this energy shortfall are a key issue for international policymakers. The motivation to find a suitable alternative to fossil fuels is three-fold:

i) Supply – fossil fuels are a finite resource, with a significant amount of supplies located in politically unstable regions

ii) Extraction – often involves an energy-intensive process, creating water and air pollution, and destroying local environments (e.g. fracking)

iii) Combustion – many harmful gases, including greenhouse gases, are released in the combustion of fossil fuels, which may affect the health of the local population as well as contribute to global warming

One alternative technology that is growing in popularity with policymakers and the public is solar photovoltaics (PV). This is largely due to its renewability and its cleaner reputation with the environment. Figure 1.2 shows that the world cumulative installed solar capacity has grown strongly in recent years, with Asia enjoying the strongest absolute growth.

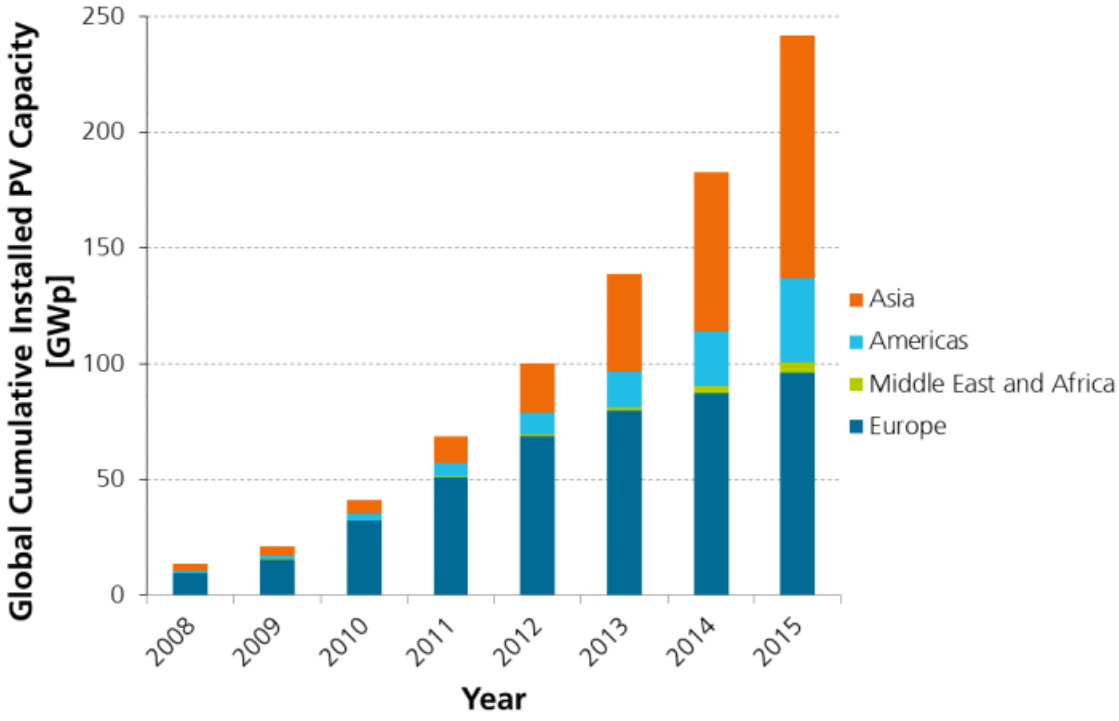

Figure 1.2 - Evolution of the Global Cumulative PV Installation until 2015. Image was taken directly from Fraunhofer report 2016.[4]

Between 2008 and 2013, the total global installed capacity increased nearly 9-fold. However, an important factor that will limit PV technologies in energy markets is its poor cost effectiveness when compared with other sources of energy. A large reason for this poor cost effectiveness is the high cost of production of crystalline silicon PV devices, which currently dominate the PV market.

Organic photovoltaics (OPVs) based on semiconducting polymers have attracted great interest in recent years, promising a low-cost PV technology. This is largely due to their potential for large scale production on a roll-to-roll basis from solution processing, producing devices that are lightweight and employ flexible substrates. The commerciality of OPV has not been lost on academic researchers or their industrial partners, where a lot of research effort has gone into improving power conversion efficiencies. The current record is held by Heliatek[5] at 12 %, which is comparable to a 14-15% cell at operational temperatures as device efficiency increases with temperature for OPV (conversely, traditional technologies, e.g. silicon, lose cell efficiency with rising temperatures). However, despite rapid progress in OPV efficiencies in recent years, it still falls short of a typical silicon-based PV (~20%). Another major issue that will have to be addressed in order to make OPV commercially viable is its device lifetime, which is also poorer than conventional silicon PV, and will form a large topic of discussion of this thesis.

1.2 Development of organic solar cells

Synthesis of the first polyacetylene film by Shirakawa et al. in 1974, and the subsequent doping studies led by Heeger and MacDiarmid, marked the dawn of the field of "plastic electronics", eventually being applied to the development of organic light emitting diodes (OLEDs), organic field-effect transistors (OFETs) and organic photovoltaics (OPVs).[6-9] The earliest OPV devices comprised a single organic layer sandwiched by two electrode materials of different work functions, thereby creating a built-in potential, which achieved very low efficiencies of <0.1%.[10,11] These poor efficiencies can be largely explained by the photocurrent generated, arising from poor exciton dissociation in an inadequate built-in potential.

The first breakthrough in organic solar cell architecture came in 1986 when Tang reported the use of a bilayer heterojunction, achieving device efficiencies of *ca* 1%.[12] This bilayer heterojunction benefits from donor and acceptor materials being stacked together, improving dissociation of those excitons formed in close proximity to the donor-acceptor (D-A) interface. Photon absorption is limited by the thickness of this bilayer, which is in turn limited by the exciton diffusion length of *ca* 10 nm. A thin active layer thus leads to a poor photocurrent, and therefore poor device efficiency.

The next major breakthrough in organic solar cell architecture came in 1995 from Heeger et al., through the introduction of the bulk heterojunction.[13] Here, the donor and acceptor materials are mixed together in a nanoscale blend, creating a large donor-acceptor interfacial area and resulting in a higher probability of an exciton reaching the interface and dissociating. The bicontinuous network of the bulk heterojunction gives it

a significant advantage over the bilayer structure in that it allows for a thicker active layer without compromising on the short distance needed for exciton diffusion to the interface, leading to improved photon absorption, and therefore improved photocurrent. Ideally, this bicontinuous network also allows for efficient charge carrier percolation to the electrodes, thereby maximising photocurrent generation.

Another important focus of research has been the development of poly(heterocycles), one of the most important classes of which being the poly(thiophenes) (PTs). PTs have attracted a lot of interest in the research community since the 1980s, focussing on specific aspects such as their synthesis, functionalization, and applications.[14]

Power conversion efficiencies of OPV devices have since gone from strength to strength, with an inverted device based on a blend containing poly(thieno[3,4-*b*]thiophene/benzodithiophene) (PTB7) and [6,6]-phenyl C_{71}-butyric acid methyl ester ($PC_{71}BM$) achieving a certified efficiency of 9.2%, which was at that time the record.[15] Toray have since published a press release stating that they have achieved an efficiency of 10.6% using a thiophene-based polymer material blended with $PC_{70}BM$, but declined to confirm the polymer structure due to patenting reasons.[16] This thesis focusses on semiconducting polymers used in bulk heterojunction solar cells.

1.3 Principles of operation in a bulk heterojunction solar cell

Photon absorption normally occurs in the donor material (polymer) in which an electron is promoted to an excited state, forming a Frenkel exciton where an electron and an electron hole (herein referred to as a "hole") are tightly bound together by the electrostatic Coulomb force. Conjugated polymer dielectric constants (*ca* 2-4) are typically significantly smaller than those materials used in convential inorganic solar cells (e.g. silicon, *ca* 12) in which the coulombic interaction is screened.[17-19] As such, binding energies for Frenkel excitons in organic solar cells (on the order of 0.1 – 1 eV) are typically at least an order of magnitude larger than that of Wannier-Mott excitons in conventional inorganic solar cells, which limits the process of separating the electron and the hole into free charges. Electron transfer from the donor to the acceptor may occur if the exciton diffuses to the donor-acceptor interface, and is facilitated by the thermodynamic driving force provided by the energy offset of the lowest unoccupied molecular orbitals (LUMOs) of the donor and acceptor materials. Electron transfer results in a bound polaron pair, which still needs to overcome the coulombic interaction in order to separate into free charge carriers (polarons). Although the bulk heterojunction is designed to improve the efficiency of exciton quenching by the donor-acceptor interface, good photocurrent is not guaranteed.[17,20] Geminate recombination after exciton quenching is a major loss mechanism, which limits the yield of charge generation.[21-23]

1.3.1 Exciton quenching

Excitons are photoexcited states and have finite lifetimes – if an exciton is not quenched, it will eventually relax to the ground state. A requirement of exciton quenching is that the exciton is formed either at the donor-acceptor interface or close enough so that it can diffuse to the interface within its lifetime. In the case of excitons formed in the donor material, the stronger electron affinity of the acceptor material provides a thermodynamic driving force for electron transfer from donor to acceptor, and hence exciton dissociation.[24-26] A stronger (or weaker) electron affinity is equivalent to a lower-lying (or higher-lying) LUMO. Similarly, in the case of excitons formed in the acceptor material, the smaller ionisation potential of the donor material provides a thermodynamic driving force for hole transfer from acceptor to donor, and hence exciton dissociation.[27-29] A smaller (or larger) ionisation potential is equivalent to a higher-lying (or lower-lying) HOMO. Both processes require a sufficiently large energy offset between donor and acceptor in order to overcome the coulombic binding interaction. For well-designed intimately mixed polymer/fullerene blend systems, exciton quenching efficiency can approach 100%, as evidenced by photoluminescence quenching when compared with polymer neat films.[20,23,30,31] However, efficient charge transfer processes do not necessarily translate into efficient charge separation.

1.3.2 Charge separation

Charge separation was originally thought to proceed as a single step, via electron transfer or hole transfer (as discussed above). More recently, the idea that charge separation may occur through an intermediate known as the charge transfer (CT) state after exciton dissociation at a donor-acceptor interface has gained momentum. In the literature, the CT state may also be referred to as a geminate pair, a bound polaron pair, or an exciplex, which consist of an electron located on the LUMO of the acceptor, and a hole on the HOMO of the donor.[22,24,31-37] It has been suggested that this leads to a partially bound electron-hole pair in which the electron and hole have a degree of spatial separation, but are close enough to each other to still feel a significant mutual coulombic attraction and therefore cannot be described as free charges. The CT state can therefore be considered to be an intermediate between a tightly bound exciton and fully dissociated charges. Due to its very short-lived nature, direct observations of the CT state have been extremely limited.[38-40]

The mechanism responsible for charge separation in bulk heterojunction systems remains a contentious issue. One model suggests dissociation of the CT state is required before free charges can be generated. The CT state is formed with excess thermal energy and is referred to as a "hot" CT state, which can dissociate into free charge carriers if the spatial separation between the electron and hole is larger than the Coulomb capture radius.[41] If this hot CT state initially fails to separate into free charge carriers it will undergo thermal relaxation, forming a lower energy charge transfer state, which is less likely to separate into free charge carriers and more likely to undergo recombination to form the ground state.

Charge generation yield is likely to be governed by kinetic competition between charge dissociation, thermalisation, and CT state recombination. Hot excitons and CT states may be more efficient in overcoming the coulombic attraction and therefore a higher probability of generating free charges due to their excess thermal energy.[42-45] One study that supports this theory found that excitons formed directly at the interface, and therefore with minimal loss of thermal energy from diffusion, are more likely to generate charges.[22]

1.3.3 Geminate and non-geminate recombination

Recombination of electrons and holes limits the charge generation yield, and represents a loss mechanism in devices. Geminate recombination involves an electron and hole, from the same photogenerated electron-hole pair (exciton), recombining to the ground state. It is therefore referred to as a monomolecular process and proceeds on very short timescales from picoseconds to nanoseconds, often competing with charge dissociation.[17,46-49] Geminate pairs can include those still bound in a CT state, or even those CT states that have dissociated but are trapped in their respective domains.

Non-geminate recombination involves the recombination of free charge carriers originating from different excitons. The process relies on diffusion of free charge carriers to within the coulombic capture radius, and therefore proceeds on longer timescales of nanoseconds to milliseconds.

1.4 Energy level and energy gap determination in conjugated polymer films

Throughout the organic electronic community there has been much confusion around the specific meanings of the following energy gap terms: *band gap*, *HOMO-LUMO gap*, *fundamental gap*, *optical gap*, and *transport gap*. This has led to the improper use of such terminology throughout the literature. *Mind the Gap!* by Jean-Luc Bredas gives an excellent account of the intricacies that exist between the different energy gap terms.[2]

We will first consider the different energy gaps present in organic materials at the molecular level, and then build on this understanding to describe the energy gaps that apply to organic materials at the polymeric level.

The fundamental gap (E_{fund}) can be considered to be the energy difference between the ionisation potential (IP – the minimum amount of energy required to remove an electron from a molecule) and the electron affinity (EA – the amount of energy liberated when an electron is added to a molecule). Experimentally, the ionisation potential can be determined via gas-phase ultraviolet photoelectron spectroscopy (UPS), developed by David W Turner at Imperial College London and later at Oxford University.[50] The electron affinity can be determined via electron attachment spectroscopy, which can be used to determine the fundamental gap, when combined with gas-phase UPS. Computationally, various Hartree-Fock and density functional theory (DFT) methods have been developed, which can be used to compare the total energy of the N-electron ground state molecule with the total energy of the (N-1)-electron state molecule (giving an estimate for IP) or with the total energy of the (N+1)-electron state molecule (giving

an estimate for EA). In the molecular case, this difference in ionisation potential and electron affinity can also be referred to as the HOMO-LUMO gap (difference in energy between the highest occupied and lowest unoccupied molecular orbitals). Computational methods can only give an estimate for fundamental gap, the quality of which depends on the specifics of the computational method used.

The optical gap (E_{opt}) is the amount of energy associated with the lowest electronic transition accessible via single-photon absorption. This assumes that the lowest accessible transition involves the first excited state. The optical gap is often determined by considering the energy of the photon that corresponds to the onset of absorption in an absorption spectrum. Measurement of the optical gap results in the formation of an excited state, in which there is an electrostatically bound electron-hole pair, thereby stabilising both the electron and hole, which results in a narrowing of the energy gap. The fundamental gap, on the other hand, refers to the difference in energy of two ionised states, which are formed in isolation from each other and therefore are not electrostatically bound to an oppositely charged species. This difference in energy between the fundamental gap and the optical gap is referred to as the electron-hole pair binding energy, and is represented in Figure 1.3.

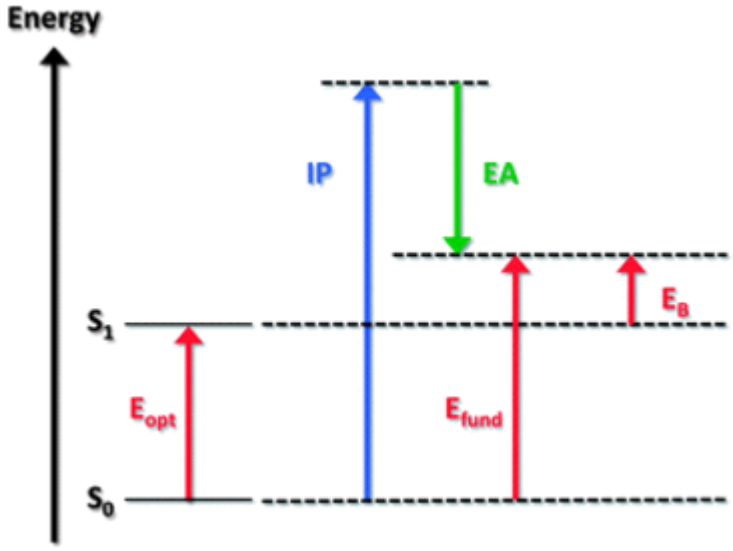

Figure 1.3[2] – Comparison of energy gaps in molecules, where S_0 is the (singlet) electronic ground state, and S_1 is the first (singlet) excited state. The difference in energy between the S_0 and S_1 states corresponds to the optical gap (E_{opt}). The difference in energy between IP and EA gives the fundamental gap (E_{fund}). The difference in energy between E_{opt} and E_{fund} gives the electron-hole pair binding energy (E_B).

In the case of organic polymers, intermolecular interactions result in a broadening of the HOMO to form a valence band (VB), as well as a broadening of the LUMO to form a conduction band (CB). Throughout literature and the wider organic semiconductor polymer community, the VB and CB of organic polymers have been incorrectly referred to as the HOMO and LUMO, respectively. Similarly, the energy gap between the VB and CB, is often interchangeably referred to as the HOMO-LUMO gap and the band gap, and sometimes both within the same communication. Whilst one intention of this section is to recognise the distinction between electronic bands and molecular energy levels, the author must confess to conforming to the increasingly "normal" practise of mixing up phraseology, and more specifically to using the terms HOMO/LUMO and bandgap to describe the electronic landscape of polymers studied in this thesis.

The band gap refers to the energy gap between the top of the VB and the bottom of the CB. In systems that are perfectly ordered, the VB and CB are typically delocalised across the entire system. Organic polymer thin films typically have some degree of disorder, resulting in some degree of localisation of the VB and CB. The degree of VB/CB localisation varies across different polymer systems and is affected by a balance between the strength of intermolecular electronic couplings, which favours delocalisation, and the extent of disorder. The transport gap refers to the minimum amount of energy necessary to create a positive charge carrier somewhere in the material (IP) minus the amount of energy gained by adding a negative charge carrier (EA) elsewhere. Hence, the transport gap can be considered to be equivalent to the band gap. Experimentally, the band gap can be determined by considering the difference in energy between the ionisation potential and the electron affinity. Similar to the molecular case, the ionisation potential can be determined with UPS. However, penetration of the incident ultraviolet radiation is limited to a depth of *ca* 10 nm. Given that the organic thin films studied in this thesis generally have a thickness of *ca* 100 nm, UPS is considered to be a surface characterisation technique, and should therefore not be considered suitable to characterise the bulk film. The surface of the film is known to exhibit energy level bending when compared with the bulk of the film, whereby the band gap widens due to a reduced capacity for intermolecular electronic coupling.[51] The electron affinity can be measured using inverse photoemission spectroscopy (IPES), and can then be combined with the IP to determine the band gap. IPES is considered to be a time-consuming and complex technique, where different measurement conditions can lead to variations in measurements for the same material. This has prompted the community to employ indirect measurement techniques for determining the conduction

band energy, including use of the optical gap, DFT and the electrochemical reduction potential.[52]

The CB energy is often inaccurately defined as the VB energy plus the optical gap. As should be evident from previous discussion and the diagram in Figure 1.3, the energy gap between the CB and the VB is equal to the optical gap plus the hole-pair binding energy. Hence, in order to accurately use the optical gap to determine the CB energy, it is necessary to also accurately know the VB energy and the hole-pair binding energy. Failure to correct for the hole-pair binding energy will result in the CB being estimated to lie too deep. It is also worth noting that this technique neglects the possibility of lower energy transitions into intermediate states.[52]

DFT estimates for CB energies of small molecules have previously been shown to have a linear fit with IPES measurements for the same molecules. DFT is therefore considered to give an accurate estimate for the conduction band of small molecules.[52] It is beneficial to have an accurate estimate of optoelectronic properties before carrying out a multistep synthesis, in order to perform preliminary screening of a target polymer.

Estimates of the CB energies of small molecules using the electrochemical reduction potential, obtained by solution cyclic voltammetry, have also been shown to have a strong correlation with IPES measurements. Solution cyclic voltammetry is therefore considered a satisfactory technique for estimating the conduction band in the solid-state.[52]

Whilst the band gap can be considered to be equivalent to the polymeric fundamental gap, it is typically much smaller than the molecular fundamental gap. Cationic and

anionic states are typically stabilised (*ca* 1 eV each) by the polarising effect of neighbouring π-conjugated molecules.

As with the case of molecular energy gaps, the polymeric optical gap is smaller than the band gap (fundamental gap). This difference in energy between the two gives the exciton binding energy, which is typically a few 0.01 eV. The exciton binding energy in a polymer thin film is notably smaller than that of a molecular electron-hole pair in the gas phase. This is explained by the stabilisation of both cations and anions by the polarisation of surrounding molecules.

1.4.1 Cyclic voltammetry (CV)

Cyclic voltammetry measures oxidation and reduction potentials of the bulk polymer film, and is not limited to the surface. It is therefore a suitable technique for characterising the oxidation and reduction potentials of the different phases present in a thin film, e.g. crystalline/aggregate and amorphous phases. A potential drawback of CV is the necessity of ionic species and solvent molecules penetrating the polymer film, which may alter morphology and therefore energetics, leading to uncertainty as to how measurements relate to the material in the absence of electrolyte solution. In addition to this uncertainty, CV does not measure the absolute energy level of molecular orbitals. However, this is deemed unimportant in this thesis as we are only interested in the relative position of MO energy levels and not their absolute values.

1.5 Overview of stability in organic solar cells

In order for a technology to become commercially viable, it must compete with the market leader on how well it performs the function it's designed to carry out, how long it can continue to function without significant maintenance, and how expensive it is. The introduction of organic solar cells was designed to reduce or remove the significant financial barrier that has restricted conventional inorganic solar cells from gaining market share in the energy market, and still holds much promise. Whilst device efficiencies of organic solar cells are still some way off those of inorganic solar cells, rapid progression of knowledge and understanding of device performance through great research efforts has led to rapid improvements in power conversion efficiencies, with the current record for a polymer solar cell at 9.2%.[15] The caveat that comes with the promises of OPV is their comparatively poor device lifetimes. Although device lifetimes have experienced vast improvements from a matter of minutes to thousands of hours, more needs to be done to improve our understanding of the various mechanisms that lead to the death of an organic solar cell.[53,54] Under controlled temperature conditions, well-encapsulated device lifetimes are estimated to be as long as 5-10 years.[53,55,56] The most effective encapsulation techniques for blocking out ambient air largely use glass, which has the disadvantage of being a bulky, inflexible material. Encapsulation of flexible organic solar cells is hitherto very limited in its effectiveness leading to device lifetimes that are far shorter than those of glass-encapsulated devices. Even with effective device encapsulation, device lifetimes of organic solar cells still lag well behind those of conventional silicon solar cells, which are typically warranted for 25 years.[57] An economic assessment of OPV electricity production carried out in 2011

helped define goalposts for device lifetime, concluding that a 10% OPV module could achieve parity with silicon PV modules after 3-4 years, or reduce the cost of electricity to approximately half of that for a silicon PV module if it managed to remain operational after 15 years.[58]

A typical bulk heterojunction solar cell with normal device architecture contains several layers, including a transparent conducting oxide (e.g. ITO) anode, a hole conducting layer (e.g. PEDOT:PSS), an active layer consisting of a polymer/fullerene blend, and a metal cathode (e.g. aluminium). Each of these layers represents a vulnerability of the device to degradation. PEDOT:PSS is a hygroscopic material containing a sulphonate group, giving it an acidic nature in the presence of water, and leading to corrosion of the ITO anode layer.[53,59] Additionally, the cathode can undergo oxidation in the presence of oxygen and water, forming electrically insulating metal oxides.[53,59] Degradation of the cathode, anode and hole transporting layers leads to reduced charge collection, resulting in a deterioration of device performance. Organic materials used in the active layer are often susceptible to photochemical, morphological and electrochemical degradation. The high temperatures associated with device operation can lead to changes to blend nanomorphology, which is important for charge generation and transport.[60] Photochemical stability is mainly concerned with the chemical degradation of active layer materials in the presence of light and oxygen.[61] The common understanding of electrochemical stability in the plastic electronics community refers to the stability of a polymer to reaction with oxygen and water (in the absence of light), and is generally limited to the storage lifetime of a material. A large focus of this thesis (in Chapters 4

and 5) will be to address operational stability from an electrochemical viewpoint, which will also be explored in the next section.

1.5.1 Electrochemical stability of conjugated polymers

1.5.1.1 Storage stability

It is well established that the highest occupied molecular orbital (HOMO) energy level of a conjugated polymer is important not just when considering how well a particular material will perform in an electronic device, but also when considering the stability of that material. A thermodynamic evaluation by de Leeuw[62] et al. considered the susceptibility of neutral p-type (and reduced n-type) organic semiconductors to undergo electrochemical reactions in the presence of oxygen and water, as a function of their ionisation potentials (and electron affinities), i.e. as a function of their HOMO (and LUMO) energy levels. By considering the standard redox potentials of oxygen and water, it is concluded that a p-type organic semiconductor must have a HOMO energy level lower in energy than -4.9 eV, in order to be stable in the presence of oxygen and water, in the absence of light. Air-stable p-type conjugated polymers have since been developed through strategies geared at lowering the HOMO of the polymer, e.g. through introduction of thiazole units along the polymer backbone.[63,64] Similarly, air stable n-type conjugated polymers have been developed through stabilisation of the radical ion formed by attaching highly fluorinated alkyl chains to the polymer backbone.[65] Given the ubiquitous nature of both oxygen and water in the atmosphere, and the lack of availability of a low-cost, flexible, and lightweight encapsulation technique, this is a very important consideration and design-rule when addressing ambient stability of

organic semiconductors. However, this approach is limited to predicting shelf-life stability as it does not address the stability of an organic semiconductor in its oxidised form in the absence of oxygen and water. Considering the impact that a steady state concentration of hole polarons will have on an organic semiconductor's physical properties will give an insight into how stable a material will be in a working device, i.e. operational stability.

1.5.1.2 Operational stability

Many studies in the literature have focussed on the operational stability of n-type polymers in organic field effect transistors (OFETs). Sirringhaus et al. measured the air stability of P(NDI2OD-T2) in OFET devices. The approach used high-resolution charge-accumulation optical spectroscopy to measure charge accumulation in the channel of an n-type OFET, and tracked the degradation of device performance in air. A shift in onset voltage to increasingly positive voltages was correlated to a reduction of charge accumulated in the polymer semiconductor, which was explained by the reaction between water, oxygen and the polymer in the accumulation layer.[66]

Similar approaches to evaluating the operational stabilities of p-type polymers have been very limited. Ruiz et al. developed a UV-vis bidimensional spectroelectrochemical approach to studying the electrochemical stability of polymer films when subjected to both p- (oxidation) and n-doping (reduction) processes.[67] Stability is investigated in a three-electrode system in deaerated solutions by monitoring normal and parallel spectroelectrochemical responses as a function of potential. Poly(4,4'-bis(butylthio)2,2'-bithiophene (PBTBT) was found to be unstable under n-doping

conditions and very stable under p-doping conditions. This study is not extensive as it only investigates the stability of one polymer, which happens to have excellent stability when oxidised. If the investigation was to be used to compare the stabilities of an extended range of polymers, one obstacle would be to ensure that each polymer is subjected to a reasonably similar level of oxidative stress.

For the majority of organic electronic devices, the organic semiconductor is partially oxidised under operation. The extent of oxidation under operation varies between different types of devices. Polaron densities ranging from $10^{15\text{-}17}$ cm^{-3} are typical for organic solar cells and organic light emitting diodes (OLEDs) whereas polaron density in OFETs can exceed 10^{18} cm^{-3} (in the surface accumulation layer). In Chapter 4, we will describe a new methodology for the evaluation of different semiconducting polymer neat films under bulk oxidative stress conditions, particularly relevant for OLEDs and organic solar cells. Furthermore, in Chapter 5 we will compare these stabilities for a range of semiconducting polymers and demonstrate how deepening the HOMO energy level leads to poorer stability of the hole polaron, which may imply poorer operational stability.

1.6 Aims and objectives

This thesis is focussed on energy level determination and electrochemical stability of semiconducting polymers in organic solar cells. The materials studied include members of the well-documented poly(thiophene) family of polymers, as well as a range of promising push-pull donor polymers. UV-vis absorption spectroscopy has been used in combination with various electrochemical characterisation techniques including cyclic voltammetry and chronoamperometry. Three motives underpin this thesis; i) to provide an improved understanding of how cyclic voltammograms of polymer neat films should be interpreted, and how they can be used to describe the valence band, ii) to expand the definition of electrochemical stability, and iii) to deduce relationships between polymer film valence band and electrochemical stability. Ultimately, the main objective of this thesis is to provide new guidelines for design rationale of new polymers with improved electrochemical stability in organic solar cells.

The electrochemical characterisation of poly(3-ethylhexylthiophene) (P3EHT) and the study of how its valence band is affected by the degree of crystallinity of a film is included in Chapter 3. The degree of crystallinity in neat films is controlled by thermal treatment, and is tracked by comparison of absorption spectroscopy with the literature. Oxidative cyclic voltammetry, coupled with absorption spectroscopy, is performed on the neat films to investigate the evolution of the valence band as a function of the relative degree of crystallinity in the film. A discussion on how this dependency of the valence band on the degree of crystallinity in a polymer neat film might affect OPV device performance is included.

Chapter 4 presents the development of a new methodology for assessing the electrochemical stability of conjugated polymer neat films. This approach presents a comparative study of the ability of a conjugated polymer to recover from the injection of a controlled concentration of positive charge carriers, across a range of polymers with different oxidation potentials. The focus of the study is in contrast to the conventional understanding of electrochemical stability of donor polymers in organic solar cells in that it refers to the operational stability instead of the storage stability. Cyclic voltammetry was used to characterise the valence band, in order to determine the oxidation potential and to understand how the positive charge carrier concentration is affected by an applied potential. Chronoamperometry was used to apply an oxidising potential in order to inject and remove a controlled concentration of positive charge carriers into the neat films, for a given time. The concentration of positive charge carriers was of the magnitude of 10^{20} cm^{-3} and therefore this study represents an accelerated ageing study. Absorption spectroscopy was used to measure how well the neat film recovered after the oxidising potential was removed, and hence its stability under oxidative stress.

Chapter 5 applies the new methodology for assessing the electrochemical stability of conjugated polymer neat films, described in Chapter 4, to an extended range of polymers. A variety of different structures were selected with a range of oxidation potentials, in order to investigate the effect of the valence band on electrochemical stability. A discussion on how this electrochemical stability might affect operational stability in an organic solar cell is included. Importantly, the predictions made in Chapter 5 regarding the impact of oxidation potential on operational stability is the

reverse for that on storage stability, and thus, in future a compromise might have to be made between storage and operational stability.

Finally, all significant results from Chapter 3-5 are summarised in the Conclusions.

2

General Experimental

This chapter will begin by describing the procedures involved in the preparation of samples, and will progress to describe the experimental techniques used in the characterisation of these samples. A key element of this thesis is the development of a new experimental methodology to probe the electrochemical stability of conjugated polymers which is employed in Chapters 4 and 5.

2.1 Sample preparation

This section gives a detailed description of the sample preparation methodologies employed in this thesis. The first part of this section outlines the preparation of neat polymer film electrodes and the second part deals with the preparation of supporting electrolyte solution for electrochemical experiments.

2.1.1 Preparation of polymer neat films

There are several different examples of conjugated polymers studied in this thesis. Electrochemical measurements were performed on polymer neat films deposited on transparent conducting oxide/glass substrate by spin-coating, which formed the working electrode (WE). A general procedure for their preparation is as follows:

1. Preparation of transparent conducting oxide/glass substrate
2. Preparation of polymer solution
3. Deposition of polymer solution on to substrate
4. Post-deposition polymer film treatment

2.1.1.1 Preparation of transparent conducting oxide/glass substrate

Glass Cutting

The transparent conducting oxide (TCO) used throughout this thesis is TEC15 fluorine doped tin oxide (FTO). This was supplied by Hartford Glass Co Inc with dimensions of 80 mm x 30 mm x 2.3 mm. Slides were cut into *ca* 12.5 mm x 30 mm substrates using a diamond glass cutter from Sigma-Aldrich and a glass-cutting clamp.

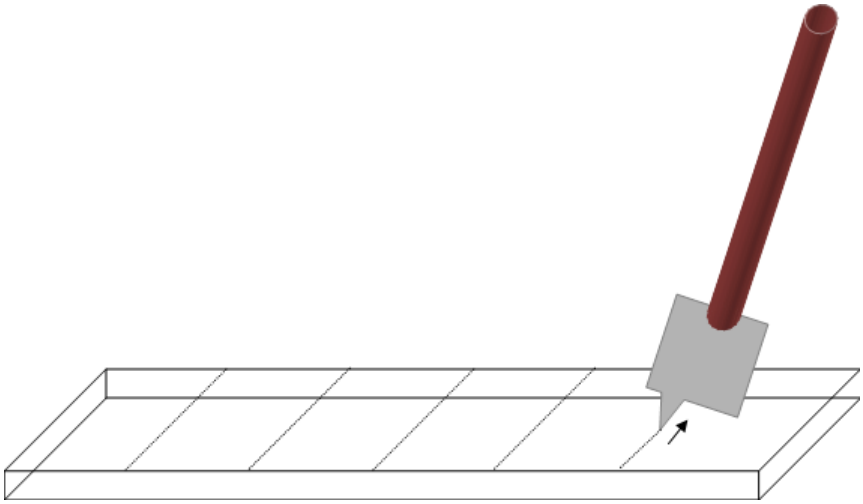

Figure 2.1 - Cutting glass. FTO glass substrate is supplied as a 2.3 x 80 x 30 mm substrate, which is cut into 2.3 x 30 x 12.5 mm substrates using a diamond glass cutter.

Glass Cleaning

Throughout the cleaning procedure, substrates were cleaned in a glass beaker with the FTO layer facing up in order to maximise the exposure of the FTO layer to the cleaning liquid.

The substrate was initially submerged in soapy water and sonicated for ten minutes. Following this, the substrate was rinsed with distilled water and then sonicated in distilled water for ten minutes, in order to remove soapy residues. The substrate was then rinsed with acetone and then sonicated in acetone for 30 minutes, in order to remove acetone-soluble impurities as well as traces of water from the substrate. The substrate was then rinsed with isopropanol and then sonicated in isopropanol for 30 minutes in order to remove impurities that may be introduced by the inferior purity of laboratory cleaning acetone. Finally, the substrate was once again rinsed with

isopropanol and then dried in an oven at 100 ^{o}C for 2 hours, in order to remove all solvent molecules.

Thin film deposition

Polymer neat films were fabricated in an inert atmosphere using a spin-coating technique. The substrate is masked on the FTO side of the substrate using tape, such that approx. half of the substrate is exposed. A polymer solution is deposited via pipette on to the unmasked area of the substrate. The substrate is then spun at 2000 revolutions per minute (rpm) for 1 minute in an inert atmosphere consisting of nitrogen. These thin films are wrapped in foil and stored under vacuum overnight to remove trace solvents.

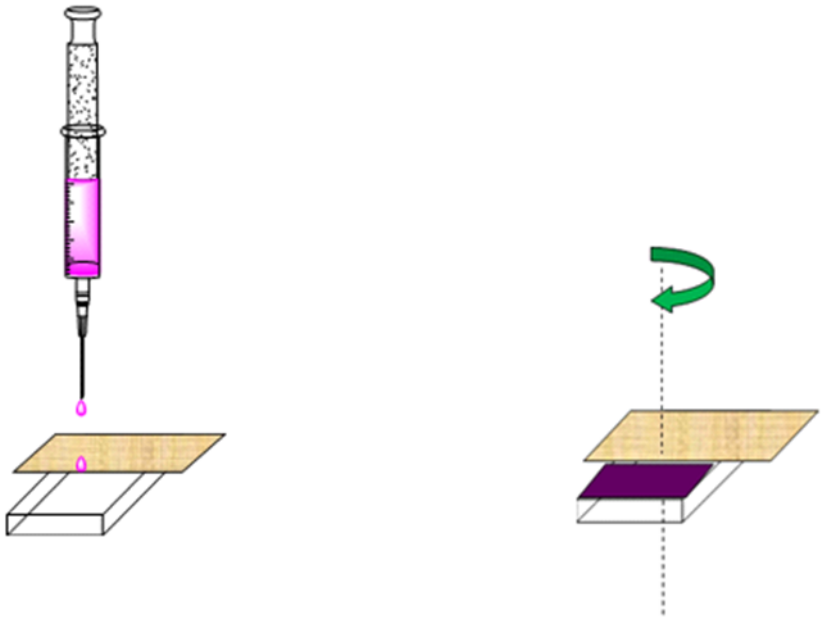

Figure 2.2 - Spin-coat procedure. Polymer solution is pipetted onto a masked FTO/glass substrate (left), and spun at 2000 rpm for 1 minute in a nitrogen atmosphere (right).

2.1.1.2 Preparation of supporting electrolyte solution

The supporting electrolyte solution used throughout this thesis was 0.1 M tetrabutylammonium hexafluorophosphate ($TBAPF_6/CH_3CN$) in dry acetonitrile. A stock solution was made up on the same day that electrochemical measurements were carried out. A description of the general procedure used to make up the solution is included, herein.

$TBAPF_6$ (9.69 g, white powder) was weighed and transferred into a clean and oven-dried round bottom flask (250 mL). The round bottom flask was then sealed using a Suba-Seal septa.

The two inlets of a Schlenck tube were connected to an argon cylinder and an oil vacuum pump. In addition, an oil bubbler was connected to the Schlenck line overflow, in order to regulate the argon pressure to produce a steady flow of *ca* one bubble per second. Meanwhile, the vacuum pump was turned on and allowed to run for 10 minutes before use, in order to allow the pump to get up to operational temperature.

A sharp needle was attached to the end of a Schlenck line and inserted into the round-bottom flask by piercing the Suba-Seal. By turning the tap on the Schlenck line to the vacuum position, a vacuum was applied to the round bottom flask for one minute. Whilst the flask was being evacuated, the contents were swirled in order to improve exposure of the contents to the vacuum. By turning the tap on the Schlenck line to the argon position, argon was reintroduced into the flask. Great care was taken not to blow the powdered contents up the walls of the flask. After flushing the flask with argon for

ca one minute, the flask was taken through two further cycles of evacuation and argon flushing.

A clean and oven-dried volumetric flask (250 mL) was sealed with a Suba-Seal septa. A long sharp needle was attached to a second Schlenck line and inserted into the volumetric flask by piercing its Suba-Seal. A second sharp needle was inserted into the Suba-Seal to act as an outlet needle. The argon flow was increased in order to flush the flask with argon. The long inlet needle was pushed deep into the flask in order to fill the flask with argon from the bottom-up. After flushing the flask with argon for 30 minutes, both needles were simultaneously removed.

A sharp needle attached to a third Schlenck line, as well as one end of a dry cannula, were simultaneously inserted into the Sure/Seal of a dry acetonitrile Winchester bottle, with both needle tips above the surface of the liquid. The other end of the cannula and an outlet needle were simultaneously inserted into the volumetric flask. The height of the cannula needle tip, inserted into the Winchester bottle, was lowered such that it was submerged below the surface of the liquid. A steady flow of dry acetonitrile flowed from the Winchester to the volumetric flask - increasing the argon flow resulted in an increased flow of acetonitrile. This step was most effective when the bottom of the Winchester bottle was held above the top of the volumetric flask. The acetonitrile was made up to the mark of the volumetric flask, at which point, the cannula tip position was readjusted such that it was above the liquid surface in order to stop the flow of acetonitrile. The cannula and outlet needle were simultaneously removed from the volumetric flask. The cannula and argon inlet needle were then simultaneously removed from the acetonitrile Winchester bottle.

An argon inlet needle and one end of the cannula were simultaneously inserted into the volumetric flask, with both needle tips held above the surface of the liquid. The opposite end of the cannula and an outlet needle were simultaneously inserted into the round bottom flask. The cannula needle tip was lowered below the surface of the liquid in the volumetric flask, which enabled transfer of the acetonitrile from the volumetric flask to the round bottom flask. During acetonitrile transfer, the contents of the round bottom flask were swirled to encourage the dissolution of $TBAPF_6$. This step was most effective when the bottom of the volumetric flask was held above the top of the round bottom flask.

After the acetonitrile had been transferred, the cannula and outlet needle were simultaneously removed from the round bottom flask. Then, the cannula and the argon inlet needle were simultaneously removed from the volumetric flask.

Before using the supporting electrolyte in an experiment, the solution was degassed with argon for ten minutes. This was achieved by simultaneously inserting a long argon inlet needle and an outlet needle into the round bottom flask, such that the inlet needle was submerged below the electrolyte solution and the outlet needle was held above the solution surface.

2.2 UV-visible absorption spectroscopy

Light absorption of polymer films was measured for wavelengths 300-1100 nm. The absorbance (A) is governed by the Beer-Lambert law:

$$A = -log_{10}(\frac{I}{I_0})$$

where I is the transmitted light intensity and I_0 is the incident light intensity.

Optical bandgap is determined by considering the energy of the photon corresponding to the onset of absorption in the absorption profile. Photon energy (E) is calculated using the following relationship:

$$E = \frac{hc}{\lambda}$$

where h is Planck's constant, c is the speed of light, and λ is the wavelength. In addition, vibronic structure in the absorption profile can be used to reveal the extent of polymer aggregation in the film.

All steady state ultraviolet-visible absorption spectra were measured using a Shimadzu UV-1800 spectrophotometer. The spectral resolution of the spectrophotometer was 0.1 nm. Spectra were collected using a sampling interval of 1 nm.

2.3 Electrochemistry

The materials studied throughout this thesis are all able to undergo oxidation and reduction, and are hence interesting to perform electrochemistry on. The relative ease of these redox processes and the ability of these materials to recover from these processes forms the basis of this thesis. As such, electrochemistry, often combined with optical spectroscopy, was the most frequently used probe of materials. Cyclic voltammetry (CV) and chronoamperometry (CA) were used throughout this thesis, due to their versatility and well-documented use in the literature. For convenience, all electrochemical measurements were measured in a three-electrode spectroelectrochemical cell. A brief description of the three-electrode spectroelectrochemical cell is given, below, followed by a more detailed review of the electrochemical techniques used.

2.3.1 The three-electrode spectroelectrochemical cell

The three-electrode spectroelectrochemical cell (see Figure 1.6) consists of a working electrode (WE), a counter electrode (CE), and a reference electrode (RE). An Autolab PGSTAT101 potentiostat was connected to the three electrodes in order to (i) control the potential applied to the WE relative to the RE (herein referred to as WE potential) and (ii) to measure the current that flows between the WE and CE.

The WE in this set-up is formed of an FTO substrate coated with a semiconducting polymer film, and is positioned such that it is parallel to, and directly between, two parallel quartz glass windows. The design of the cell incorporates an optical path to allow for the simultaneous tracking of the sample's optical properties during

electrochemical measurements. In addition, a cell holder was constructed to integrate the cell with the UV/vis spectrophotometer, such that the sample is held securely, along the optical path of the spectrophotometer light beam, and at a constant and reproducible distance from the light source. Platinum gauze wrapped around a platinum wire formed the counter electrode. The reference electrode was chosen to be a standard Ag/AgCl ([KCl] = 3.5 M) electrode which was purchased from BDH Chemicals. All potentials are quoted to this standard, unless otherwise stated. The distance between the RE and the WE was minimised in the set-up to minimise the ohmic resistance of the solution between the two electrodes and hence to maximise the control of the potential applied to the WE.

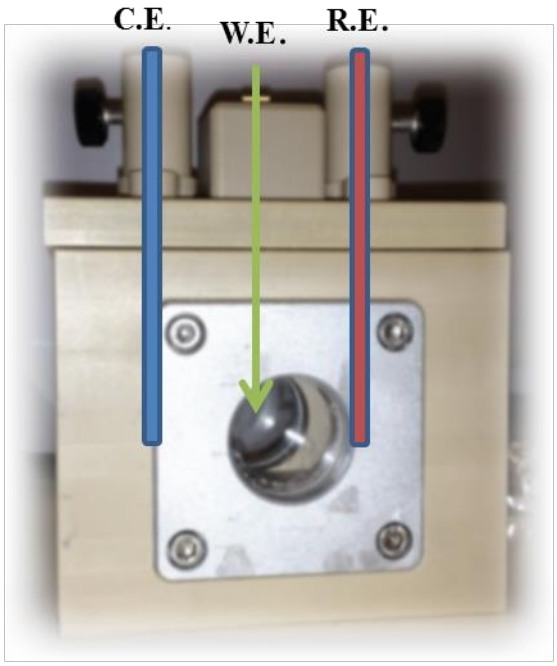

Figure 1.6 - Photograph of spectroelectrochemical cell, with electrodes drawn in for illustration purposes: The blue-fill electrode, labelled C.E., represents the counter electrode; the red-fill electrode, labelled R.E. represents the reference electrode; the green arrow represents the working electrode. The green arrow-head represents where the polymer substrate is held between the circular quartz windows; the green arrow tail represents where the working electrode is attached to the potentiostat.

2.3.2 Electrochemical techniques

2.3.2.1 Cyclic voltammetry (CV)

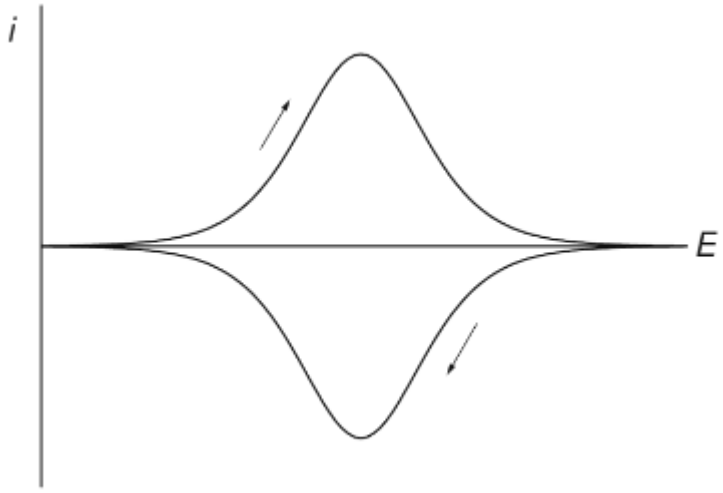

Figure 1.7[68] – Cyclic voltammogram of an ideal Nernstian electron transfer where the analyte is adsorbed on the electrode surface, where *i* is the current and *E* is the applied potential. The oxidation and reduction peaks are symmetrical and occur at the same potential in each direction. The arrows represent the direction of the potential sweep.

Cyclic voltammetry is one of the most versatile and widely applicable electrochemical techniques. It is widely used in the field of organic electronics to determine Frontier Orbital energy levels for both samples in solution and samples in film. The procedure is relatively simple and involves the use of apparatus common to most electrochemical laboratories. The technique entails the monitoring of the WE current as a function of WE potential, with respect to the RE. The WE potential is ramped, in a linear fashion, between the initial potential and a limiting potential (upper/lower), with a pre-determined scan-rate. When the WE potential approaches the formal potential of a redox active species, a current is observed, corresponding to a redox event. Specifically, scanning the WE potential in a positive direction will cause oxidation of the redox

active species, if the upper potential limit is sufficiently positive. This is indicated by a positive current. Similarly, scanning the WE potential in a negative direction will cause reduction of the redox active species, if the lower potential is sufficiently negative. This is indicated by a negative current. On reaching the limiting potential (upper/lower), the WE potential is immediately ramped in the opposite direction to a second limiting potential (lower/upper), which is the same as the initial potential throughout this thesis, i.e. 0.00 V vs Ag/AgCl. In the case of the former scenario, the oxidised species can be reduced (de-oxidised) to its initial neutral state upon reversing the potential scan direction, assuming the sample is redox stable. In the case of the latter, the reduced species can be oxidised (de-reduced) to its initial neutral state upon reversing the potential scan direction, again assuming the sample is redox stable. Plotting the resulting current as a function of WE potential produces a characteristic curve, namely a voltammogram.

Figure 1.7 gives an example of an ideal voltammogram of a reversible redox couple studied by cyclic voltammetry. The oxidation and reduction peaks are symmetrical, giving the ratio between the peak anodic and cathodic currents as unity, and occur at the same potential in each direction. Most conjugated polymers exhibit either irreversible or quasi-reversible redox couples, where there is no return current or the ratio between the anodic and cathodic currents is not unity, respectively.

Traditional cyclic voltammetry involves the analyte (redox active species under study) being dissolved in an electrolyte solution, which relies on mass transport to bring analyte materials transiently to the WE surface. However, for many semiconducting polymers, their optoelectronic properties depend strongly on whether they are in

solution or in film, and on how they have been processed. The semiconducting polymers under study, throughout this thesis, are interesting due to their potential integration as solid state films into organic solar cells. As such, all semiconducting polymers studied throughout this thesis have been studied as thin films (ca. 100 nm thick) deposited on FTO glass substrates.

As discussed in Chapter 1, many semiconducting polymers are known to be susceptible to reaction with oxygen and/or water. To limit unwanted side reactions occurring, all electrochemical measurements have been performed with an inert supply of argon being gently blown over the top of the spectroelectrochemical cell.

2.3.2.2 Chronoamperometry

Chronoamperometry uses an identical experimental set-up to the one described previously, for cyclic voltammetry, involving a WE, a CE and a RE. Current between the WE and CE is measured as a function of time, whilst applying a step potential to the WE. The initial WE potential is set such that no redox reaction of the material being studied will occur, and hence the current at this stage of the measurement should be zero. In the case of an oxidative chronoamperometry measurement, the WE potential is then increased instantaneously, such that the potential difference between the WE and the RE is sufficient to induce oxidation of the material under study. The increase in positive charge in the polymer thin film results in the migration of negative ions (PF_6^-) to the WE, and the migration of positive ions ($[NBu_4]^+$) away from the WE. This is observed by a sharp increase in positive current, which quickly tails off to zero as oxidisable material is depleted. This WE potential is applied for a pre-determined

amount of time, after which the WE potential is instantaneously reduced to its initial value. In this thesis, CA was used to control charge concentration injected into polymer thin films in the development of a new methodology for the study of polaron stability in semiconducting polymer thin films.

2.4 Spectroelectrochemistry

Electrochemical measurements were performed on materials spin-coated on fluorine-doped tin oxide glass substrates (FTO glass). FTO glass is an example of a transparent conducting oxide (TCO), and is by its very nature transparent, allowing for optical and electrochemical measurements to be performed simultaneously on the material being studied. These measurements are generally referred to as spectroelectrochemical measurements. The three-electrode cell described in 2.3.1 is fixed on a tailored aluminium block, designed to fit in the spectrophotometer and to hold the cell securely such that the optical path of the spectrophotometer is transmitted through the quartz window at the front of the cell. The substrate forms part of the back of the cell, along the beam path, where it is screw-tightened into place, using a rubber O-ring to form the seal. The substrate is oriented such that the TCO/material layer forms part of the inner-wall of the cell, placing the material being studied in direct contact with the supporting electrolyte solution. The substrate was connected to the working electrode port of an Autolab PGstat potentiostat, via crocodile clip and electrical wire, which was used to control the potential applied to the substrate, as well as measure the current between the working electrode and the counter electrode. A thick black cloth was used to cover the top of the spectrophotometer set-up to exclude external light, thereby limiting an obvious source of noise in optical measurements. Supporting electrolyte solutions were the same as those used in cyclic voltammetry measurements, and were prepared as described in 2.1.1.2. This was degassed for 10 minutes immediately before measurements.

2.4.1 Cyclic voltabsorptometry

The optical absorbance at a specific wavelength is measured as a function of sweep potential. This is a useful alternative way of viewing the onset of oxidation in a cyclic voltammetric experiment. One advantage of using optical absorbance to indicate the onset of a redox process is that current measurements are prone to having a background current, which is difficult to exclude. This can make the voltammetric curve difficult to interpret and analyse. Optical absorbance background, on the other hand, can easily be excluded by using a thick black cloth to block out ambient light.

In this thesis, we will demonstrate the use of cyclic voltabsorptometry to estimate Highest Occupied Molecular Orbital (HOMO) energy levels in neat semiconducting polymer films, particularly in Chapter 3, and compare them to interpretations of "classical" current vs applied potential voltammograms. FTO glass is an ideal substrate to use for these studies due to its high optical transparency, and electrical semi-conductivity. Studying polymers as a film also allows for better comparison to polymers operating in plastic electronic devices.

The change in optical absorbance, at the wavelength where absorption intensity of the polymer film is maximal, is measured as a function of applied potential. The onset of oxidation is used to estimate HOMO energy levels (E_{HOMO}, measured in eV) by using the following equation:

$$E_{HOMO} = -(E_{vs\ Fc/Fc^+}^{oxidation\ onset} + 4.8)$$

where $E_{vs\ Fc/Fc^+}^{oxidation\ onset}$ is the oxidation onset potential with respect to the oxidation half potential of ferrocene.

All absorption and electrochemical experiments were carried out at room temperature.

3

Poly(3-ethyhexylthiophene) Crystallinity and its Effect on Highest Occupied Molecular Orbital Energy Levels in Neat Films

Frontier molecular orbital energy levels of conjugated polymer films are commonly estimated through a spectroscopic approach (PESA – photoelectron spectroscopy in air), or through simulation using density functional theory. When cyclic voltammetry is employed, it is often included as a side note, with little or no explanation offered for the overall shape of the voltammogram, and what information this may contain. In this chapter, we will attempt to investigate how cyclic voltammetry can give insight into polymer crystallinity in neat films, and outline what implication this may have on polymer performance in a polymer/fullerene blend.

3.1 Introduction

Conjugated polymers form an important class of materials used in organic electronics due to their impressive transport properties, high optical absorption coefficients, and their potential to be solution-processed from common organic solvents.[69-71] Many of these materials readily form semicrystalline thin films when cast from solution. The degree of crystallinity can be affected by how the films are processed, and can often be controlled through variation of deposition technique, the organic solvent used, solid-state processing, and post-processing treatments (e.g. thermal annealing).[71-75] Charge mobilities in semiconducting polymer thin films are typically significantly lower in amorphous regions than in crystalline ones.[72,76-78] The relative degree of crystallinity in such films is therefore already established as an important criterion in the design of high performance organic electronic devices.[79-82] Changes in crystallinity are also known to affect various optoelectronic properties, including the optical band gap.[83] An increase in crystallinity generally leads to a red-shift of the absorption profile, which is associated with either interchain-delocalisation or a planarisation of the polymer backbone, both of which would result in an increase in π-π conjugation. This overall narrowing of the band gap can be resolved into the destabilisation of the HOMO and/or the stabilisation of the LUMO. It is interesting to note that for a semicrystalline polymer thin film, the resultant absorption spectrum is the linear combination of the absorption spectrum of the amorphous polymer domains and the crystalline polymer domains. It follows that the same is true of the frontier molecular orbital energy levels; the overall MO picture is the linear combination of the MO picture for the amorphous polymer domains and the crystalline polymer domains. In spite of this, energy levels of semicrystalline polymers

are generally reported as a single value for neat films, with little or no insight into how this number relates to crystalline and amorphous domains in the neat film or indeed blend films.[84] Recent work by Jamieson et al. demonstrated how the electron affinity of PCBM blended with poly(2,5-bis(3-tetradecylthiophen-2-yl)thieno[3,2,-*b*]thiophene) (PBTTT) can be increased through PCBM crystallisation by varying blend ratio, thereby providing a thermodynamic driving force for spatial separation of electrons and holes.[85] This is important as it may lead to an improvement in charge separation and a reduction in charge recombination in organic solar cells. Other studies have related the formation of PCBM crystallites to enhanced charge separation and the formation of electron percolation pathways.[86-88]

A recent study by Sweetnam et al. observed an energetic offset of up to 150 meV between amorphous and crystalline polymer in a neat film of regioregular P3HT, and up to 350 meV associated with polymer:fullerene interactions in blend films.[89] This is significant as it suggest that holes will be less stable in amorphous regions than in crystalline regions of the film, and even less stable in mixed domains, thereby "pushing" holes away from high concentrations of electrons, i.e. fullerenes, possibly reducing recombination and improving charge collection.

One of the most widely studied class of conjugated polymers is the poly(3-alkylthiophenes) (P3ATs).[90-93] The most famous example of this class of polymers being poly(3-hexylthiophene) (P3HT), which has become a standard p-type material in organic field-effect transistors (OFETs)[77,94] and as an electron donating material in bulk heterojunction organic solar cells.[71,95,96] It would be interesting, therefore, to study the effect of relative degree of crystallinity of a thin film of P3HT on the frontier molecular

orbital energy levels, which was indeed the original intention of this chapter. One method of controlling the relative degree of crystallinity in a polymer thin film would be to heat the film above its melting temperature and quench directly to room temperature, thereby freezing it in an entirely amorphous state. Since P3HT crystallises at room temperature, performing CV measurements at selected intervals would allow for a time-resolved study of the effect of crystallisation on MO energy level. Unfortunately, the crystallisation kinetics of a P3HT thin film at room temperature is inconveniently much faster than the time it takes to set up a single CV measurement making such a study impossible. Poly(3-(2-ethylhexyl)thiophene) (P3EHT) has the same polymer backbone structure as P3HT and has previously been shown to have similar optoelectronic properties.[97] Conveniently, the introduction of an ethyl group in the 2-position of the hexyl sidechain results in a higher kinetic barrier to backbone rotation, and therefore slower rearrangement from the melt, and much slower crystallisation kinetics at room temperature (*ca* 75 mins).[98]

In this chapter we aim to reveal the effect that polymer crystallinity in neat films has on the HOMO energy level of semiconducting polymers. Due to the convenient timescales of its crystallisation kinetics, we will use P3EHT as our model polymer system. Cyclic voltammetry will be used in conjunction with cyclic voltabsorptometry to determine HOMO energy levels. Absorption spectroscopy will be used to compare relative degrees of crystallinity to studies in the literature. In addition to correlating HOMO energy level with crystallinity, we will also aim to disambiguate the shape of cyclic voltammograms, and how they should be interpreted for other polymer systems.

3.2 Experimental

3.2.1 Thermal annealing

Neat polymer films were annealed in an inert atmosphere using a hot-plate, a glass funnel, and a supply of argon. A diagram of the experimental set-up is provided in Figure 3.1.

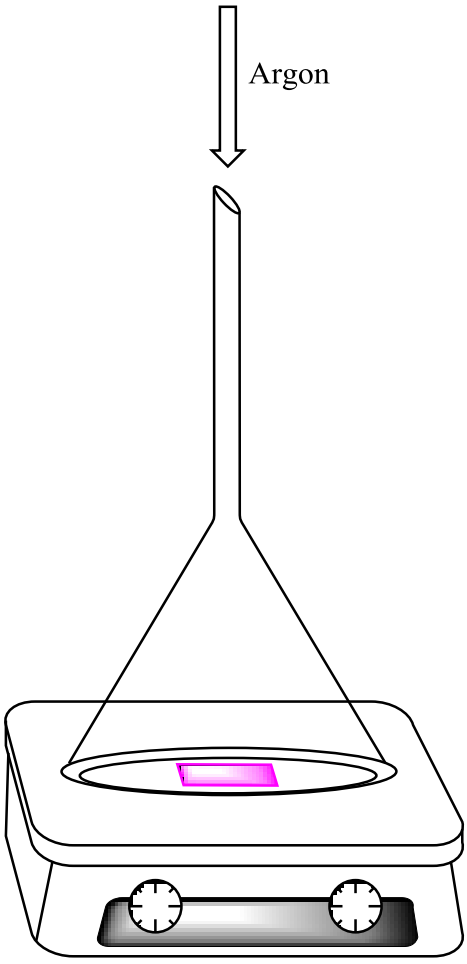

Figure 3.1 – Experimental set-up for thermal annealing station. A glass funnel is suspended just above the surface of a hot-plate, which is supplied with a gentle flow of argon.

The experimental procedure that was followed when annealing neat polymer films is described herein.

The hot-plate was covered with aluminium foil to ensure the annealing surface was clean, thereby avoiding the introduction of contaminants to the polymer neat film. The foil was flattened to ensure a good thermal contact between the hot-plate and the foil.

The hot-plate was turned on, and the temperature dial was set to the annealing temperature. The hot-plate was left for ten minutes in order to allow its temperature to stabilise. A digital infrared thermometer gun was used to determine the temperature of the aluminium foil surface at the centre of the hot-

plate. The temperature dial was adjusted to correct the temperature in order to align the measured temperature with the desired annealing temperature. As before, the hot-plate temperature was allowed to stabilise before it was measured again with the thermometer gun. This temperature correction was reiterated, as necessary, until the desired annealing temperature was achieved.

A glass funnel was connected to a Schlenck line using rubber tubing. A clamp, boss, and clamp-stand were used to secure the funnel upside down, approximately 0.5 cm above the centre of the hot-plate, as per Figure 3.1. A gentle flow of argon was supplied to the funnel via the Schlenck line. The hot-plate was left to stand for *ca* ten minutes, in order to regain its annealing temperature.

With the polymer film facing up, the film to be annealed was swiftly placed at the centre of the hot-plate and a stopwatch was started. The set-up was covered with aluminium foil to exclude light, in order to avoid photochemical reactions. After allowing the film to anneal for the desired time, the hot-plate was turned off and allowed to slowly return to room temperature, whilst maintaining a gentle flow of argon.

3.2.2 Thermal quenching

Neat polymer films were subjected to a thermal quench by first using the annealing set-up (described above) to melt the film, and then rapidly cooling the film on a cold surface. A diagram describing the experimental set-up of the cooling process in the thermal quench is given in Figure 3.2.

3.2.2.1.1 Thermal melt

The annealing experimental set-up (described above) was used, with the annealing temperature being replaced by the melting temperature. The film was placed at the centre of the hot-plate, with the polymer film facing up. The set-up was covered with aluminium foil, and the film was allowed to melt for ten minutes.

Meanwhile, a Dry-Syn heating block was placed into an ice-bath containing an ice-water slurry, and allowed to chill to 0 ^{o}C.

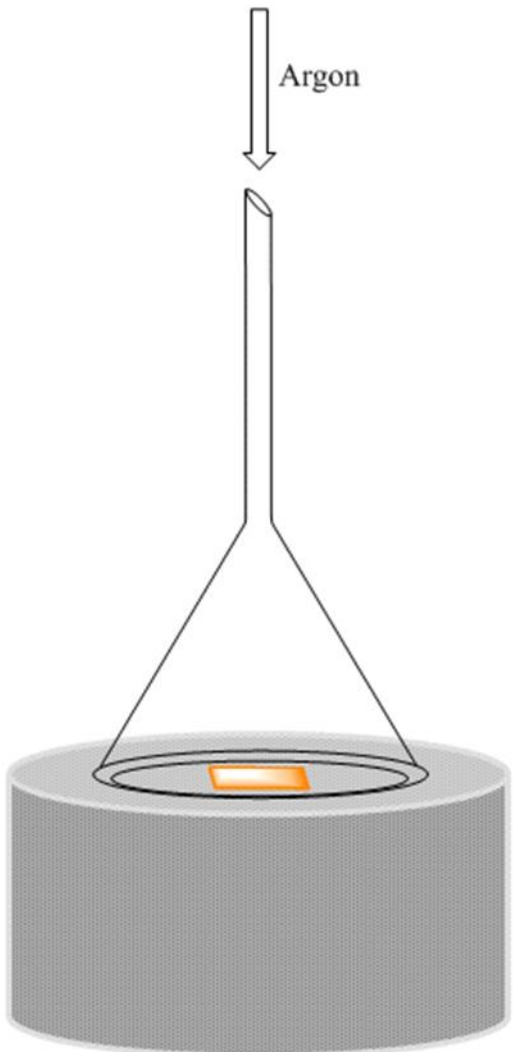

Figure 3.2 – Experimental set-up for thermal quenching station. A glass funnel, supplied with argon, is suspended just above a chilled Dry-Syn heating block.

3.2.2.1.2 Thermal quench

The Dry-Syn heating block was removed from the ice-bath, dried with blu-roll, and placed under a second argon-funnel set-up, immediately before applying the thermal quench. Using a pair of tweezers, the melted film was swiftly moved from the melting station to the quenching station and left to quench for one minute, with the polymer film facing upwards.

Upon removal of the film from the quenching station, a stopwatch was started, and the film was covered with aluminium foil. The stopwatch time

was later used to determine the amount of time that had elapsed since the quench was performed.

3.2.3 Data Analysis

3.2.3.1.1 Cyclic voltammograms (CVs)

To determine the onset potential of a redox event, two tangents are drawn; one from the background current in the build up to the redox event, and another from the rising current of the redox event. The potential at which these two tangents intercept is used to determine the onset potential of the redox event. For the first oxidation event, the background current is usually an approximately horizontal line. For the second oxidation event, the falling current from the first oxidation event is used as the background current. Figure 3.3 uses the cyclic voltammogram from Figure 3.13a to demonstrate how this method was applied to the cyclic voltammogram of a P3EHT film, shortly after quenching.

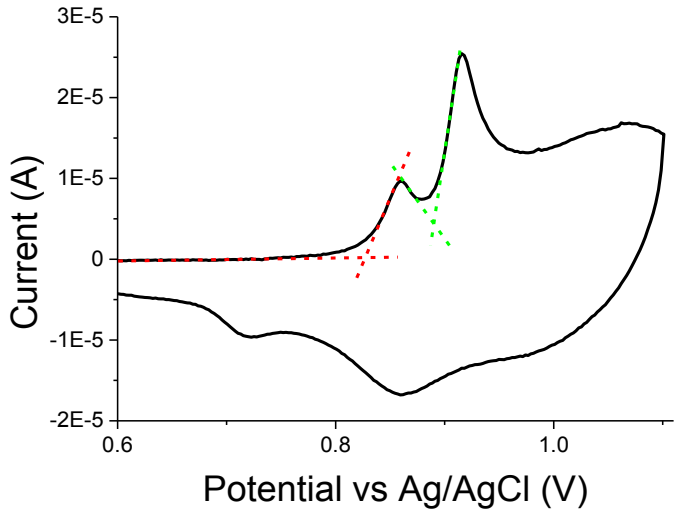

Figure 3.3 – Determination of first (red) and second (green) oxidation onset potentials from cyclic voltammogram.

In Table 3.2 the ratio of the first oxidation peak current to the second oxidation peak current is stated. This was calculated by dividing the first oxidation peak current by the second oxidation peak current. Both the first and second oxidation peaks were determined by two different methods; (i) by reading off the current at the highest point of the respective oxidation peak, and (ii) by correcting the current obtained through the first method by subtracting an estimated background current.

$$Ratio = \frac{I_{first}^{peak}}{I_{second}^{peak}}$$

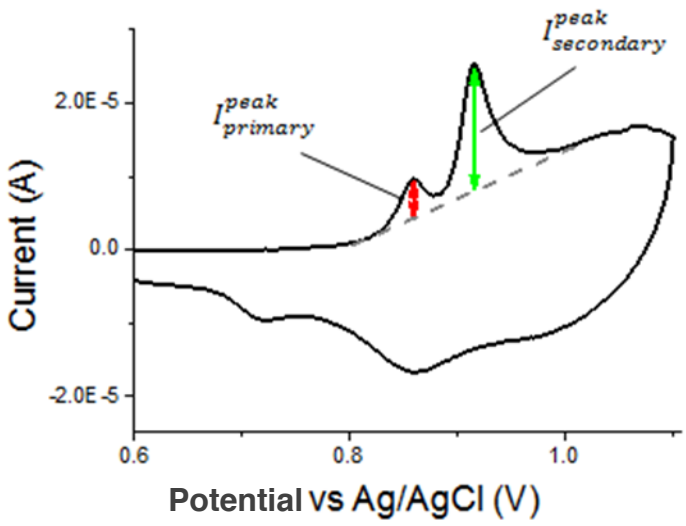

Figure 3.4 – Correcting the first and second oxidation peak currents for the contribution from background currents. The red double-headed arrow represents the first corrected oxidation peak current, and the green arrow represents the second corrected oxidation peak current.

Hence two different ratios are calculated, and the ratio is given as a range between these calculated values. Figure 3.4 uses the cyclic voltammogram from Figure 3.8a to demonstrate this method.

3.2.3.1.2 Cyclic voltabsorptograms

To determine the onset potential of a redox event, two tangents are drawn; one from the background absorption in the build up to the redox event, and another from the falling absorption intensity. The potential at which these two tangents intercept is used to determine the onset potential of the redox event. For the first oxidation event, the background absorption intensity is a horizontal line where Norm Abs = 1.00.

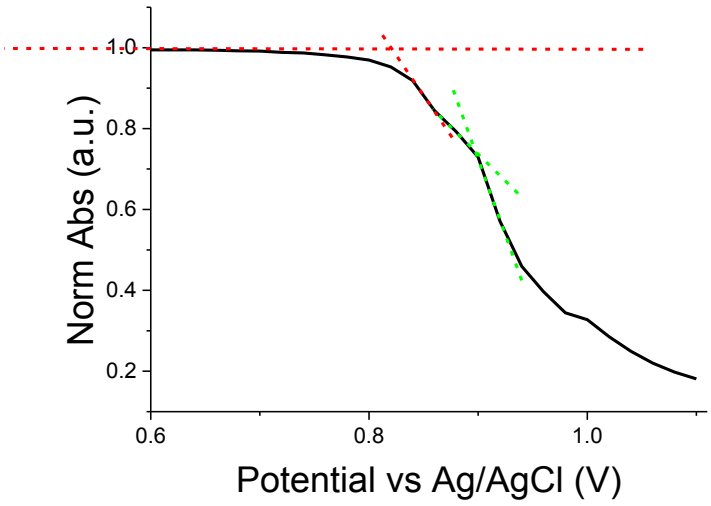

Figure 3.3.5 – Determination of onset potentials of first (red) and second (green) oxidation events from cyclic voltabsorptogram.

For the second oxidation event, the background absorption intensity is considered to be the falling absorption intensity caused by the first oxidation event. The falling absorption intensity of the second oxidation event is considered to be the region after the first oxidation event where there is a sudden increase in gradient. This is demonstrated in Figure 3.3.5. It should be noted that this method of determining the second oxidation potential is difficult, and so it is useful to consider the first derivative of the cyclic voltabsorptogram.

3.2.3.1.3 First derivative of cyclic voltabsorptogram (dCVA)

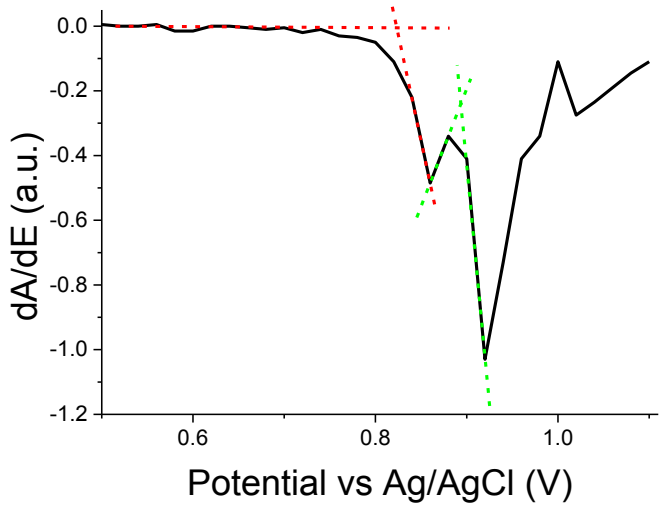

Figure 3.3.6 – Determination of onset potentials of first (red) and second (green) oxidation events from the first derivative of a cyclic voltabsorptogram (dA/dE), with respect to potential.

The quantity dA/dE in the first derivative of the cyclic voltabsorptogram is equivalent to the gradient of the absorption in a cyclic voltabsorptogram. Similar to the analysis of a cyclic voltammogram, the onset potential of a redox event using the first derivative of a cyclic voltabsorptogram can be determined by drawing two tangents; one from the background gradient in the build up to the redox event, and another from the rising gradient of the redox event. The potential at which these two tangents intercept is used to determine the onset potential of the redox event. For the first oxidation event, the first background gradient is usually an approximately horizontal line. For the second oxidation event, the falling gradient from the first oxidation event is used as the second background gradient. Figure 3.3.6 uses the first dCVA (first derivative of a cyclic voltabsorptogram, with respect to potential) from Figure 3.13c to demonstrate how this method was applied to the dCVA of a P3EHT film, shortly after quenching.

3.3 Results

3.3.1 Cyclic voltammetry and absorption spectroscopy study on the crystallisation of P3EHT neat films

3.3.1.1 As-spun P3EHT neat films

Stirring P3EHT (0.2 mg) in degassed dry chloroform (1 mL) at room temperature resulted in a clear, bright orange solution. Spin-coating the solution onto a clean, dry FTO glass substrate resulted in a purple thin film. The absorption spectrum of P3EHT, as-spun (Figure 3.7) exhibits an absorption maximum at 492 nm, which is accompanied by several shoulders indicating some vibronic structure. This fine structure in the absorption spectrum is described by Franck-Condon coupling within microcrystalline domains embedded in an amorphous matrix.[99] Similar structures in the absorption spectrum of P3HT have previously been attributed to the high degree of intra and interchain order in the film.[100] The first optical bandgap is estimated by considering the

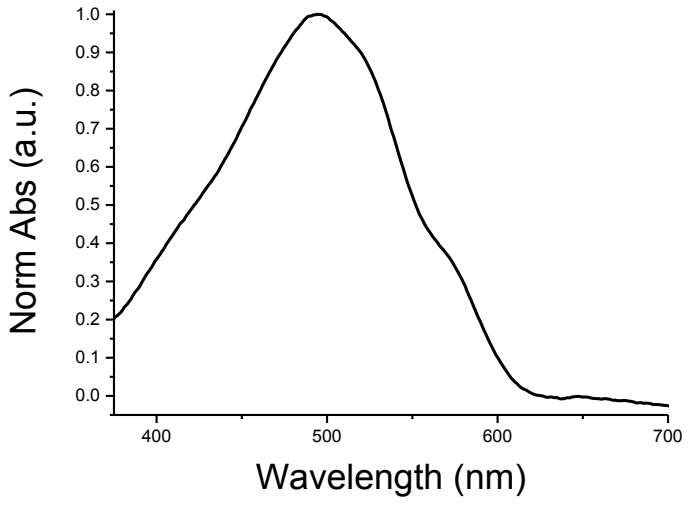

Figure 3.7 - Normalised absorption spectrum of a neat film of P3EHT, as-spun, on an FTO glass substrate. Absorption spectrum was measured in an electrochemical cell containing 0.1 M tetrabutylammonium hexafluorophosphate in dry acetonitrile solution.

onset of absorption of the shoulder on the extreme right of the main peak at 613 nm, which corresponds to a first optical bandgap of 2.03 eV. The second optical bandgap is estimated by considering the onset of absorption of the main peak at 558 nm, which corresponds to a second optical bandgap of 2.22 eV.

Cyclic voltammetry (CV) was carried out in order to obtain estimates for frontier molecular orbital energy levels of the polymer film, as spun. The oxidative cyclic voltammogram (Figure 3.8a) was carried out with a scan rate of 20 mV s^{-1}, and exhibited a first sharp oxidation peak at +0.88 V. The first HOMO energy level is estimated by considering the onset potential of this oxidation peak, +0.84 V, which corresponds to a HOMO energy level of -5.20 eV. A less conspicuous second oxidation peak is observed at +0.93 V, with an onset potential of +0.90 V, corresponding to a second HOMO energy level of -5.26 eV. The absorption intensity at the peak absorption wavelength was measured simultaneously as a function of applied potential to give the cyclic voltabsorptogram (CVA, Figure 3.8b). The first onset of oxidation is represented by the initial drop in absorption intensity at +0.84 V, which also translates to a first HOMO energy level of -5.20 eV. A second onset of oxidation is not observed. The cyclic voltammogram corresponds to the rate of change of population of redox reactive species (i.e. neutral polymer) as a function of applied potential, whilst the cyclic voltabsorptogram corresponds to the population of redox reactive species as a function of applied potential. The first derivative of absorption intensity with respect to the applied potential (dCVA, Figure 3.8c) corresponds to the rate of change of population of redox reactive species, allowing for direct comparison of cyclic voltammetry and cyclic voltabsorptometry. A first sharp oxidation peak is observed in the dCVA at +0.87

V. The HOMO energy level can once again be estimated by considering the onset potential of this oxidation peak, +0.82 V, which corresponds to a HOMO energy level of -5.18 eV. A second oxidation peak is not observed.

a)

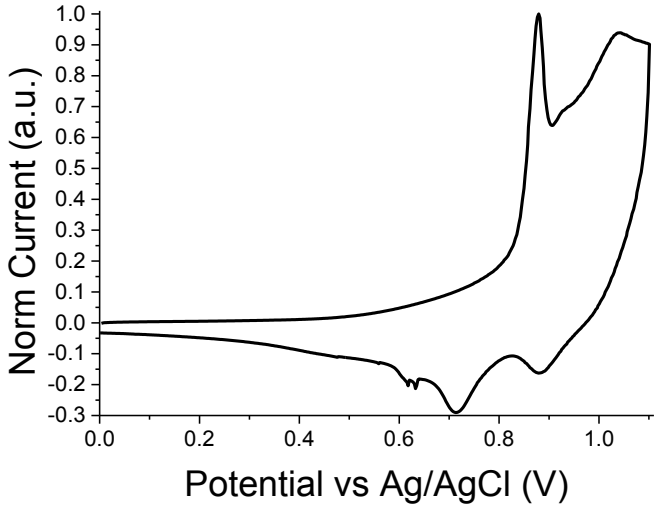

b)

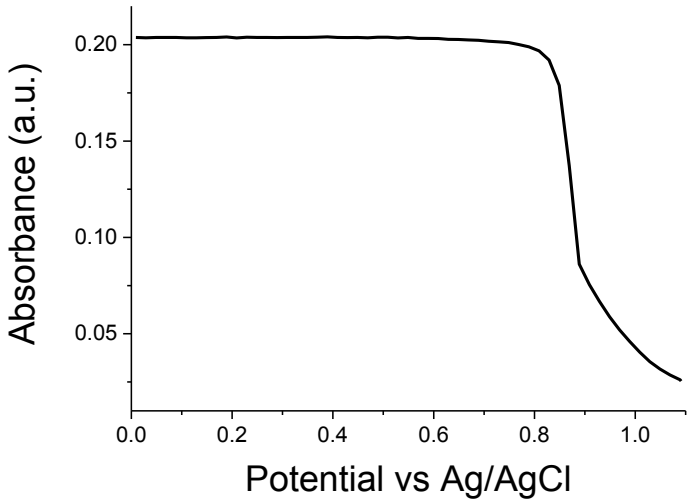

c)

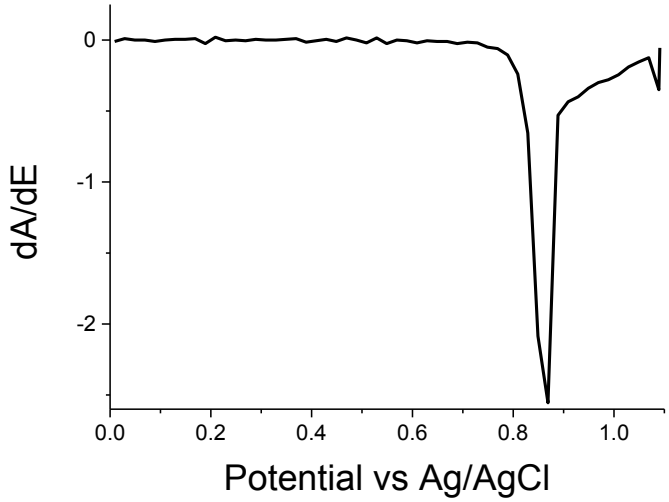

Figure 3.8 – Investigation of HOMO energy level of a neat film of P3EHT on FTO glass, as spun; a) cyclic voltammogram, b) cyclic voltabsorptogram, and c) first derivative of the cyclic voltabsorptogram, with respect to applied potential. All three plots are based on the same cyclic voltammetry experiment on a single pristine sample.

The reductive cyclic voltammogram (Figure 3.9a) was also carried out with a scan rate of 20 mV s^{-1}, and exhibited a broad reduction peak at -1.46 V. The first LUMO energy level is estimated by considering the first onset potential of this reduction peak, -0.78 V, which translates to a first LUMO energy level of -3.58 eV. The difference in energy between the first HOMO and first LUMO energy levels, as determined from analysis of the cyclic voltammograms, is used to provide an estimate for the first electrochemical bandgap, and gives a value of 1.62 eV. A second reduction onset is observed at -1.20 V, which translates to a second LUMO energy level of -3.16 eV. The difference in energy between the second HOMO and second LUMO energy levels, as determined from analysis of the cyclic voltammograms, is used to provide an estimate for the second electrochemical bandgap, and gives a value of 2.10 eV. CVA measurements (Figure 3.9b) were carried out during LUMO energy level determination, revealing a first reduction onset potential of -0.90 V, corresponding to a first LUMO energy level of -3.46 eV. By comparing this value with the corresponding CVA measurement of the first HOMO (above), a first electrochemical bandgap of 1.74 eV is obtained. A second reduction onset is observed at -1.23 V, corresponding to a second LUMO energy level of -3.27 eV. Finally, dCVA measurements (Figure 3.9c) reveal a first reduction onset at -0.82 V, corresponding to a first LUMO energy level of -3.54 eV, and a first electrochemical bandgap of 1.65 eV. A second reduction onset is observed at -1.11 V, corresponding to a second LUMO energy level of -3.25 eV.

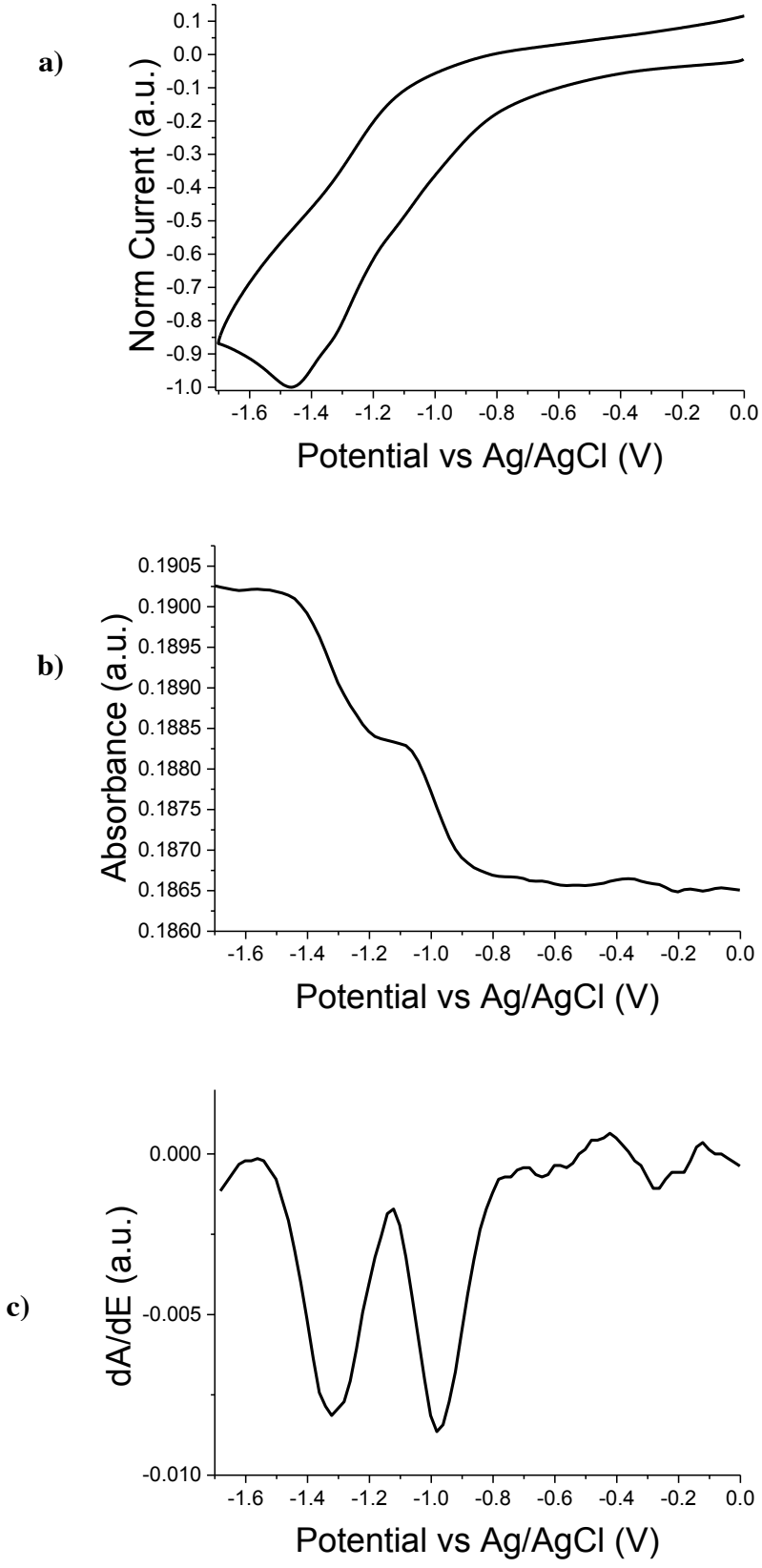

Figure 3.9 - Investigation of LUMO energy level of a neat film of P3EHT on FTO glass, as spun; a) normalised cyclic voltammogram, b) smoothed cyclic voltabsorptogram, and c) smoothed first derivative of the cyclic voltabsorptogram, with respect to applied potential. All three plots are based on the same cyclic voltammetry experiment on a single pristine sample.

3.3.1.2 Thermal annealing of P3EHT neat films

Neat films of P3EHT were prepared using an identical methodology to that described above, and then thermally annealed at 60 ^{o}C for 3 hours, in the absence of oxygen. The annealed film was similar in colour to the as-spun film, as confirmed by absorption spectroscopy in Figure 3.10. The absorption spectrum of annealed P3EHT exhibits an absorption maximum at 494 nm, which is comparable to the absorption maximum of as-spun P3EHT (492 nm). Similar, and yet more pronounced absorption shoulders are present in the annealed film absorption spectrum suggesting an increase in vibronic structure. The onset of absorption for the annealed film (609 nm) is very similar to that of the as-spun film (613 nm), resulting in a similar optical bandgap of 2.04 eV.

The oxidative cyclic voltammogram in Figure 3.11a displays a first sharp oxidation peak at +0.87 V, with an oxidation onset potential of +0.83 V, corresponding to a first HOMO energy level of -5.19 eV. Further, a less obvious second oxidation peak is observed at +0.93 V, with an onset potential of +0.89 V, corresponding to a second HOMO energy level of -5.25 eV. A first onset of oxidation is observed in the CVA (Figure 3.11b) at +0.84 V, corresponding to a first HOMO energy level of -5.20 eV. A dCVA second onset of oxidation is not observed. A first oxidation peak is observed in the (Figure 3.11c) at +0.88 V, with an onset potential of +0.84 V, corresponding to a first HOMO energy level of -5.20 eV. A second oxidation peak is not observed.

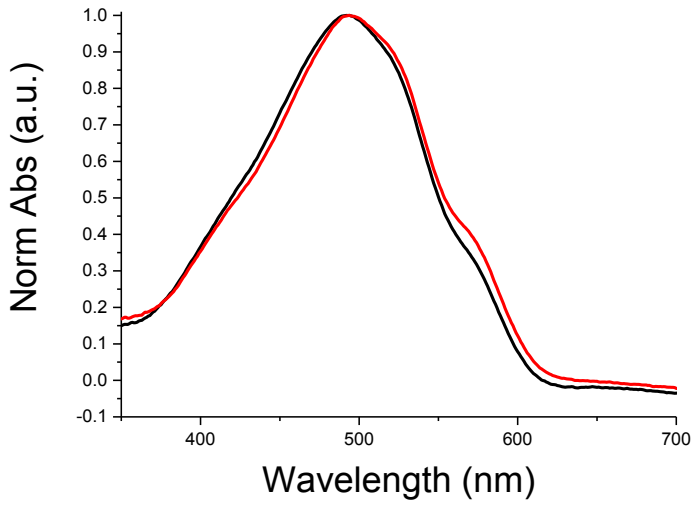

Figure 3.10 – Normalised absorption spectrum of an annealed film of P3EHT (red) compared with normalised absorption spectrum of an as-spun film of P3EHT (black).

a)

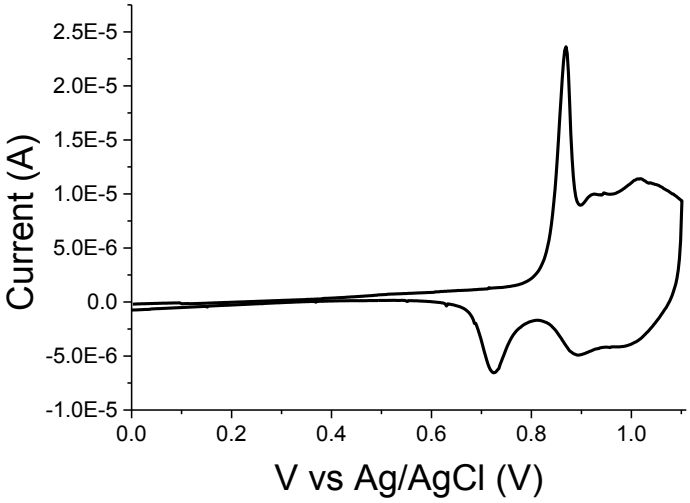

b)

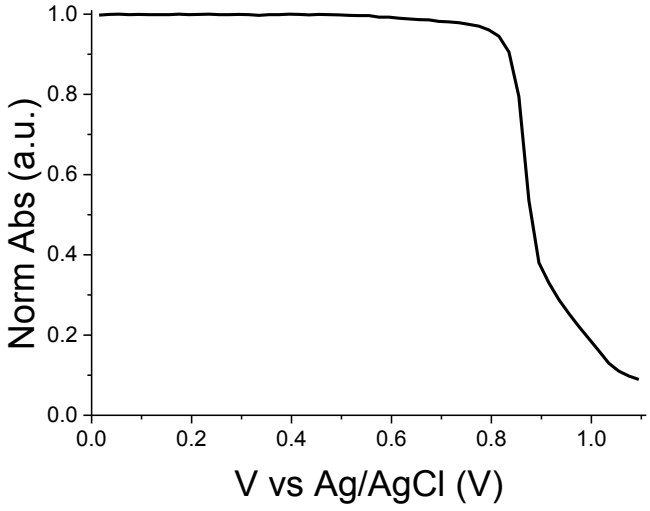

c)

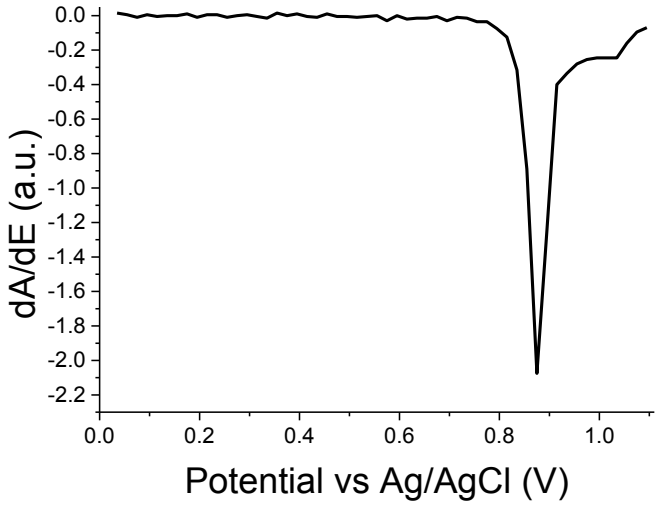

Figure 3.11 – Investigation of HOMO energy level of a neat film of P3EHT on FTO glass, after annealing; a) cyclic voltammogram, b) cyclic voltabsorptogram, and c) first derivative of the cyclic voltabsorptogram, with respect to applied potential.

3.3.1.3 P3EHT films quenched immediately from the melt to room temperature

Neat films of P3EHT were prepared using an identical method to that described above, before subjecting the neat films to a thermal quenching experiment. This resulted in the films having a colour that was similar to that of the orange polymer solution.

The change in colour after the thermal quench experiment is reflected by the change to its absorption spectrum, given in Figure 3.12. An absorption maximum is observed at 464 nm, representing a blue-shift of *ca*. 30 nm, compared to the as-spun film, whilst the shoulders present in the as-spun sample have been removed. Its optical bandgap can be estimated by considering the significantly blue-shifted onset of absorption at 574 nm, which translates to an optical bandgap of 2.16 eV.

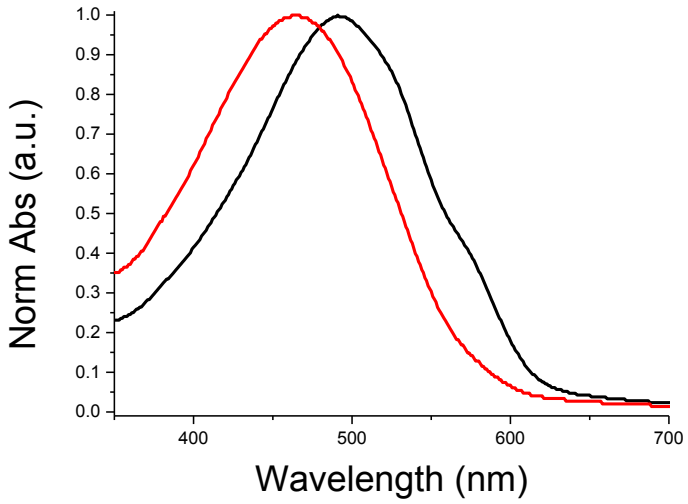

Figure 3.12 - Normalised absorption spectra of neat films of P3EHT as spun (black) and immediately after a thermal quench (red).

Due to the time involved in setting up a cyclic voltammetry experiment, it was not possible to provide an estimate for HOMO energy level immediately after thermal quenching. Instead cyclic voltammetry was carried out 15 minutes after the thermal quench, and is compared with the as-spun film in Figure 3.13a. Experimental set-up and parameters were identical to that used for the as-spun film. The oxidative cyclic voltammogram exhibits two distinct oxidation peaks. The first peak is notably less intense than the second peak. The first oxidation peak is observed at +0.86 V, with an onset potential of +0.83 V, corresponding to a HOMO energy level of -5.19 eV. The second oxidation peak is observed at +0.92 V, with an onset potential of +0.89 V, corresponding to a HOMO energy level of -5.25 eV. The cyclic voltabsorptogram was recorded as described in 3.3.1.1, and is compared to that of the as-spun film in Figure 3.13b. The shape of the CVA of the quenched film is notably different to that of the as-spun film; the absorption intensity appears to drop in two stages, suggesting that there are two separate oxidation events occurring. A first oxidation onset potential is observed at +0.81 V, corresponding to a first HOMO energy level of -5.17 eV, whilst a second onset potential is observed at +0.87 V, corresponding to a second HOMO energy level of -5.23 eV. Two oxidation processes are observed in the dCVA in Figure 3.13c. The first oxidation peak is observed at +0.86 V, with an onset potential of +0.82 V, corresponding to a first HOMO energy level of -5.18 eV. The second oxidation peak is observed at +0.92 V, with an onset potential of +0.89 V, corresponding to a second HOMO energy level of -5.25 eV.

a)

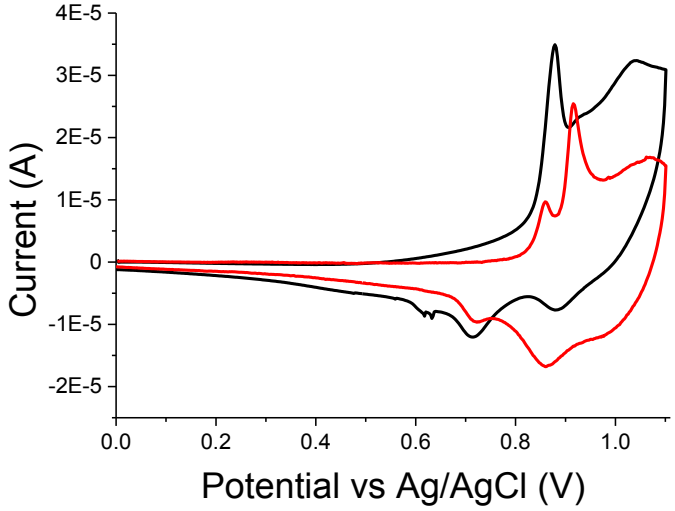

b)

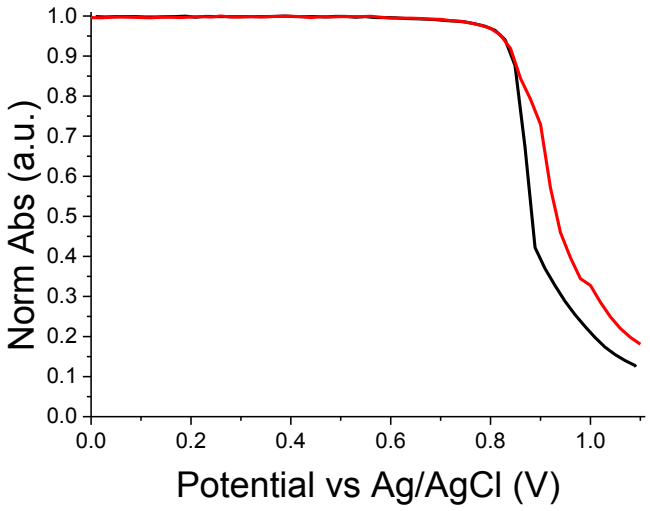

c)

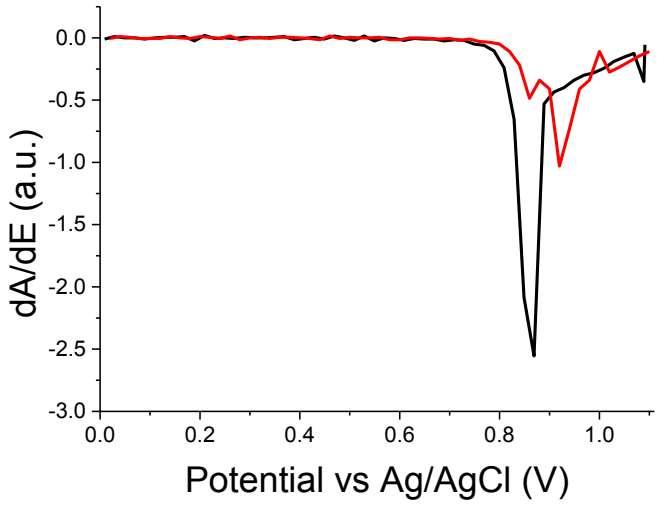

Figure 3.13 – Comparison of HOMO energy level investigation of an as-spun (black) and a thermally quenched (red) film of P3EHT on FTO glass; a) cyclic voltammogram, b) cyclic voltabsorptogram, and c) first derivative of the cyclic voltabsorptogram, with respect to applied potential. The quenched film was measured 15 minutes after quenching.

3.3.1.4 Room temperature annealing from quench

Several films of P3EHT were prepared and quenched, using the same procedures as outlined above, and left in the dark in the absence of oxygen at room temperature, to investigate how the HOMO energy level evolves with time after quenching.

3.3.1.4.1 Absorption spectroscopy

Table 3.1 – Absorption data taken from Figure 3.14, displaying the evolution of the absorption maximum, absorption onset, and full width half maximum as a function of time after thermal quenching. Absorption data for evolution times not included in Figure 3.14 is also tabulated. Absorption data for as-spun and annealed films (Figure 3.10) is included for comparison.

Time after quench / days:hours:mins	**Absorption maximum / nm**	**FWHM / nm**	**Absorption onset / nm**	**E_g^{opt} / eV**
00:00:00	464	140	574	2.16
00:00:10	468	146	604	2.06
00:00:32	465	146	608	2.04
00:00:53	483	144	606	2.05
00:01:21	482	145	608	2.04
00:01:38	482	147	607	2.05
00:03:18	488	119	607	2.05
00:23:22	493	128	609	2.04
02:02:00	492	129	609	2.04
As-spun	492	133	613	2.03
Annealed	494	123	609	2.04

The absorption spectrum of each film was measured at a given amount of time after quenching, which is displayed in Figure 3.14. The optical bandgap was estimated by

considering the onset absorption wavelength, which narrowed by *ca* 100 meV during the first 10 minutes after quenching, and thereon did not change significantly. The absorption maximum red-shifts by *ca* 30 nm in the first half hour after quenching, after which it stabilises at *ca* 493 nm. Absorption data is summarised in Table 3.1.

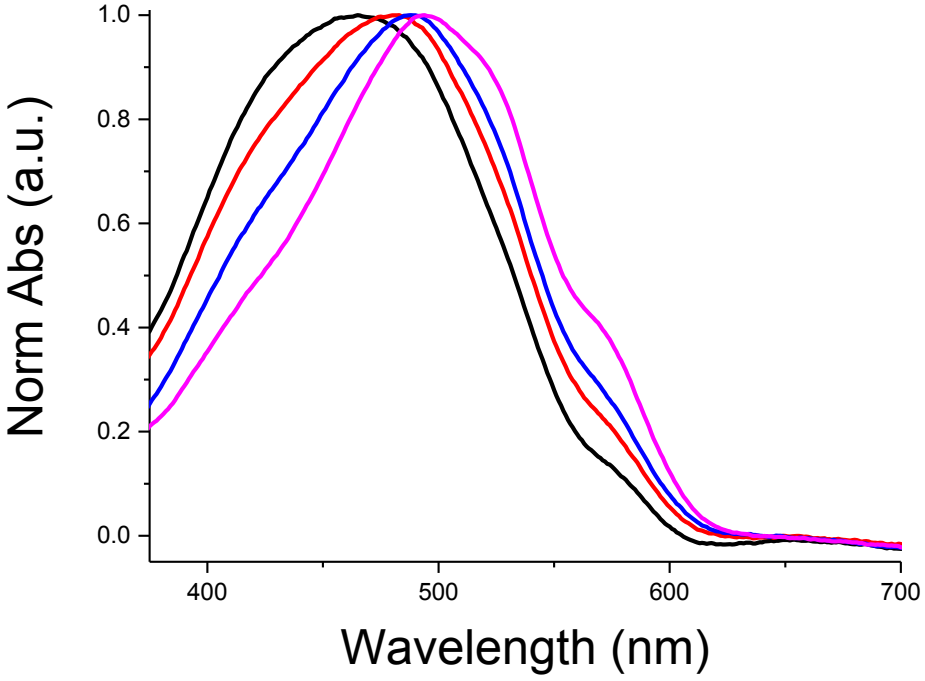

Figure 3.14 – Normalised absorption spectra of neat films of P3EHT at 32 minutes (black), 1 hour 38 minutes (red), 3 hours 18 minutes (blue), and 7 days 21 hours 8 minutes (magenta), after quenching from melt to 0 ^{o}C.

3.3.1.4.2 Cyclic voltammetry

Table 3.2 – Cyclic voltammetry data taken from Figure 3.15, displaying the evolution of the onset potential and peak potential values of the first and second oxidation peaks, as well as the ratio of peak currents. Cyclic voltammetry data for as-spun and annealed films (Figure 3.8a and Figure 3.11a, respectively) is included for comparison.

$^{\mathbf{F}}$calculated from non-corrected oxidation peak currents; *calculated from corrected oxidation peak currents (see 3.2.3.1.1 on page 69 for a more detailed explanation)

Time after quench / dd:hh:mm	V_{first}^{onset} **/ V**	V_{second}^{onset} **/ V**	$I_{first}^{peak} : I_{second}^{peak}$ **/ a.u.**
00:00:15	+0.83	+0.89	*0.30-$^{\mathbf{F}}$0.38
00:00:36	+0.83	+0.89	*0.34-$^{\mathbf{F}}$0.40
00:00:59	+0.84	+0.88	$^{\mathbf{F}}$1.02-*1.28
00:01:26	+0.84	+0.89	$^{\mathbf{F}}$0.90-*1.20
00:01:45	+0.84	+0.89	$^{\mathbf{F}}$0.89-*1.05
00:03:24	+0.84	+0.89	$^{\mathbf{F}}$1.49-*2.54
00:23:26	+0.84	+0.89	$^{\mathbf{F}}$2.24-*4.84
02:02:05	+0.84	+0.89	$^{\mathbf{F}}$2.03-*8.25
05:00:50	+0.84	+0.89	$^{\mathbf{F}}$2.45-*5.57
07:21:08	+0.83	+0.89	$^{\mathbf{F}}$2.67-*7.77
As-spun	+0.84	+0.90	$^{\mathbf{F}}$1.64-*7.07
Annealed	+0.83	+0.89	$^{\mathbf{F}}$2.65-*8.27

Cyclic voltammetry was performed on each film shortly after the absorption spectra in Figure 3.14 were recorded.

Table 3.2 includes CV data for the quench experiment, as well as for the as-spun and annealed films for comparison. Generally, two oxidation peaks are observed in the cyclic voltammograms. As time progresses, the ratio of the first oxidation peak current to the second oxidation peak current generally increases. There is no significant change to the onset or peak values for either peak as time elapses (Table 3.3).

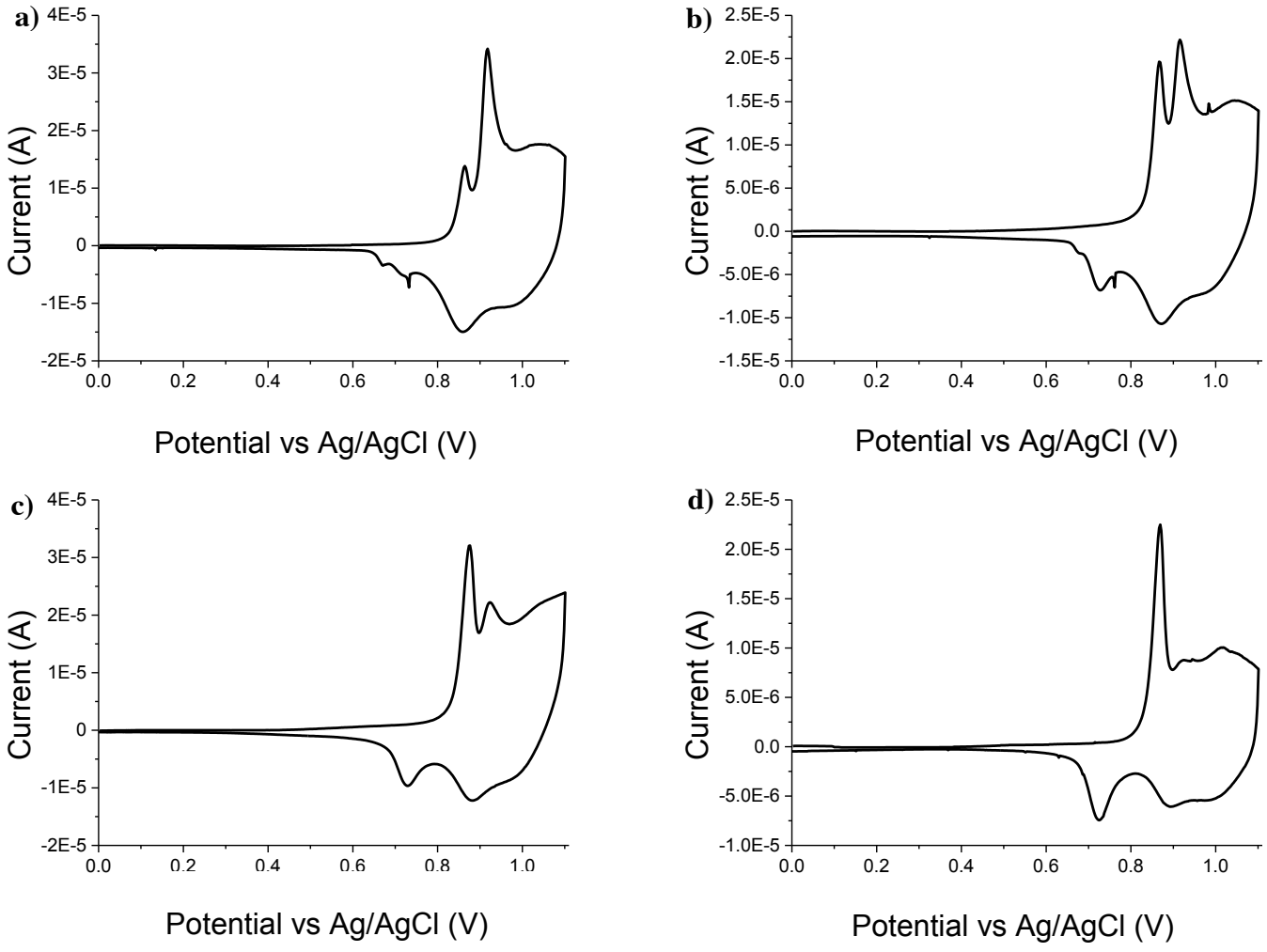

Figure 3.15 – Cyclic voltammograms of neat films of P3EHT; a) 36 minutes, b) 1 hour 45 minutes, c) 3 hours 24 minutes, d) 7 days 21 hours 8 minutes after quenching.

3.3.1.4.3 Cyclic voltabsorptometry

Table 3.3 – Cyclic voltabsorptogram data taken from Figure 3.16, displaying the evolution of the onset potential of the first and second oxidation events. Cyclic voltabsorptogram data for as-spun film (Figure 3.8b) is included for comparison.

Time after quench / dd:hh:mm	V_{first}^{onset} / V	V_{second}^{onset} / V
00:00:15	+0.82	+0.87
00:00:36	+0.83	+0.87
00:00:59	+0.83	+0.85
00:01:26	+0.83	+0.86
00:01:45	+0.84	+0.87
00:03:24	+0.85	+0.88
00:23:26	+0.84	+0.87
02:02:05	+0.84	+0.88
05:00:50	+0.84	+0.89
07:21:08	+0.83	+0.87
As-spun	+0.84	+0.89

Absorption intensity was measured at the absorption maximum wavelength simultaneous to each cyclic voltammogram experiment to produce the cyclic voltabsorptograms in Figure 3.16. The onset of the first and second oxidation events is represented in the CVA plots by a drop in absorption intensity, and is recorded in Table 3.3. As time progresses, there is no significant change in the first or second oxidation onset potentials.

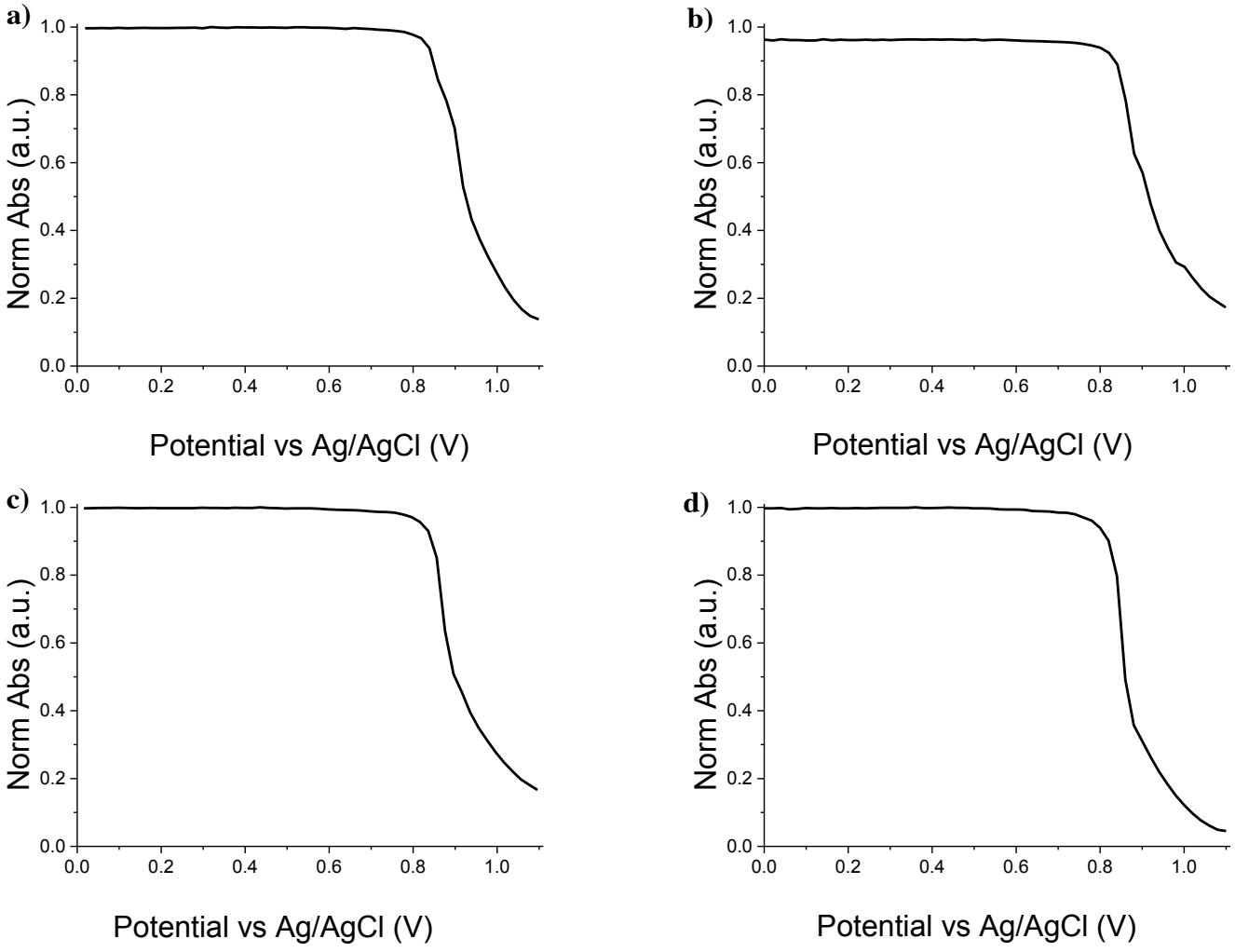

Figure 3.16 – Cyclic voltabsorptograms of neat films of P3EHT; a) 36 minutes, b) 1 hour 45 minutes, c) 3 hours 24 minutes, d) 7 days 21 hours 8 minutes after quenching. Absorption intensity was measured at polymer absorption maximum wavelength and was collected during the same cyclic voltammetry experiment displayed in Figure 3.15.

3.3.1.4.4 First derivative of cyclic voltabsorptometry

Table 3.4 – First derivative of cyclic voltabsorptogram data taken from Figure 3.17, displaying the evolution of the onset potential of the first and second oxidation events. The ratio between the intensities of the peaks representing the first and second oxidation events is calculated. dCVA data for as-spun and annealed films is included for comparison.

Time after quench / dd:hh:mm	V_{first}^{onset} / V	$\left\|\frac{dA^{peak}}{dE\,first}\right\|$ / a.u.	V_{second}^{onset} / V	$\left\|\frac{dA^{peak}}{dE_{second}}\right\|$ / a.u.	$dA/dE_{first}^{peak} : dA/dE_{second}^{peak}$ / a.u.
00:00:15	+0.82	0.48	+0.89	1.02	0.47
00:00:36	+0.83	0.77	+0.89	1.42	0.54
00:00:59	+0.84	1.11	+0.89	0.58	1.91
00:01:26	+0.83	1.42	+0.89	0.66	2.15
00:01:45	+0.83	1.30	+0.90	0.78	1.67
00:03:24	+0.85	1.85	+0.92	0.51	3.62
00:23:26	+0.83	2.12	-	<0.32	>6.63
02:02:05	+0.84	2.61	-	<0.40	>6.53
05:00:50	+0.82	2.31	-	0.39	>5.92
07:21:08	+0.81	2.08	-	<0.32	>6.50
As-spun	+0.83	2.56	-	<0.40	>6.40
Annealed	+0.84	2.08	-	<0.37	>5.62

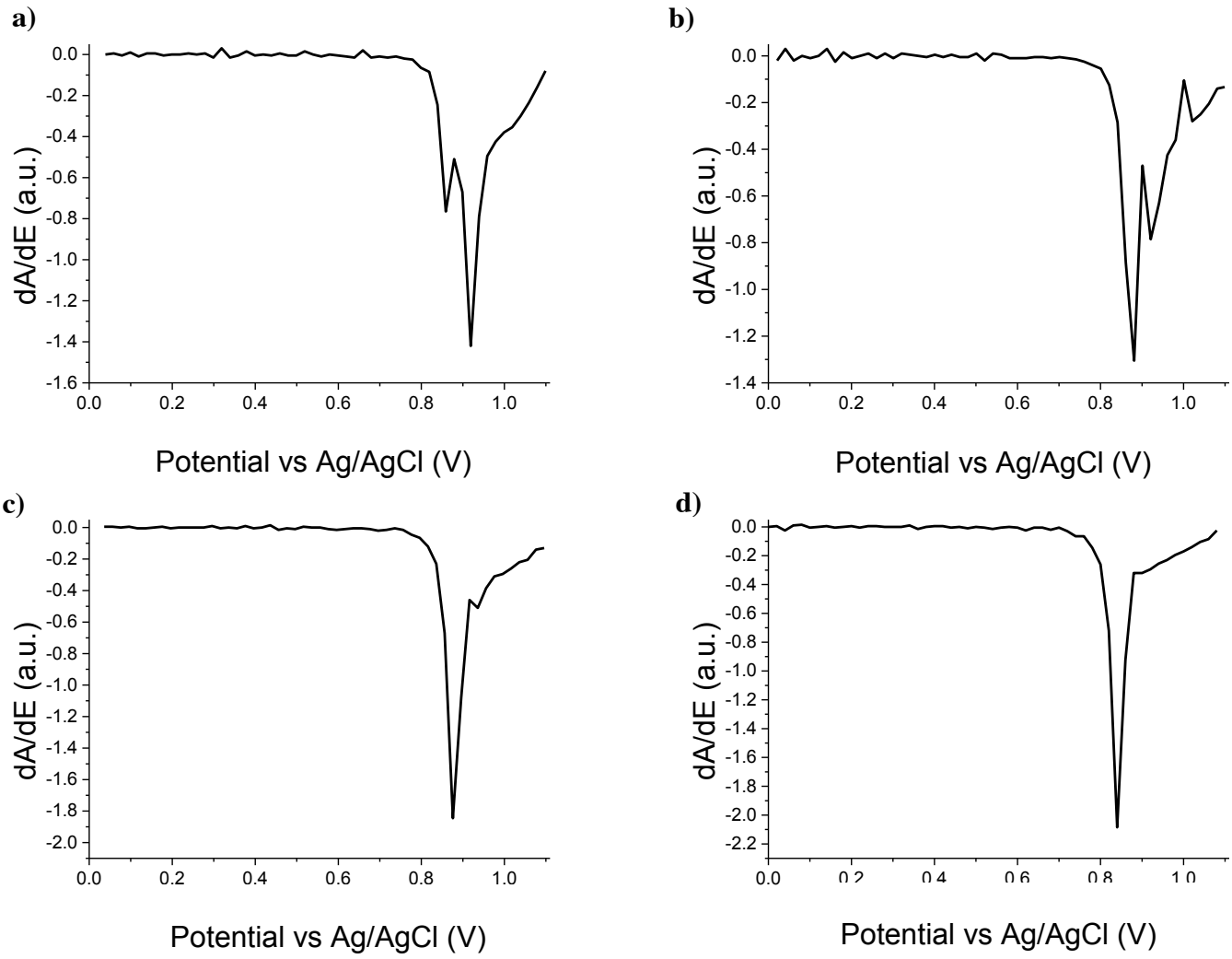

Figure 3.17 – First derivative with respect to reference electrode potential of cyclic voltabsorptograms (from Figure 3.16) of neat films of P3EHT; a) 36 minutes, b) 1 hour 45 minutes, c) 3 hours 24 minutes, d) 7 days 21 hours 8 minutes after quenching.

3.4 Discussion

A time-resolved electrochemical study of P3EHT was successfully performed on neat films to investigate the effect of crystallinity on HOMO energy level of a poly(3-alkylthiophene) (P3AT) polymer. P3EHT was selected as the model polymer to its semicrystalline nature, and the convenient timescales on which it crystallises.

We initially discuss the as-spun neat film. Cyclic voltammetry was successfully performed on a neat film of P3EHT, which resulted in two distinct HOMO energy levels as well as two distinct LUMO energy levels.

Table 3.5 - Comparison of molecuar orbital energy levels and electrochemical bandgaps obtained by cyclic voltammetry (CV), cyclic voltabsorptometry (CVA), and the first derivative of the cyclic voltabsorptammogram with respect to applied potential (dCVA). Subscripts *crys* and *am* refer to crystalline and amorphous regions of the film, respectively. Optical bandgaps obtained by absorption spectroscopy (UV-vis) are included for comparison.

	$HOMO_{crys}$ / eV	**$LUMO_{crys}$ / eV**	**$E_{g,\,crys}$ / eV**	**$HOMO_{am}$ / eV**	**$LUMO_{am}$ / eV**	**$E_{g,\,am}$ / eV**
CV	-5.20	-3.58	1.62	-5.26	-3.16	2.10
CVA	-5.20	-3.46	1.74	-5.23	-3.27	1.96
dCVA	-5.19	-3.54	1.65	-5.26	-3.25	2.01
UV-vis	-	-	2.04	-	-	2.22

Considering CV, the first and second HOMO energy levels are attributed to the crystalline/aggregate (-5.20 eV) and amorphous (-5.26 eV) regions of the film, respectively. Similarly, the first and second LUMO energy levels are attributed to the crystalline/aggregate (-3.58 eV) and amorphous (-3.16 eV) regions of the film, respectively. Two electrochemical bandgaps are thus calculated to be 1.62 eV and 2.10

eV, which are assigned to the crystalline and amorphous regions, respectively. The electrochemical bandgap is effectively widened by *ca* 480 meV. Consideration of the absorption spectrum also leads to two optical bandgaps being observed, with values of 2.03 eV for the crystalline regions and 2.22 eV for the amorphous regions. The optical bandgap is effectively widened by *ca* 180 meV, which is slightly at odds with the magnitude observed by CV. One explanation for this difference is that the estimate obtained by CV for the second (amorphous) LUMO energy level is too shallow due to the difficulty in distinguishing between two ill-defined and overlapping reduction waves with similar onset potentials, hence leading to an estimate for the amorphous bandgap that is too wide. Considering the electrochemical bandgaps obtained by the dCVA data, the bandgap is effectively widened by *ca* 360 meV, which is in better agreement with that value obtained by absorption spectroscopy. This is a good example of where optical data can be used to effectively support an otherwise ambiguous voltammogram. Figure 3.18 gives a graphical representation of the energy landscape of a neat film of P3EHT. The 60 meV energy offset of the HOMOs provides a driving force for holes to move from less ordered amorphous regions to crystalline regions of a film. One way of quantifying this effect is to consider the population of holes in semicrystalline films to reside on crystalline and amorphous regions in equilibrium:

$$h^+_{amorphous} \quad \underset{\rightleftharpoons}{K} \quad h^+_{crystalline}$$

The equilibrium constant (K) is defined as follows:

$$K = \frac{[h^+_{crystalline}]}{[h^+_{amorphous}]}$$

Where [h^+] represents the concentration of hole species in a region. The equilibrium constant can be calculated by considering the Gibbs free energy (ΔG) associated with a hole moving from an amorphous region to a crystalline region:

$$\Delta G = -nFE$$

$$= -1\ x\ 96{,}458\ x\ 0.060$$

$$= -5{,}788\ Jmol^{-1}$$

where *n* is the number of electrons involved in the redox process, *F* is Faraday's constant, and *E* is the difference in energy between the amorphous and crystalline regions. The equilibrium constant can thus be calculated:

$$K = e^{-\frac{\Delta G}{RT}} = e^{\frac{5{,}788}{8.31\ x\ 298}} = 10$$

where *R* is the molar gas constant, and *T* is temperature (assumed to be room temperature). The position of equilibrium therefore favours holes in the crystalline regions, with the population of holes in crystalline regions predicted to be an order of magnitude higher than that in amorphous regions. This energy offset is significant as it means that crystalline domains may offer a thermodynamic sink for hole charge carriers, similar to the electron thermodynamic sinks created by fullerene crystalline domains in bulk heterojunction solar cells.[85]

This driving force is predicted to be even larger for polymer/fullerene mixed domains in blend films, as the fullerenes further disrupt order in the polymer. This could be important for increasing the spatial separation between photogenerated holes and the

high concentration of electrons on fullerenes, limiting charge recombination and maximising charge collection.

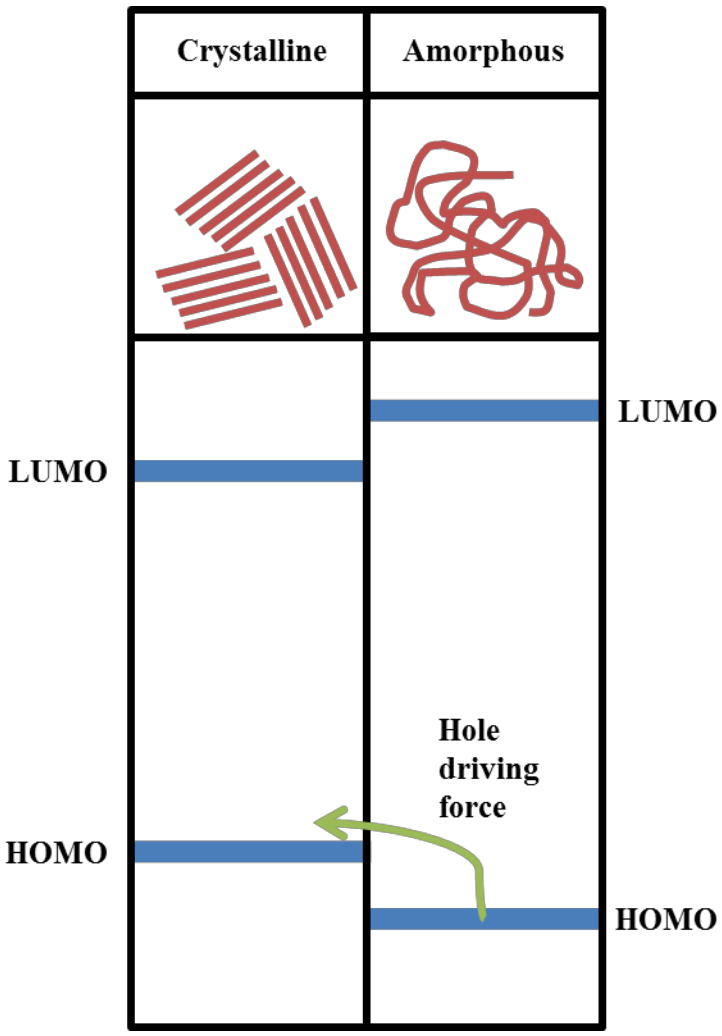

Figure 3.18 – Graphical representation of the energy landscape of a neat film of P3EHT. Not to scale.

A thermal quench was successfully performed on thin films of P3EHT, in order to carry out a time-resolved electrochemical study of the crystallisation of a poly(3-alkylthiophene) (P3AT) polymer. The absorption profile of the thin film immediately after quenching from the melt to 0 ^{o}C features a broad absorption with a single

maximum observed at 464 nm. This is comparable to a dilute solution of regioregular P3HT in a good solvent,[101] or a regiorandom P3HT thin film,[102-104] in both cases indicating a lack of semicrystalline order and an absence of interchain optoelectronic coupling. The blue-shift and the broadness of the absorption profile of the P3EHT film immediately after quenching is therefore confirmation of an amorphous film. The conspicuous red-shift of the absorption peak with time after quenching from the melt indicates an increase in conjugation length. In addition to this increase in conjugation length, the emergence of a vibronic shoulder at a higher wavelength (*ca* 570 nm) indicates the formation of small crystalline regions. It has previously been shown that there exists an isosbestic point in the absorption profiles as time elapses, indicating that the overall absorption profile is a linear combination of the absorption spectra of just two species; the amorphous domains and the crystalline domains. Absorption in the amorphous domains takes place without interchain coupling, resulting in a relatively wide optical bandgap (2.22 eV). In the crystalline domains, interchain coupling forces the polymer backbone to planarise, thereby increasing the conjugation length, reducing the optical bandgap (2.04 eV), and shifting the absorption profile to longer wavelengths.[77] Thus, the overall change in the absorption profile represents a decrease in population of amorphous domains, and an increase in population of crystalline domains.

To the best of our knowledge, this chapter is the first investigation to study the evolution of the HOMO energy level of P3EHT as a function of crystallinity. The observed reduction in optical bandgap associated with the formation of crystalline usually indicates (i) a destabilisation of the HOMO, (ii) a stabilisation of the LUMO, or

(iii) a combination of both effects for crystalline domains with respect to amorphous domains. Cyclic voltammetry performed on a film shortly after quenching reveals two distinct HOMO energy levels at -5.20 eV and -5.26 eV, which are assigned to the crystalline domains and amorphous domains, respectively (as above). Although it was not practically possible to perform CV on a film immediately after quenching, it is expected that the cyclic voltammogram would exhibit only the second oxidation peak, as the film would be completely amorphous. The relative positions of the oxidation peaks representing the two HOMO energy levels do not significantly change as a function of time elapsed after quenching, meaning that the hole driving force discussed above also does not change. However, the relative intensities of the oxidation peaks do vary. The oxidation peak relating to the crystalline domains grows in intensity relative to that of the amorphous domains. Since the peak intensity or current in a cyclic voltammogram is proportional to charge, and therefore population of redox active species, this suggests that amorphous domains are being converted into crystalline domains, which is in good agreement with absorption profile findings.

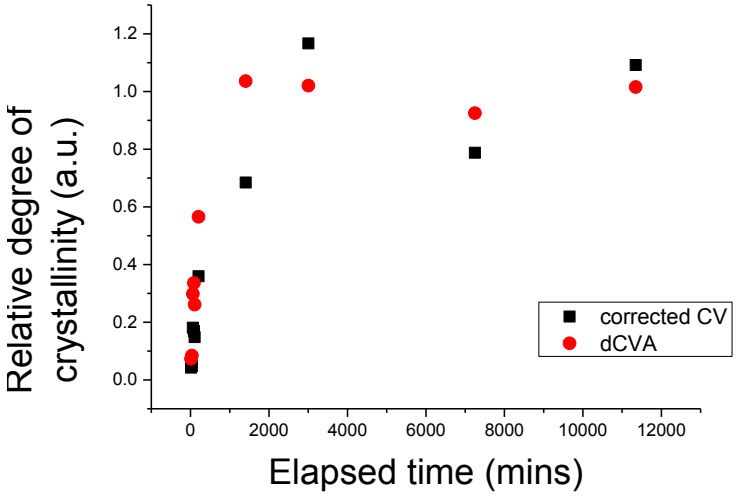

Figure 3.19 - Relative degree of crystallinity (rDOC) as measured by CV and dCVA as a function of time elapsed after thermal quenching. Data is normalised by dividing by the respective degree of crystallinity calculated for the as-spun film.

The ratio of crystalline:amorphous oxidation peak currents is used as an indicator of the relative degree of crystallinity (rDOC) within the film, and is plotted as a function of time in Figure 3.19. Both CV and dCVA plots are normalised for the respective degree of crystallinity calculated for the as-spun film. The rDOC therefore represents the progression of recovery of the amorphous film back to its former as-spun self. The initial increase in the rDOC recovers to 50% of the as-spun rDOC after *ca* 4 hours, and plateaus after *ca* 1 day. This represents a much slower crystallisation process than the 75 mins determined by GI-XRD in a previous study.[98]

In conclusion, cyclic voltammetry has been employed to measure the HOMO energy level of crystalline/aggregate and amorphous domains. An energy offset of 60 meV is observed, which is thought to be significant as it might promote the transfer of hole polarons from less-ordered amorphous domains to more ordered crystalline/aggregate

domains. This could be an important implication in polymer/fullerene solar cells as it might promote charge separation and therefore charge collection.

4

Development of Electrochemical Stability Methodology for Conjugated Polymers

Current understanding of electrochemical stability of conjugated polymers is limited to two approaches; (i) predicting how resistant a polymer is to reaction with oxygen and water, in the absence of light, and (ii) observing the reversibility of a redox process of a polymer using cyclic voltammetry. The former approach is useful in predicting the stability of conjugated polymers under storage, or when a device is not operating. The latter approach attempts to predict the stability of conjugated polymers when oxidised, approximating the hole polaron species present in a blend after charge separation. In order to study the stability of polaronic species in polymer films, across a series of polymers, two important considerations concerning the degradation step must be made: (i) the concentration of polaronic species that are injected into the film, and (ii) the duration for which the polaronic species are injected into the film. In cyclic voltammetry, these considerations are impacted by (i) the experimental set-up (e.g.

upper potential, lower potential, scan-rate, number of cycles), (ii) the MO energy landscape (e.g. how well-defined the voltammogram is, and whether there are shoulders present in the voltammogram), and (iii) the kinetics associated with the redox process involved. The combination of these three factors means that cyclic voltammetry is very limited in its potential to be used as a method of controlling the degree of oxidative stress applied to neat polymer films, across a series of polymers.

This chapter describes the development of a spectroelectrochemical approach, using chronoamperometry and absorption spectroscopy, to probing the electrochemical stabilities of conjugated polymers. Further, we will compare the ability of a series of polymers to recover from being subjected to comparable levels of oxidative stress.

The well-studied poly(3-hexylthiophene), or P3HT, was used in the development of this novel methodology along with two iso-structural polymers; PTTTz and PTTz.[3]

4.1 Introduction

In this chapter, we will describe a new methodology for the evaluation of different semiconducting polymer neat films under bulk oxidative stress conditions, particularly relevant for OLEDs and organic solar cells. In order to develop a methodology that can compare polaron stabilities in different polymer neat films, the relative degree of oxidative stress must be controlled. Chronoamperometry can be used to induce oxidative stress conditions by applying a positive potential to the neat film working electrode. The size of this potential will be largely affected by the difficulty of injecting holes into the bulk film, i.e. the polymer's ionisation potential. An element of this chapter will focus on the process of selecting a potential (herein referred to as the *oxidative stress potential*) for each polymer system, and controlling the relative degree of oxidation stress in the film. The three materials used in the development of this methodology are discussed in the next section.

4.1.1 Polaron Stability of P3HT and its Deeper HOMO Cousins

P3HT is the most widely studied organic semiconductor material, in part due to its relatively easy synthesis, good scalability and ease of processing. Power conversion efficiencies of 2-5% are routinely obtained in bulk heterojunction solar cells when P3HT is blended with [6,6]phenyl-C61-butyric acid methyl ester ($PC_{60}BM$). To date, the vast majority of publications relating to P3HT have focussed on gaining an understanding of the exact processes responsible for charge generation in a P3HT:PCBM system. As a result, a detailed understanding of the various loss mechanisms involved in such solar cells has been gained. Despite the promise of higher

efficiencies from more recent push-pull hybridised donor polymers, P3HT remains a popular material due to its availability, and the ease and low toxicity (and therefore cost) of its synthesis.

In order to investigate and compare polaron stabilities in polymers of different HOMO energy levels, two analogous polymers with deeper HOMO energy levels were synthesised; poly(2-(3',4-dihexyl-[2,2'-bithiophen]-5-yl)-4-hexylthiazole) (PTTTz) and poly(4-hexyl-2-(3-hexylthiophen-2-yl)thiazole) (PTTz).

4.1.1.1 Structure

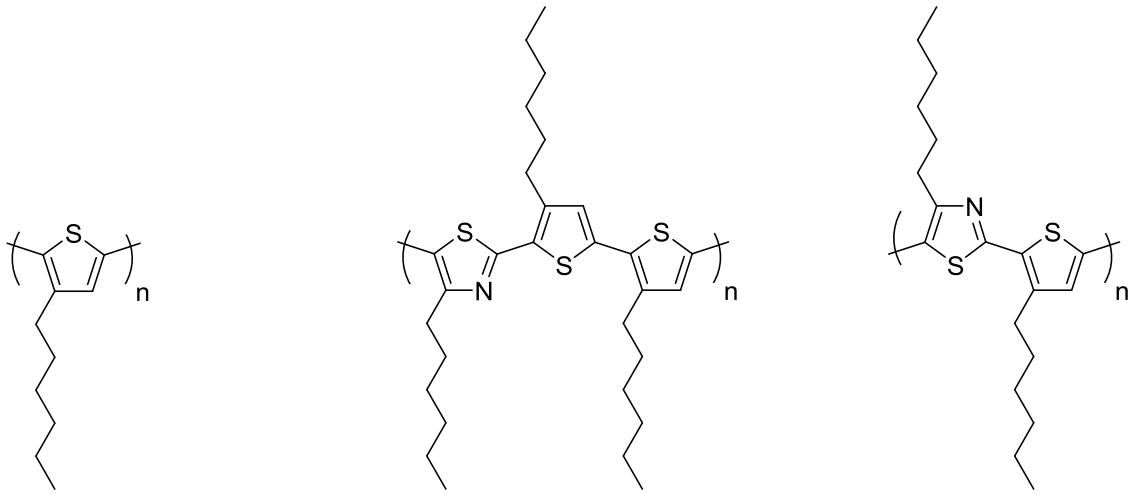

Figure 4.27 – Chemical structures of P3HT (left), PTTTz (centre), and PTTz (right)

Regioregular P3HT is a homo-coupled polymer consisting solely of 3-hexylthiophene monomer units, in which the 5-position carbon atom of each monomer unit is attached to the 2-position carbon atom of the next monomer unit, in a head-tail fashion. PTTTz and PTTz both have almost identical conjugated polymer backbones, with identical side-chain attachment and density, to that of P3HT. As such, these materials should exhibit similar solid state behaviour to P3HT, making them a very suitable polymer

series to study. An obvious structural difference is the substitution of one 4-hexylthiazole monomer unit for every other thiophene unit in PTTz, and for every third thiophene unit for PTTTz, along the polymer backbone. Thiazole has a very similar structure to thiophene; the main structural difference is the substitution of a nitrogen atom into the 4-position of a thiophene ring. The numbering of atoms within the thiazole ring is the mirror-image of that in thiophene due to the higher priority of the nitrogen atom, and so the nitrogen atom is in the 3-position in thiazole. Aside from the complication of the nomenclature involved, the introduction of the relatively electron-deficient thiazole unit was designed to stabilise the HOMO of the polymer, which is a well-established synthetic strategy in conjugated polymer synthesis.[63,64,105-107] This effect is predicted to be more pronounced in PTTz since it has a bigger ratio of thiazole:thiophene (1:1) than PTTTz (1:2).

4.1.1.2 Physical and electrochemical properties

The physical properties of PTTTz and PTTz are listed in Table 4.6.

Table 4.6 - Physical properties of PTTTz and PTTz. [a]Determined by GPC(TCB) against PS standards. [b]Determined from ^{1}H NMR spectra. [c]Determined by photoelectron spectroscopy in air (PESA). [d]Determined from the HOMO and optical gap.

Polymer	**M_n / kDa**[a]	**M_w / kDa**[a]	**PDI**[a]	**RR / %**[b]	**HOMO / eV**[c]	**LUMO / eV**[d]
P3HT	43	78	1.8	98	-4.90	-2.97
PTTTz	21	45	2.2	93	-5.02	-3.12
PTTz	27	51	1.8	90	-5.15	-3.25

The molecular weights of both novel polymers are reasonably high and comparable to that of the regioregular P3HT used.

The absorption spectra of PTTTz and PTTz in solution and as a thin film have been studied in-house.[108] Both materials have very similar absorption profiles. In solution, a single featureless absorption is observed for both materials at 450 nm, which is assigned to the π−π transitions of the polymer backbone. In the thin film, the absorption maxima are significantly red shifted to *ca* 550 nm, as well as several shoulders appearing, which are attributed to the formation of microcrystalline domains with a coplanar intrachain conformation.[109] The similarity of both the solution and thin film UV−vis spectra to those of P3HT indicates that the novel materials behave in a very similar manner in the solid state, and are therefore comparable.

Estimates for HOMO energy levels of all three polymers were initially determined using photoelectron spectroscopy in air (PESA) measurements. As predicted, the introduction of thiazole, and therein increasing the thiazole content along the polymer backbone leads to stabilisation of the HOMO, across this polymer series. It follows that the introduction of thiazole leads to PESA estimates for the HOMO energy level of PTTz being *ca* 0.3 eV more stable than that of P3HT. Similarly, PTTTz has a lesser thiazole content than PTTz, and so this stabilisation is seen to be less pronounced in the case of PTTTz.

Thus, the similarities in physical properties and the spread of HOMO energy levels make this polymer series suitable for developing a methodology that investigates polaron stability of semiconducting polymers.

4.2 Experimental

4.2.1 Materials and reagents

P3HT was synthesised and purified by recycling GPC in-house by Dr Weimin Zhang. PTTTz and PTTz were both synthesised in-house by Dr Hugo Bronstein and Michael Hurhangee using standard GRIM type conditions and purified by GPC, affording dark purple polymers.[110] P3HT was dissolved in chloroform (5 mg mL^{-1}), by stirring it at room temperature for 1 hour, giving a clear orange solution. PTTTz was dissolved in chlorobenzene (5 mg mL^{-1}), by stirring it at 60 ^{o}C for 1 hour, giving a clear orange solution. PTTz was dissolved in *ortho*-dichlorobenzene (5 mg mL^{-1}), by stirring it at 80 ^{o}C for 1 hour, giving a clear orange solution. All solutions were heated and/or stirred on a stirrer/hot-plate. All dry chlorinated solvents were prepared by bubbling dry argon gas through the solvent for 10 minutes.

4.2.2 Thin film deposition

Neat polymer thin films were deposited on clean masked FTO glass substrates, and then dried under vacuum, using the spin-coating technique described in **Chapter 2.1.1**.

4.2.3 Frontier Orbital energy level determination

4.2.3.1 Preparation

The dry neat polymer thin films on FTO glass formed the working electrode as part of the three-electrode spectroelectrochemical cell described in **Chapter 2.3.1**. Supporting electrolyte solutions were degassed with dry argon for 10 minutes before being

transferred to the spectroelectrochemical cell, which was already under an argon atmosphere. The argon atmosphere was maintained in the cell, throughout measurements, by applying a gentle flow of argon over the solution. All experiments were carried out at room temperature. The cell was thoroughly rinsed with water, soapy water, acetone, and then *iso*-propyl alcohol, before being dried for 5 minutes with a strong flow of nitrogen.

4.2.3.2 Measurement

Cyclic voltammetry was used to probe the HOMO, and therefore obtain an estimate of its energy level, for each polymer, as described in **Chapter 2.3.2.1**. The parameter used to set up the cyclic voltammetry measurements are given in Table 4.7.

Table 4.7 - Cyclic voltammetry parameters used to probe the oxidation potential of P3HT, PTTTz, and PTTz. Potentials are given with respect to Ag/AgCl reference electrode.

Polymer	**P3HT**	**PTTTz**	**PTTz**
Upper potential/ V	+1.20	+1.20	+1.30
Lower potential/ V	0.00	0.00	0.00
Stop potential/ V	0.00	0.00	0.00

Since the shape and position of oxidation features in CV can be affected by scan rate, a scan rate of 20 mV s^{-1} was used for all CV scans. Oxidation onset potentials (with respect to Ag/AgCl reference electrode) were determined by taking the intercept of one tangent off the background current and a second tangent off the rising current. The half-wave potential of ferrocene (Fc/Fc^{+}) was found to be +0.44 V, with respect to Ag/AgCl

reference electrode. Frontier Orbital energy levels were estimated from the oxidation onset potentials (with respect to Fc/Fc^+) using the following equation:

$$E_{HOMO} = -\left(E_{ox.,onset\ vsFc/Fc+} + 4.8\right)$$

where E_{HOMO} is the HOMO energy level and $E_{ox.,\ onset\ vs\ Fc/Fc^+}$ is the onset of oxidation versus the half-potential of the Fc/Fc^+ reference electrode.

4.2.4 Spectroelectrochemistry

4.2.4.1 Preparation

Pristine dry neat thin films on FTO glass were fabricated for each polymer in an identical procedure to that used in **3.2.3**. The dry neat polymer thin films on FTO glass formed the working electrode as part of the three-electrode spectroelectrochemical cell described in **Chapter 2.3.1**. Supporting electrolyte solutions were degassed with dry argon for 10 minutes before being transferred to the spectroelectrochemical cell, which was already under an argon atmosphere. The argon atmosphere was maintained in the cell, throughout measurements, by applying a gentle argon flow over the solution. All experiments were carried out at room temperature. The cell was thoroughly rinsed with water, soapy water, acetone, and then *iso*-propyl alcohol, before being dried for 5 minutes with a strong flow of nitrogen.

4.2.4.2 Measurement

Chronoamperometry was used to produce spectroelectrochemical data by measuring absorption profiles, in the wavelength range 400-1100 nm, of the polymer film as a function of potential applied to the working electrode. The same polymer film sample

was used to produce the series of spectroelectrochemical data. The parameters used in the chronoamperometry measurements are given in Table 4.8.

Table 4.8 - Chronoamperometry parameters used to oxidise polymer neat film for spectroelectrochemical measurements. V_0, V_1, and V_2 are the initial potential, oxidising potential, and final potential, respectively. These potentials were applied for a time of T_0, T_1, and T_2, respectively.

V_0/ V	0.00
T_0/ s	15
V_1/ V	V_{probe}
T_1/ s	60
V_2/ V	0.00
T_2/ s	60

The initial potential applied to the working electrode (V_0) is chosen such that the polymers being investigated show no redox reactivity. A potential of 0.00 V is neither negative enough to reduce, nor positive enough to oxidise the polymers being studied, and hence the polymers have a neutral charge at 0.00 V. The probing potential (V_{probe}) is increased between scans from 0.00 V by 0.10 and/or 0.05 V increments. The potential applied to the working electrode is ramped from 0.00 V to V_{probe}, and held at this potential for a total time of 1 minute. An absorption spectrum measurement is initiated 10 s after the working electrode potential is ramped, which takes approximately 40 s to complete its scan. After 60 s at V_{probe}, the potential is ramped down to 0.00 V and held at this potential for 60 s in order to remove any positive charges that may have been induced in the film during the V_{probe} regime. This process was repeated for increasing

values of V_{probe} to produce a series of absorption spectra as a function of working electrode potential, for each polymer neat film.

4.2.5 Polaron stability

4.2.5.1 Preparation

Pristine dry neat thin films on FTO glass were fabricated for each polymer in an identical procedure to that used above. The dry neat polymer thin films on FTO glass formed the working electrode as part of the three-electrode spectroelectrochemical cell described in Chapter 2.3.1. Supporting electrolyte solutions were degassed with dry argon for 10 minutes before being transferred to the spectroelectrochemical cell, which was already under an argon atmosphere. The argon atmosphere was maintained in the cell, throughout measurements, by applying a gentle argon flow over the solution. All experiments were carried out at room temperature. The cell was thoroughly rinsed with water, soapy water, acetone, and then *iso*-propyl alcohol, before being dried for 5 minutes with a strong flow of nitrogen.

4.2.5.2 Measurement

Chronoamperometry was used to apply an oxidising potential, herein referred to as the *oxidative stress potential* ($V_{ox.\ stress}$), to the working electrode. $V_{ox.\ stress}$ was defined as that potential that caused the absorption intensity of the polymer's main absorption peak to reduce to 75% of its initial intensity, which was determined using its spectroelectrochemical data. Absorption spectra were recorded after time intervals at 0.00 V, and give the absorption profile as a function of total oxidative stress time. The

same polymer film sample was used to produce a series of absorption spectra as a function of oxidative stress time. The following chronoamperometry parameters were used in the production of each spectrum:

Table 4.9 – Chronoamperometry parameters used to oxidise polymer neat films for stability measurements. V_0, V_1, and V_2 are the initial potential, oxidative stress potential, and final potential, respectively. These potentials were applied for a time of T_0, T_1, and T_2, respectively.

V_0/ V	0.00
T_0/ s	15
V_1/ V	$V_{ox.\ stress}$
T_1/ s	$T_{ox.\ stress}$
V_2/ V	0.00
T_2/ s	60

The initial potential applied to the working electrode (V_0) is 0.00 V for the same reasons discussed in 4.2.4.2. The working electrode potential is then ramped to the pre-determined oxidative stress potential. The values used for T_1, and consequently the total oxidative stress time, are given in Table 4.10.

Table 4.10 - Sequence of times (T_1) used to hold polymer films at the oxidative stress potential during the oxidative stress stage of chronoamperometry measurement. The resultant cumulative oxidative stress time is also given.

Measurement	**T_1/ s**	**Cumulative oxidative stress time / s**
1	30	30
2	30	60
3	60	120
4	180	300
5	300	600
6	400	1000
7	500	1500
8	1500	3000
9	3000	6000
10	4000	10000

4.3 Results

4.3.1 Fabrication of polymer neat films on FTO glass substrate

P3HT

Stirring P3HT (0.2 mg) in degassed, dry chloroform (1 mL) at room temperature resulted in a clear, bright orange solution. Spin-coating the orange solution onto a clean, dry FTO glass substrate resulted in a purple thin film. The absorption spectrum of P3HT (Figure 4.28, top) exhibits an absorption maximum at a wavelength of 518 nm, which is accompanied by several shoulders.

PTTTz

Stirring PTTTz (0.2 mg) in degassed, dry chlorobenzene (1 mL) at room remperature resulted in a dark purple solution. Stirring the solution whilst heating to 60 °C caused the solution to become clear and bright orange, comparable to the solution obtained for P3HT. Spin-coating the orange solution onto a pre-heated clean, dry FTO glass substrate resulted in a purple thin film that was indistinguishable from that obtained for P3HT with the naked eye. The absorption spectrum of PTTTz (Figure 4.28, middle) exhibits an absorption maximum at a wavelength of 550 nm, which is accompanied by several shoulders.

PTTz

Stirring PTTz (0.2 mg) in degassed, dry *ortho*-dichlorobenzene (1 mL) at room temperature resulted in a dark purple solution, similar to that initially obtained for

PTTTz. Stirring the solution whilst heating to 80 °C caused the solution to become clear and bright orange, which was also comparable to the solution obtained for P3HT. Spin-coating the orange solution onto a pre-heated clean, dry FTO glass substrate resulted in a purple thin film that was also indistinguishable from that obtained for P3HT. The absorption spectrum of PTTz (Figure 4.28, bottom) exhibits an absorption maximum at a wavelength of 546 nm, which is accompanied by several shoulders.

The absorption spectrum of a pristine FTO glass substrate was measured and subsequently subtracted from all polymer film absorption spectra. All absorption spectra were found to be stable when polymer neat films were stored in the absence of light and in dry conditions before electrochemical measurements were carried out.

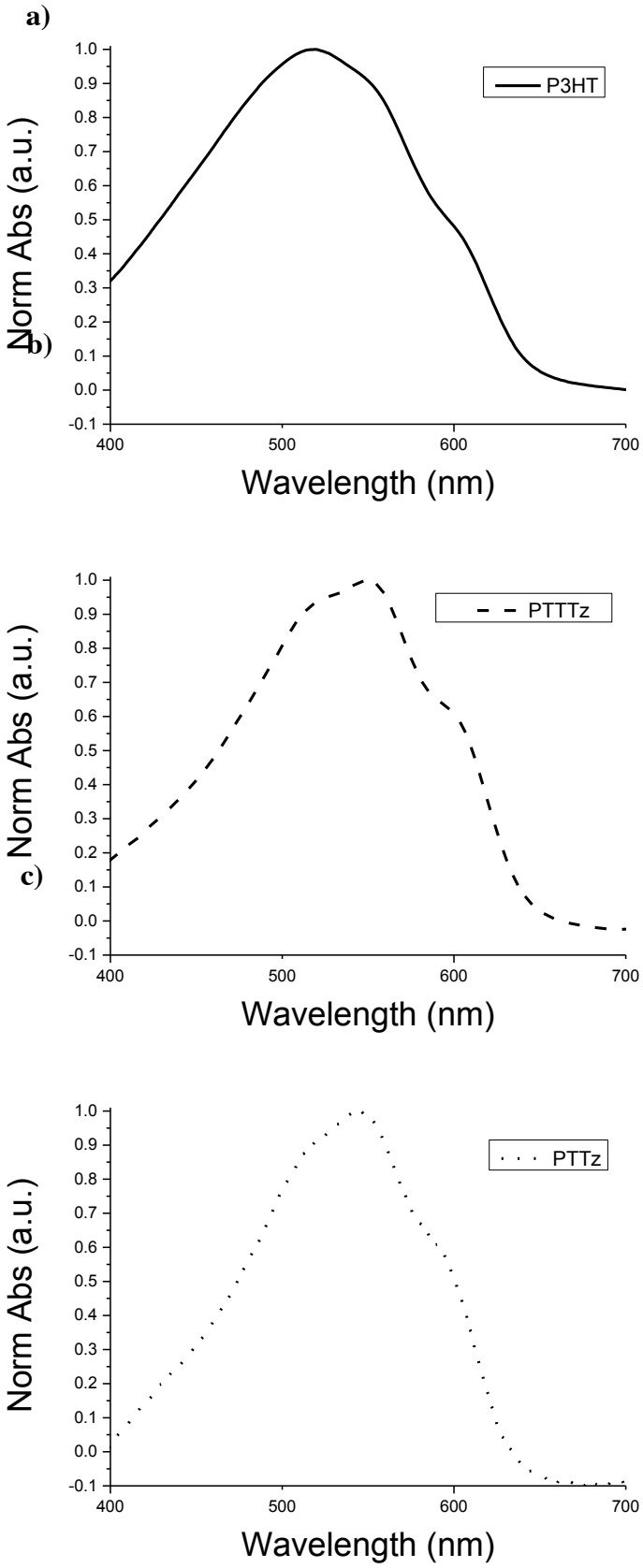

Figure 4.28 – Absorption spectra of neat films of a) P3HT, b) PTTTz, and c) PTTz. Polymers were spin-coated on FTO glass substrates. A background spectrum of a blank FTO glass substrate was subtracted from all measurements.

4.3.2 Spectroelectrochemistry

After drying under vacuum overnight, the films were each incorporated as the working electrode in a spectroelectrochemical cell. Spectroelectrochemical data is shown in Figure 4.29 for varying degrees of oxidation of P3HT, PTTTz and PTTz films. In the case of P3HT, the application of potentials up to and including +0.40 V vs Ag/AgCl had no effect on the absorption spectrum. An applied potential of +0.50 V gives rise to two observations; (i) a reduction in the absorption intensity between 400 and 600 nm, which is attributed to a reduction in the population of unoxidised (neutral) polymer, and (ii) formation of a broad absorption at *ca*. 800 nm, which is attributed to the oxidation of the polymer, i.e. the formation of hole polarons. This suggests that the onset potential for oxidation of P3HT lies in the range +0.40-0.50 V. Upon the application of increasingly more positive potentials, both noted phenomena become increasingly more pronounced, i.e. the absorption intensity between 400 and 600 nm decreases further, and the broad absorption at *ca*. 800 nm grows in intensity. The degree to which the absorption intensity at the absorption maxima decreases is used as an indicator to the degree of oxidation of the polymer film. PTTTz displayed similar behaviour to P3HT under similar spectroelectrochemical conditions. PTTTz showed no spectroelectrochemical response, between 400 and 1100 nm, under applied potentials up to and including +0.40 V. The application of +0.50 V gives rise to the same two spectroelectrochemical observations, as described for P3HT. Interestingly, the spectroelectrochemical response of PTTTz at +0.50 V is less pronounced than that of P3HT at +0.50 V. More specifically, (i)the drop in absorption intensity at absorption maxima is observed to be 5% for P3HT (at 518 nm), compared to 1% for PTTz (at 550

nm), and (ii) there is no significant increase in absorption intensity at *ca*. 800 nm for PTTTz, compared to a small increase (2%) for P3HT. At increasingly more positive potentials, the magnitude of the spectroelectrochemical response of PTTTz continued to lag behind that of P3HT. PTTz displayed similar behaviour to both P3HT and PTTTz under similar spectroelectrochemical conditions. The main difference between PTTz and the other two polymers is that it shows no spectroelectrochemical response up to and including +0.50 V. An applied potential of +0.60 V gives rise to the same two spectroelectrochemical observations, as described for P3HT and PTTTz at +0.50 V. This suggests that the potential relating to the onset of spectroelectrochemical response for PTTz lies between +0.50 V and +0.60 V. Upon the application of increasingly more positive potentials, both noted phenomena become increasingly more pronounced.

Across the polymer series, both the reduction in absorption intensity between 400 and 600 nm and the increase in absorption intensity at *ca*. 800 nm are reversible changes for smaller (less oxidising) applied potentials, over the timescale of the experiment, i.e. the initial absorption spectrum (not shown) is reproduced after the smaller applied potentials are removed. At larger (more oxidising) applied potentials, the reduction in absorption intensity between 400 and 600 nm is less reversible, suggesting degradation in the polymer structure. Conversely, the increase in absorption intensity at 800 nm remains reversible (Figure 4.30) suggesting that holes are successfully removed from the polymer film. For P3HT, the normalised absorption at 518 nm recovers to 98% of its initial intensity, after the spectroelectrochemical experiment. For PTTTz, the normalised absorption at 550 nm recovers to 73% of its initial intensity, after the

spectroelectrochemical experiment. For PTTz, the normalised absorption at 546 nm recovers to 67% of its initial value.

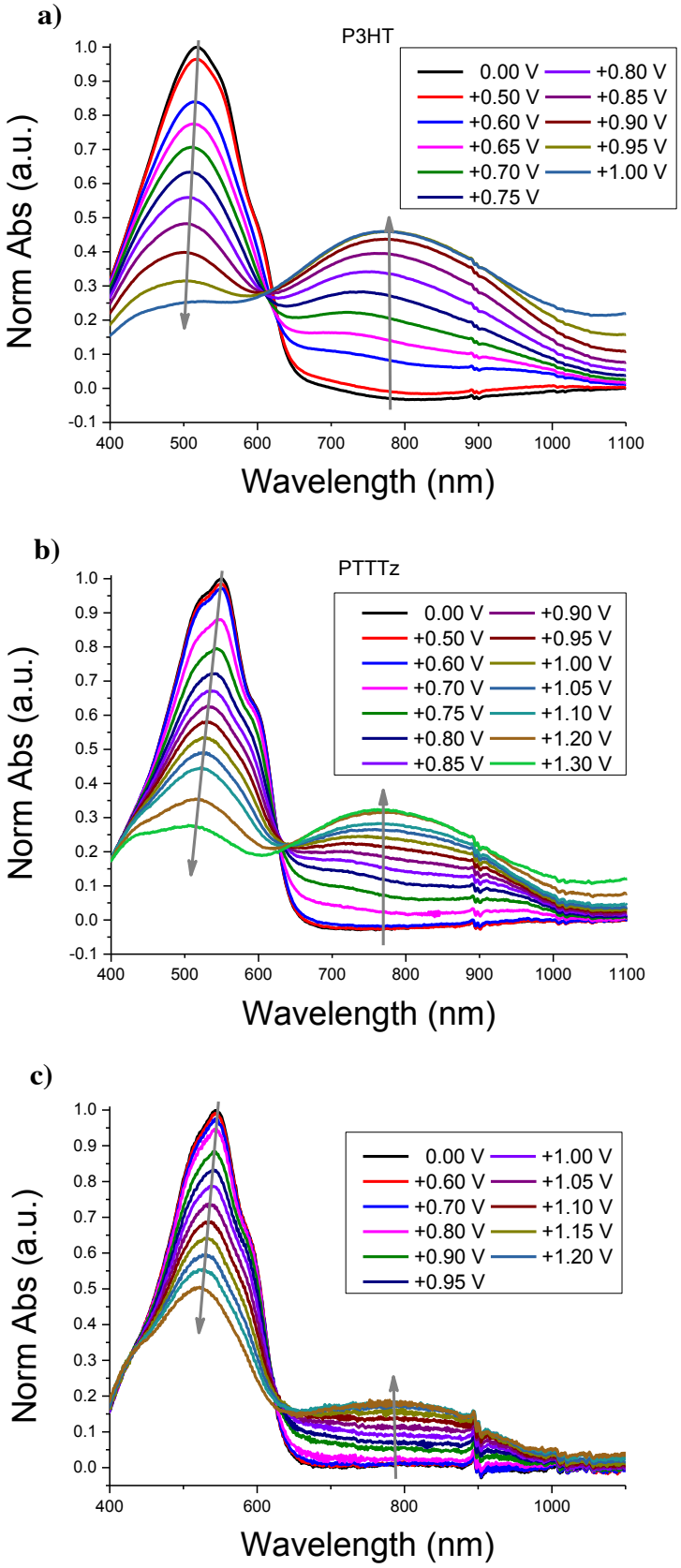

Figure 4.29 - Spectroelectrochemical data for neat films of a) P3HT, b) PTTTz, and c) PTTz. A background absorption spectrum consisting of a blank FTO glass substrate, submerged in 0.1 M $TBAPF_6/CH_3CN$ electrolyte solution, was subtracted from all absorption spectra.

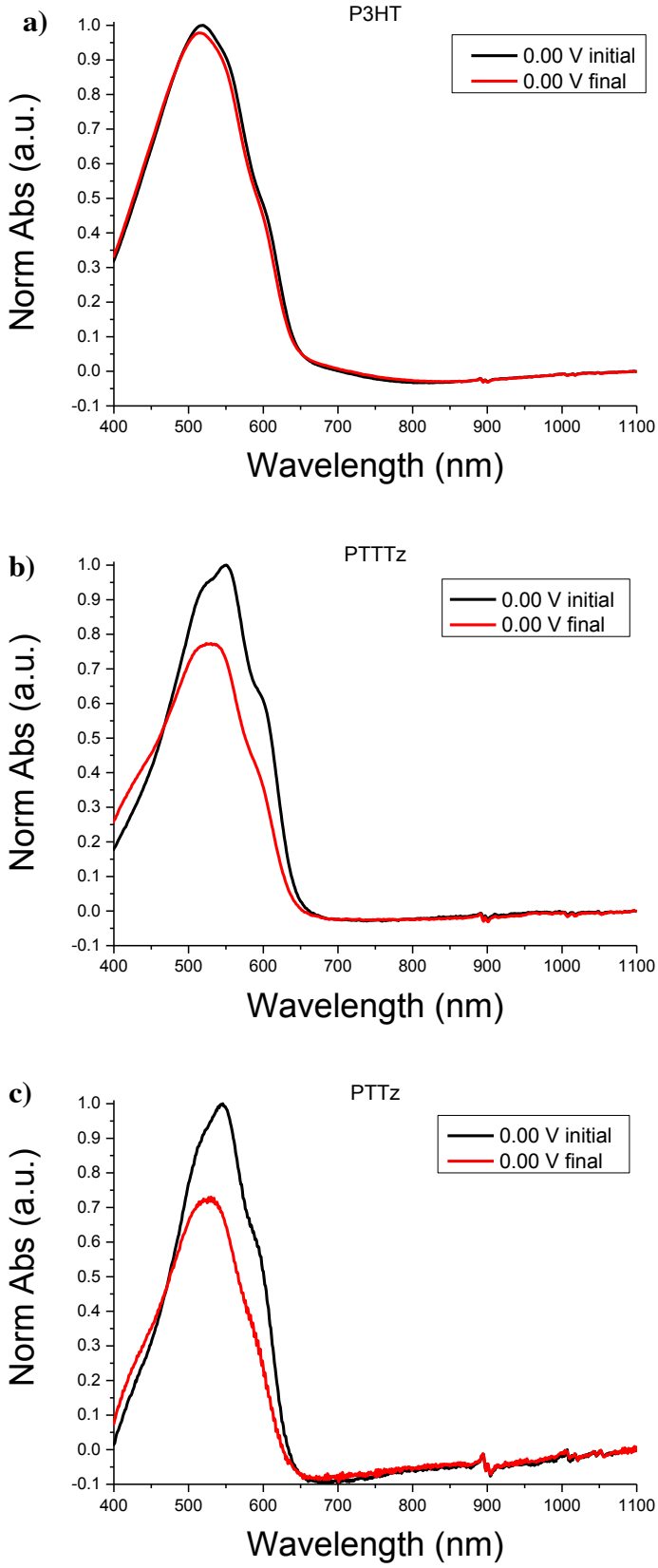

Figure 4.30 - Normalised absorption spectrum before and after spectroelectrochemical experiment for a) P3HT, b) PTTTz, and c) PTTz. Absorption spectra were measured using the same procedure as for the spectroelectrochemical experiment.

4.3.3 Cyclic Voltammetry

Cyclic voltammetry was carried out on pristine neat polymer films, across the polymer series, in order to obtain an estimate for HOMO energy level of each polymer. Neat films were fabricated using the same conditions as described previously for the spectroelectrochemistry study. Typical voltammograms are given for P3HT, PTTTz and PTTz in Figure 4.31, all performed with a scan rate of 20 mV s^{-1}. Multiple redox events occur for each polymer within the potential window studied. For each of the three polymers, the first redox event is not well-defined, and hence it is not trivial to determine the half-wave potential relating to the HOMO energy level. An alternative method of determining HOMO energy levels takes into account the potential at which the onset of oxidation occurs. The onset potential is determined by the intersection of the background current (near horizontal) and the tangent of the oxidation peak that occurs at the lowest applied potential (furthest to the left). This intersection is displayed in the inset of each voltammogram. The onset potentials, across the polymer series are determined to be at +0.44, +0.76, and +0.83 V for P3HT, PTTTz, and PTTz, respectively. It is interesting that these onset potentials follow the same trend across the polymer series as observed in the spectroelectrochemical study (above). These onset potentials can be processed to give HOMO energy levels of -4.80 eV, -5.12 eV, and -5.19 eV. This stabilisation of the HOMO energy level as thiazole content is increased along the polymer backbone is in good agreement with previous PESA measurements and DFT calculations.[108]

Figure 4.32 compares the spectroelectrochemical response of each of the polymers as a function of applied potential. Plotting the normalised absorption intensity at the initial

absorption maximum wavelength, as a function of applied potential, gives a good indication of how the population of neutral polymer in the film is affected by potential. Another advantage that optical measurements have over CV in monitoring the relative population of a redox species is the relative ease of removing optical background noise as opposed to removing background currents. The plot is used to determine a potential, for each polymer, at which the population of neutral polymer in the film is reduced to 75% of its initial value at 0.00 V. This potential is the aforementioned *oxidative stress potential* ($V_{ox.\ stress}$), and is given for each polymer in Table 4.11.

Table 4.11 – Oxidative stress potentials of polymer neat films as determined from Figure 4.32.

Polymer	**P3HT**	**PTTTz**	**PTTz**
$V_{ox.\ stress}$ / V	+0.65	+0.80	+1.05

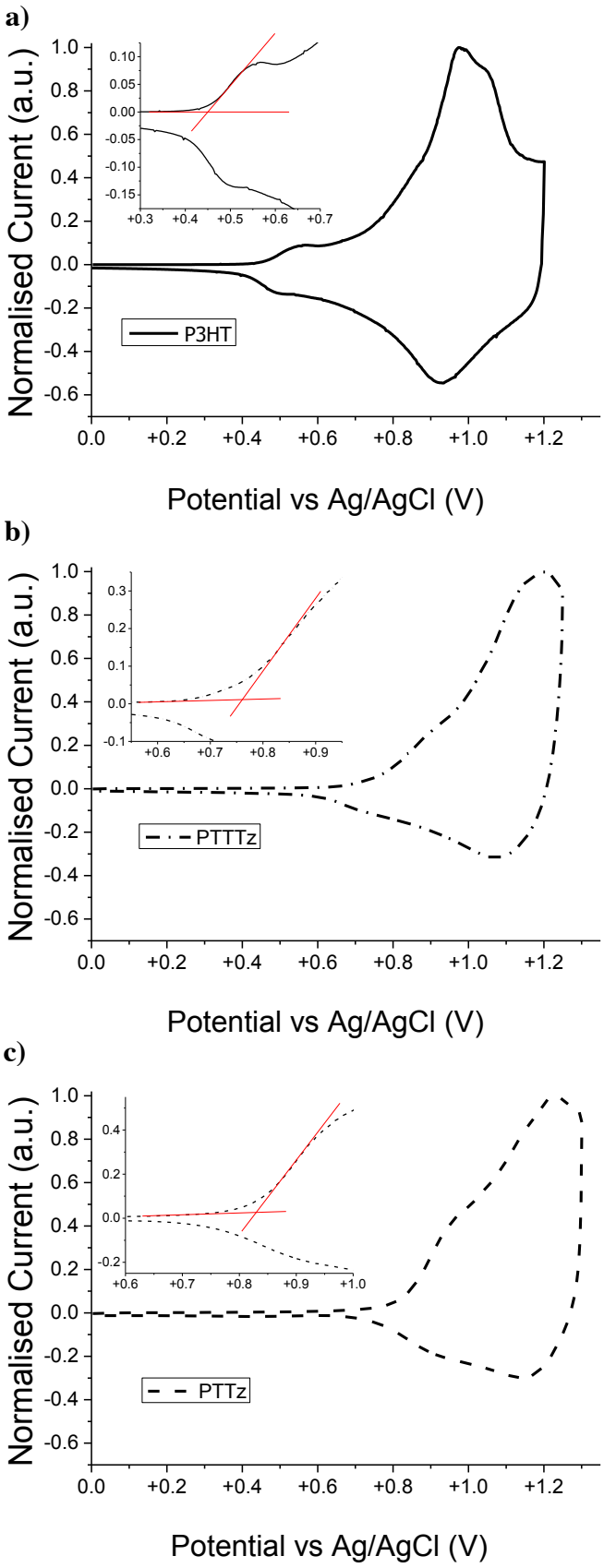

Figure 4.31 - Cyclic voltammograms of a) P3HT, b) PTTTz, and c) PTTz. Insets demonstrate the method used to determine oxidation onset potential: the intersection is taken between the background current and a tangent drawn off the rising current.

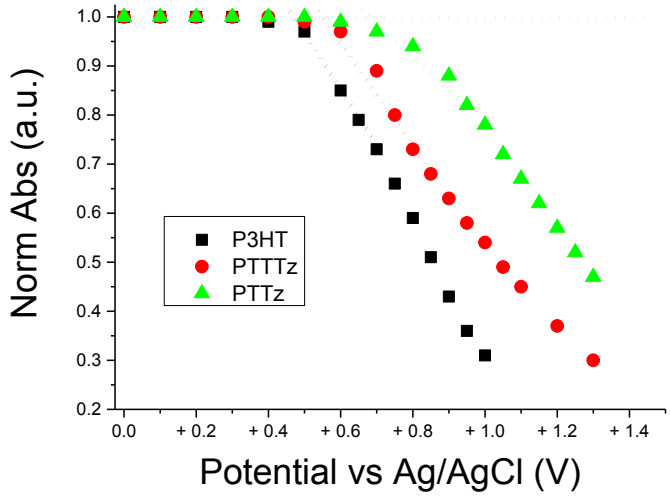

Figure 4.32 - Comparison of change in normalised absorption intensity at main peak absorption maxima of P3HT (black), PTTTz (red), and PTTz (green). Plotted data is take from spectroelectrochemical measurements in Figure 4.29.

4.3.4 Electrochemical degradation of polymer films

Chronoamperometry is used to inject positive charge into the polymer films, in a set-up similar to that used in **4.3.2**. The probing potential is applied to the film to provide an oxidative stress. The absorption spectrum of the film held at 0.00 V (with the oxidative stress removed) was recorded as a function of total oxidative stress time.

4.3.4.1 Effect of oxidative stress potential on relative electrochemical degradation rates

Before carrying out a comparative study of the electrochemical degradation across the polymer series, the effect of oxidative stress potential on the relative rate of degradation was investigated for neat films of PTTz. Three potentials were investigated that induced a drop in peak absorption intensity (λ=546 nm) by 10% (+0.85 V), 25% (+1.05 V), and 50% (1.30 V), which is shown in Figure 4.35.

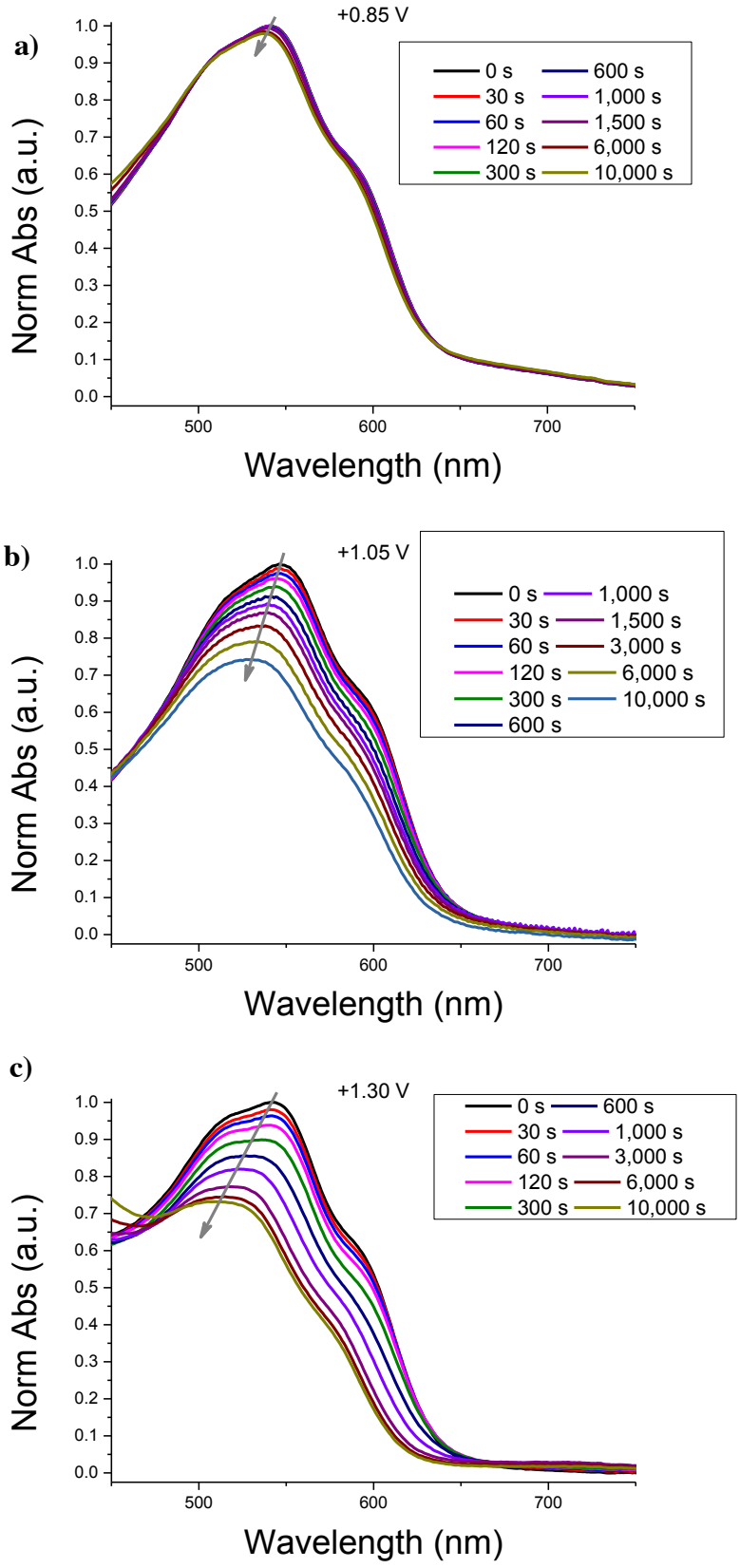

Figure 4.33 - Electrochemical degradation of neat films of PTTz with oxidative stress potentials of a) +0.85 V, b) +1.05 V, and c) +1.30 V, as a function of oxidative stress time.

The absorption spectrum was found to be stable over the timescale of this experiment when the working electrode was held at 0.00 V. This suggests that the polymer is stable in the electrochemical set-up, submerged in electrolyte solution, and that any degradation in the absorption profile in subsequent studies is due to the presence of holes. The less oxidising potential (+0.85 V) results in a very small change to the absorption profile. The absorption peak intensity drops by just 2% and blue-shifts by *ca* 3 nm, with the overall absorption profile retaining its shape after just under 3 hours. At the intermediate potential (+1.05 V) a more conspicuous degradation in the absorption profile is observed; the absorption intensity at 546 nm drops by 30% of its initial value and the absorption peak blue-shifts by *ca* 20 nm. The overall shape of the absorption profile becomes broader, but still retains some of the vibronic character evidenced by the shoulder at *ca* 600 nm. The evolution of the main absorption peaks are attributed to a reduction in conjugation length, and is not comparable with the spectroelectrochemical data provided in Figure 4.29; the broad absorption at *ca*. 800 nm is absent in the degradation studies, which indicates that the injected hole polarons from the oxidative stress regime have been removed at 0.00 V. A more pronounced degradation is observed for the most oxidising potential (+1.30 V); the peak absorption intensity drops by 37% of its initial value and the absorption peak blue-shifts by *ca* 30 nm. The overall shape of the absorption profile becomes broader still, with a greater loss in definition of the vibronic shoulder than for the lower oxidative stress potentials. Figure 4.34 highlights the effect that relative degree of oxidative stress has on degradation rate and therefore the importance of selecting an oxidative stress potential for each polymer system that induces the same relative degree of oxidative stress across a polymer series.

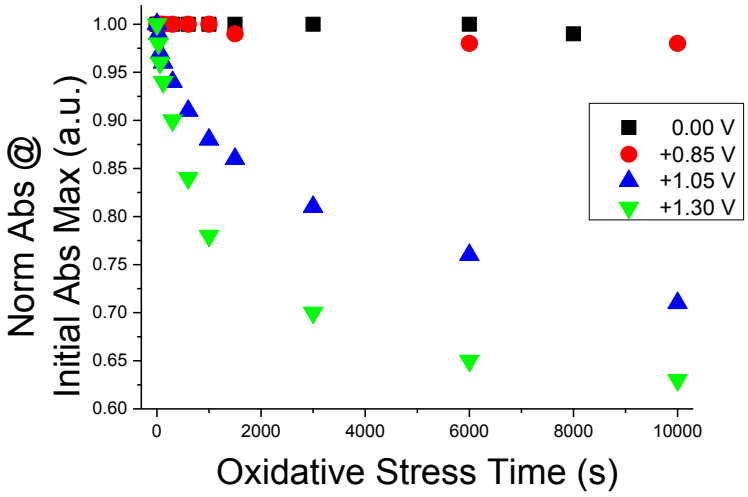

Figure 4.34 – Comparison of relative degradation rates for neat films of PTTz using different values of oxidative stress potential; 0.00 V (0% oxidation), +0.85 V (10% oxidation), +1.05 V (25% oxidation), and +1.30 V (50% oxidation).

4.3.4.2 Electrochemical stability comparison across polymer series

The electrochemical degradation of polymer neat films was investigated across the polymer series including P3HT, PTTTz, and PTTz, and is shown in Figure 4.35. A blue-shift and a reduction in intensity around the absorption maxima were generally observed for all three polymers. P3HT displays the least amount of degradation across the series; the absorption intensity at 517 nm drops by 12% and the absorption peak blue-shifts by 8nm after nearly 3 hours of degradation. The overall shape of the absorption profile remains largely unchanged. PTTTz displays more degradation than P3HT, but less than that for PTTz (described in 4.3.4.1); the absorption intensity at 548 nm drops by 14%, which is comparable to that of P3HT. However, there is a larger blue-shift of 15 nm to the absorption maximum. The overall shape of the absorption profile becomes broader, but still retains some of the vibronic character evidenced by the shoulder at *ca* 600 nm. Figure 4.36 compares the evolution of the absorption intensity at the initial peak absorption wavelength for P3HT, PTTTz, and PTTz, and is plotted from data in Figure 4.35.

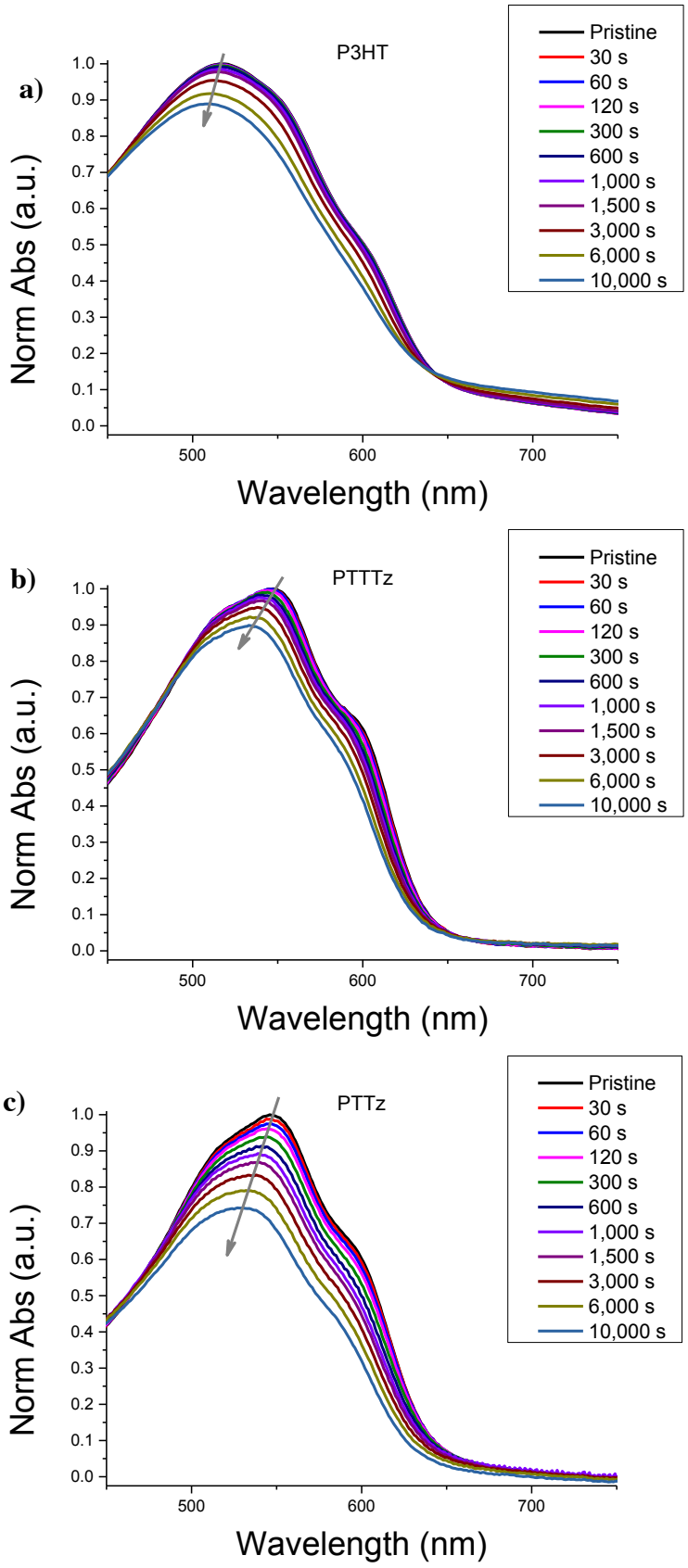

Figure 4.35 – Normalised absorption spectra of neat films of a) P3HT, b) PTTTz, and c) PTTz, as a function of time held at respective degradation potential, displaying electrochemical degradation.. Degradation potentials of a) +0.65 V, b) +0.80 V, and c) +1.05 V were used (see Table 4.11). Electrochemical degradation is generally observed by an irreversible reduction in absorption intensity of and a blue-shift of the main absorption peak. A grey arrow is included to make this observation more explicit to the reader.

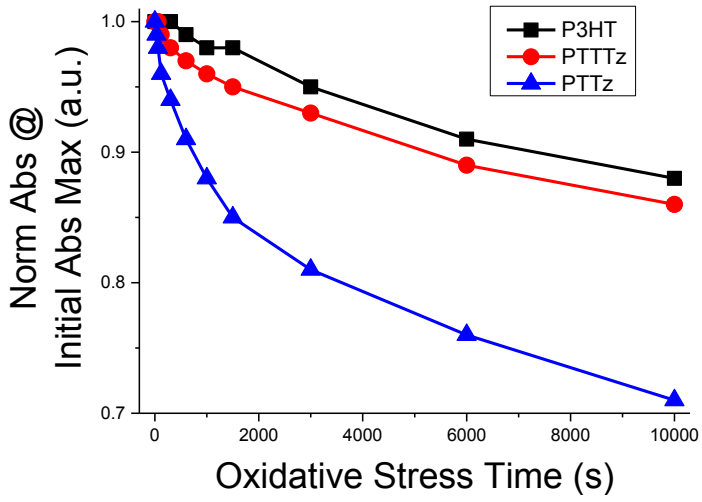

Figure 4.36 - Comparison of normalised absorption intensity at initial absorption maximum wavelength, as a function of oxidative stress time, for P3HT, PTTTz, and PTTz. Data is plotted from Figure 4.35.

Figure 4.36 displays the normalised absorption intensity at the initial absorption maximum wavelength as a function of time, which is used as an indication of relative degree of electrochemical degradation. Over the course of nearly 3 hours of oxidative stress, relative degree of electrochemical degradation is consistently greater than that of PTTTz, which in turn is consistently greater than that of P3HT.

Raman spectroscopy was performed on pristine and degraded samples of PTTz by Jess Wade.

Raman spectroscopy was performed on a pristine PTTz film and on a PTTz film held under oxidative stress (25%) for nearly 3 hours (Figure 4.37). Vibrational modes were assigned to an oligomer PTTz using DFT with a B3LYP Hybrid Functional and a 6-31 G(d,p) basis set. Two signals are observed at 1450-1490 cm^{-1} and 1330 cm^{-1} which are assigned to C=C ring stretching and C-C skeletal stretching, respectively, in both pristine and degraded films. Pristine PTTz films exhibit a third signal at 1500 cm^{-1}, which is attributed to the C=N stretch.

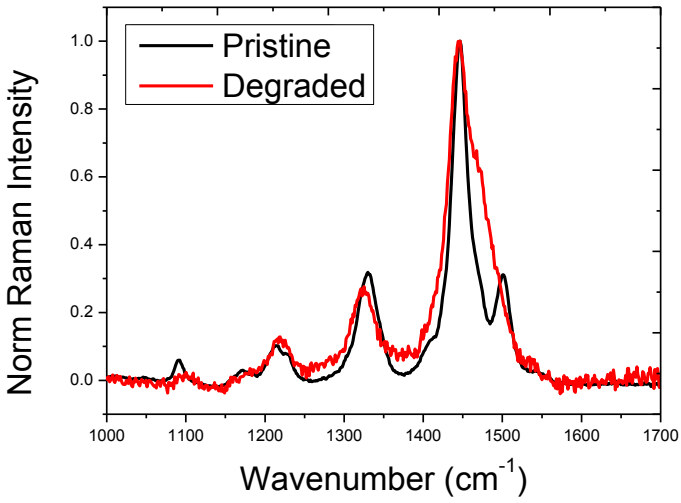

Figure 4.37 – Background corrected and normalised Raman spectra of pristine and degraded films of PTTz. An oxidative stress potential of +1.05 V was used to electrochemically degrade the film. [Figure taken directly from collaborative publication with Jessica Wade. Raman measurements performed by Jessica Wade.[3]]

4.4 Discussion

We have successfully designed a new methodology for investigating the effect of applying an oxidative stress to a semiconducting polymer neat film. Controlling the relative degree of oxidation of the polymer film using chronoamperometry has made it possible to execute a comparative study of polaron stability, through accelerated electrochemical degradation, across a series of polymers with different HOMO energy level landscapes.

In order to control the relative degree of oxidation through chronoamperometry, it was important to first understand the effect of applied potential on the population of neutral polymer species. Consider the Beer-Lambert law,

$$A = \varepsilon . c . l$$

where A is the absorbance, ε is the molar extinction coefficient, c is the concentration of the analyte species, and l is the path length of analyte species that the probe light beam has to travel through. We can assume that the polymer's chemical structure and its electronic structure are both stable in its neutral form during measurement of its absorption spectrum. The extinction coefficient (ε) can be described as the probability of a certain electronic transition occurring, and is affected by electronic structure. Thus the extinction coefficient should be a constant. The path length is essentially the thickness of the polymer film, which is also assumed to remain constant. It is therefore concluded that absorbance at the main polymer peak absorption wavelength is proportional to the concentration of neutral polymer, and therefore the population of

neutral polymer, e.g. a 10% reduction in absorption intensity upon application of an oxidising potential corresponds to a 10% reduction of the neutral polymer population. The oxidative stress potential used in the comparative polaron stability investigation was somewhat arbitrarily chosen such that 25% of the polymer film was oxidised upon application. Smaller degrees of oxidation were found to result in degradation rates that were too slow for experimental convenience. It was also considered that larger degrees of oxidation might result in unrealistically high hole polaron concentrations. Integration of the chronoamperometric curve (data not shown) relating to the oxidative stress regime indicated that a 25% degree of oxidation corresponded to an initial hole concentration of *ca* 10^{20} cm^{-3}. This is a few orders of magnitude higher than that typically found in OSCs and OLEDs ($10^{15\text{-}17}$ cm^{-3}), and in OFETs (10^{18} cm^{-3}), and therefore represents an accelerated degradation methodology.

Upon application of oxidative stress, absorption profiles generally exhibit a blue-shift and a reduction in absorption intensity. The blue-shift of the absorption maxima is assigned to a reduction in conjugation length. One explanation for this effect is that planar segments of polymer chains are being twisted, hence breaking up the overlap of π-orbitals between monomer units, disrupting conjugation along the polymer backbone. This seems unlikely since oxidised species tend to favour a planar conformation, and so with the absence of electrochemical degradation, one would expect an increase in planarity after oxidative stress. Another explanation for this effect is that a chemical bond is broken along the polymer backbone during the oxidative stress regime. The C=N bond in PTTz is speculated to be affected during degradation as evidenced by Raman spectroscopy (Figure 4.37). The C=N stretch signal is quenched after

degradation suggesting that the C=N bond is broken in the degradation step. This would effectively break up conjugation along the polymer backbone, resulting in shorter conjugation length, widening the bandgap, which is consistent with the blue-shift observed in the absorption profile. An important implication of this blue-shift is the change in electronic structure induced by electrochemical degradation. One way of quantifying this effect is to consider how much the absorption maxima change in terms of energy when such a blue-shift occurs. Consider:

$$\Delta E_{peak} = E_{shifted\ peak} - E_0$$

where ΔE_{peak} is difference in energy between $E_{shifted\ peak}$ (the energy of the photon responsible for the absorption maximum after the shift) and E_0 (the energy of the photon responsible for the absorption maximum before the shift).

$$\Delta E_{peak}(eV) = \left(\frac{hc}{\lambda_0 + \lambda_{shift}} - \frac{hc}{\lambda_0}\right) x\ \frac{1}{e} = -\frac{\lambda_{shift} hc}{e.\lambda_0.(\lambda_0 + \lambda_{shift})}$$

where λ_0 is the initial absorption maximum wavelength, λ_{shift} is the absorption maximum shift, h is Planck's constant, c is the speed of light and e is the elementary charge. ΔE_{peak} is calculated to be 38 meV, 64 meV and 86 meV for P3HT, PTTTz, and PTTz, respectively. The smallest change is once again seen in P3HT, the intermediary change in PTTTz, and the largest change in PTTz, which is in good agreement with the order of polaron stabilities already discussed. This shift in absorption to shorter wavelengths suggests a widening of the optical bandgap, which could be detrimental to spectral overlap with the sun, and might therefore reduce the material's potential to generate a photocurrent as part of a polymer/fullerene blend.

In summary, we have used chronoamperometry to apply an oxidative stress to polymer neat films, probing the stability of the hole polaron species in polymer neat films. We have managed to control the relative degree of oxidation across a series of polymers with different oxidation potentials, allowing for comparison of hole polaron stability across a series of polymers. Finally, we note that we are beginning to see a trend where deeper HOMO polymers lead to less stable hole polarons (Figure 4.36). This trend will be investigated further in Chapter 5.

5

Polymer neat film stability under electrochemically induced oxidative stress

5.1 Introduction

In this chapter we will build on the work in Chapter 4, applying the same methodology for investigating hole polaron stability in neat films to a wider range of polymers. Specifically, we will investigate the effect of HOMO energy level on the hole polaron stability. In order to control the degree of oxidative stress, each polymer film will first be characterised using CV and CVA.

5.1.1 Materials

The chemical structure of the polymers studied in this chapter are given in Figure 5.38, with the exception of Ra-P3HT, which has the same chemical structure as Rr-P3HT.

PCDTBT and PTB7 were purchased from 1-Material and purified by Bob Schroeder before use. Rr-P3HT, Ra-P3HT, SiIDT-BT, PDPP3Se, PTT, IDFBT and PCDTBT were all synthesised and purified[111,112,113] in the groups of Iain McCulloch and Martin Heeney by Shahid Ashraf, Hugo Bronstein, Mindaugus Kirk, Bob Schroeder, Munazza Shahid, and Weimin Zhang.

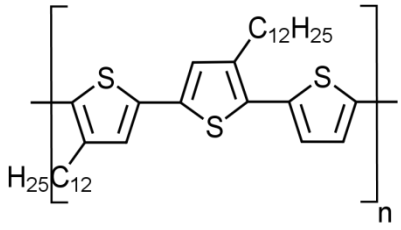

PTT

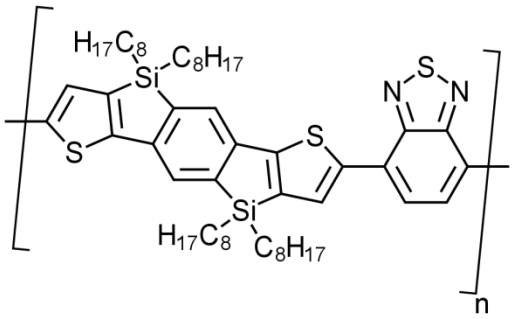

SiIDT-BT

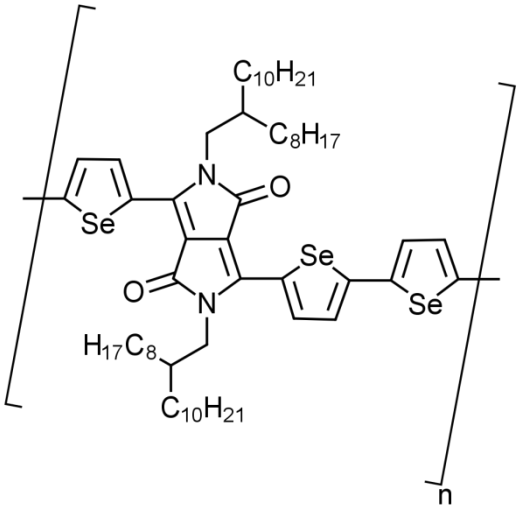

PDPP3Se

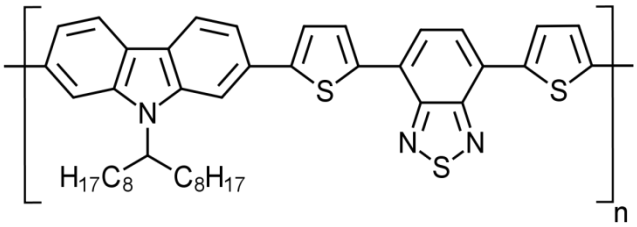

PCDTBT

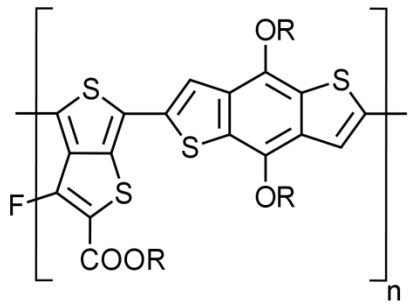

R=$_2$-ethylhexyl

PTB7

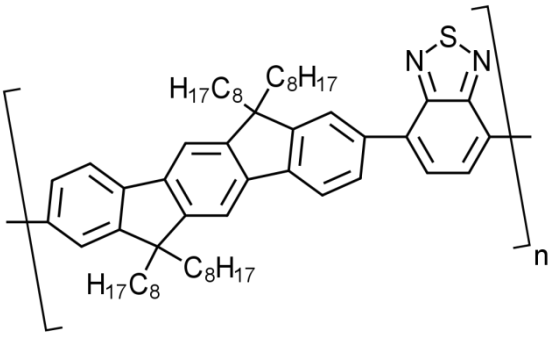

IDFBT

Figure 5.38 – Structures of some of the polymers investigated in this chapter.

5.2 Results

5.2.1 Ra-P3HT

Stirring Ra-P3HT (0.2 mg) in degassed dry chloroform (1 mL) at room temperature resulted in a clear, bright orange solution. Spin-coating the solution onto a clean, dry FTO glass substrate resulted in an orange thin film. The absorption spectrum of the as-spun film is given in Figure 5.39a, and features a broad absorption profile with a maximum at 440 nm and an absorption onset wavelength of 555 nm, corresponding to an optical bandgap of 2.24 eV.

Cyclic voltammetry was carried out using an oxidative sweep between 0.00 V and +0.90 V, in order to obtain an estimate for HOMO energy level, and is given in Figure 5.39b. An oxidation peak is observed at +0.90 V which has an oxidation onset potential of +0.74 V. An estimate of the HOMO energy level is found to be -5.10 eV by consideration of the oxidation onset potential. The absorption spectrum is found to be very stable and remains unchanged after three oxidative sweeps (Figure 5.39a). Absorption intensity at the polymer peak absorption wavelength (440 nm) was measured as a function of applied potential, simultaneous to the cyclic voltammetry experiment, thereby producing the normalised cyclic voltabsorptogram in Figure 5.39c. The onset of oxidation is represented by the onset of the drop in absorption intensity at +0.74 V, which corresponds to a HOMO energy level of -5.10 eV. A potential of +0.83 V caused the absorption intensity at the polymer peak absorption wavelength to decrease by 25%, and was therefore used as an oxidative stress potential during the degradation experiment.

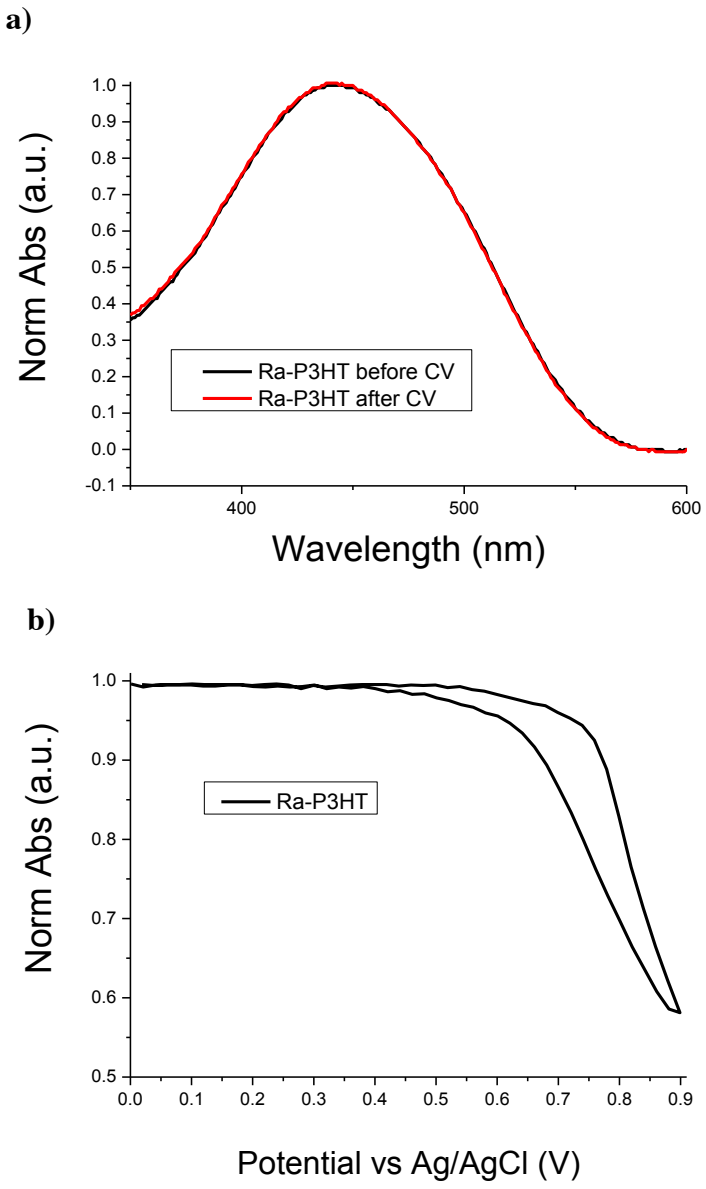

Figure 5.39 – Optical and electrochemical characterisation of an as-spun neat film of regio-random P3HT; a) normalised absorption spectrum before (black) and after (red) three CV cycles, b) cyclic voltabsorptogram performed with a scan rate of 20 mV s^{-1}, measuring normalised absorbance at 440 nm as a function of applied potential. Note: The electronic file containing the cyclic voltammogram was lost, between measurement and the writing of this thesis. The voltammogram was analysed at the time of measurement, and is thus reported and discussed in the main text of this chapter.

Table 5.12 – Electrochemical degradation of thin films of regiorandom P3HT, at varying oxidative stress potentials as displayed in Figure 5.40. The wavelength and normalised absorption intensity of the shifting main absorption peak is tabulated, as well as the normalised absorption intensity at the initial absorption peak wavelength. The overall change in each parameter is also included. * The data file for the absorption spectrum after 10000 s of degradation for the film degraded at +0.88 V was lost, therefore the overall change is calculated for 6,000 s of degradation time.

Oxidative stress potential / V	***+0.78***			***+0.83***			***+0.88***		
Total degradation time / seconds	λ_{max} **/ nm**	$Norm\ Abs_{max}$ **/ a.u.**	$Norm\ Abs_{443\ nm}$ **/ a.u.**	λ_{max} **/ nm**	$Norm\ Abs_{max}$ **/ a.u.**	$Norm\ Abs_{442\ nm}$ **/ a.u.**	λ_{max} **/ nm**	$Norm\ Abs_{max}$ **/ a.u.**	$Norm\ Abs_{444\ nm}$ **/ a.u.**
0	443	1.00	1.00	442	1.00	1.00	444	1.00	1.00
30	443	1.01	1.01	442	1.01	1.01	442	1.01	1.01
60	446	1.02	1.01	442	1.01	1.01	442	1.01	1.01
120	444	1.02	1.01	443	1.01	1.01	442	1.01	1.01
300	443	1.01	1.01	440	1.01	1.01	439	1.01	1.01
600	443	1.01	1.01	441	1.01	1.01	440	1.00	0.99
1000	443	1.01	1.01	439	1.04	1.03	438	0.99	0.99
1500	442	1.01	1.01	440	1.02	1.01	436	0.99	0.98
3000	439	1.00	0.99	437	1.00	1.00	432	0.98	0.96
6000	439	0.99	0.98	435	0.99	0.98	431	0.97	0.93
10000	435	0.97	0.97	432	0.99	0.97	-	-	-
Total change	-8	-0.03	-0.03	-10	-0.01	-0.03	-13*	-0.03*	-0.07*

In addition to the oxidative stress potential determined by the 25% reduction in absorption intensity in the CVA (+0.83 V), two other potentials were investigated; +0.78 V (12% oxidation) and +0.88 V (38% oxidation). Normalised absorption spectra as a function of total oxidative stress time are given in Figure 5.40. The absorption profile generally blue-shifts and reduces in intensity at both the initial absorption maximum wavelength and the shifting absorption maximum wavelength. Data from Figure 5.40 are tabulated in Table 5.12. As expected, the smallest oxidative stress potential (+0.78 V) produced the smallest response in the absorption spectrum after being subjected to nearly 3 hours of oxidative stress, whereas the largest potential (+0.88 V) produced the largest response in the absorption spectrum even though it was only degraded for just over 1.5 hours. An oxidative stress potential of +0.83 V caused a blue-shift of 10 nm, and an insignificant reduction in absorption intensity after nearly 3 hours of oxidative stress.

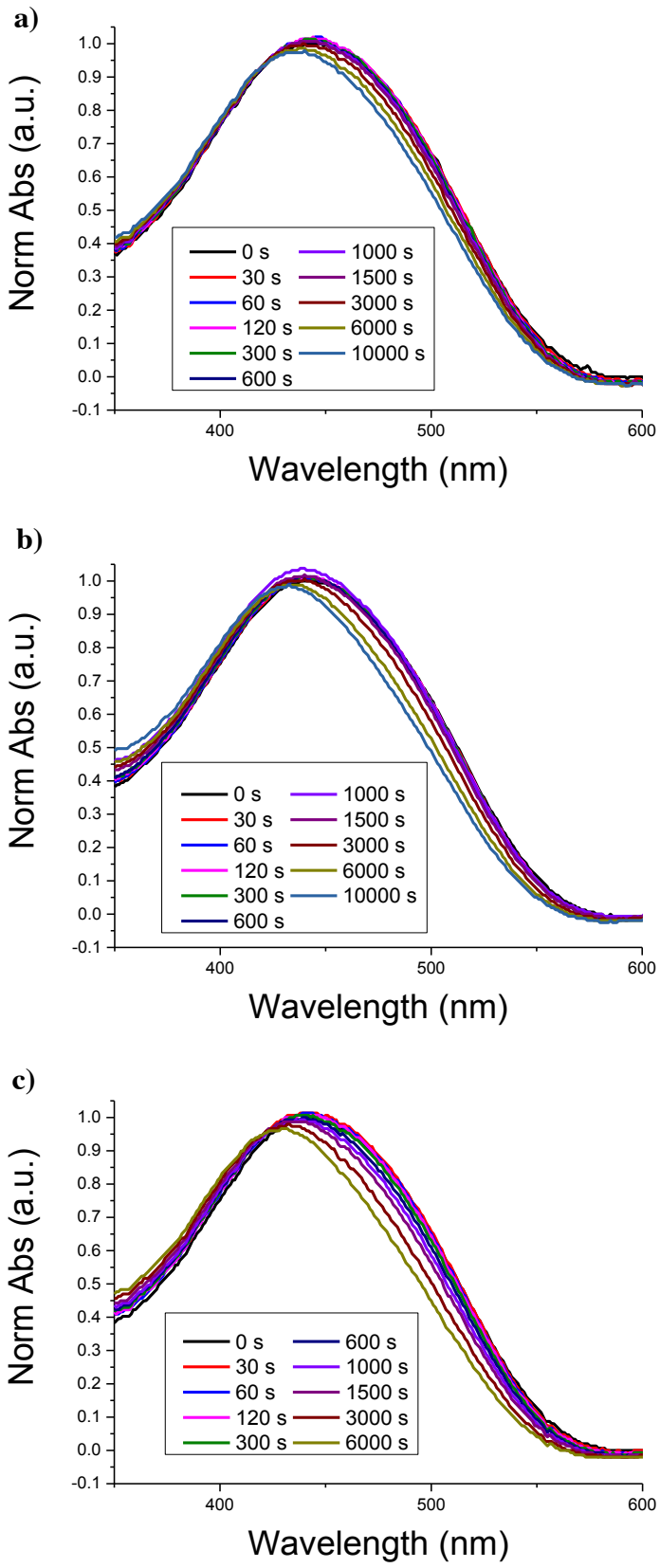

Figure 5.40 – Stability of as-spun neat films of regio-random P3HT demonstrated by evolution of absorption spectra as a function of degradation time. Each film was degraded at a different degrading potential; a) +0.78 V, b) +0.83 V, and c) +0.88 V.

5.2.2 SiIDT-BT

Stirring SiIDT-BT (0.2 mg) in degassed dry chloroform (1 mL) at room temperature resulted in a dark blue solution. Spin-coating the solution onto a clean, dry FTO glass substrate resulted in a dark blue thin film. The absorption spectrum of the as-spun film is given in Figure 5.41a, and features an absorption profile with a maximum at 635 nm, a shoulder at *ca* 600 nm, and an absorption onset wavelength of 690 nm, corresponding to an optical bandgap of 1.8 eV.

Cyclic voltammetry was carried using an oxidative sweep between 0.00 V and +1.10 V, in order to obtain an estimate for HOMO energy level, and is given in Figure 5.41b. An oxidation peak is observed at +1.08 V, which has an oxidation onset potential of +1.02 V. An estimate of the HOMO energy level is found to be -5.38 eV by consideration of the oxidation onset potential. Absorption intensity at the polymer peak absorption wavelength (635 nm) was measured as a function of applied potential, simultaneous to the cyclic voltammetry experiment, thereby producing the normalised cyclic voltabsorptogram in Figure 5.41c. The onset of oxidation is represented by the onset of the drop in absorption intensity at +0.99 V, which corresponds to a HOMO energy level of -5.35 eV. A potential of +1.02 V caused the absorption intensity at the polymer peak absorption wavelength to decrease by 25%, and was therefore used as the oxidative stress potential during the degradation experiment.

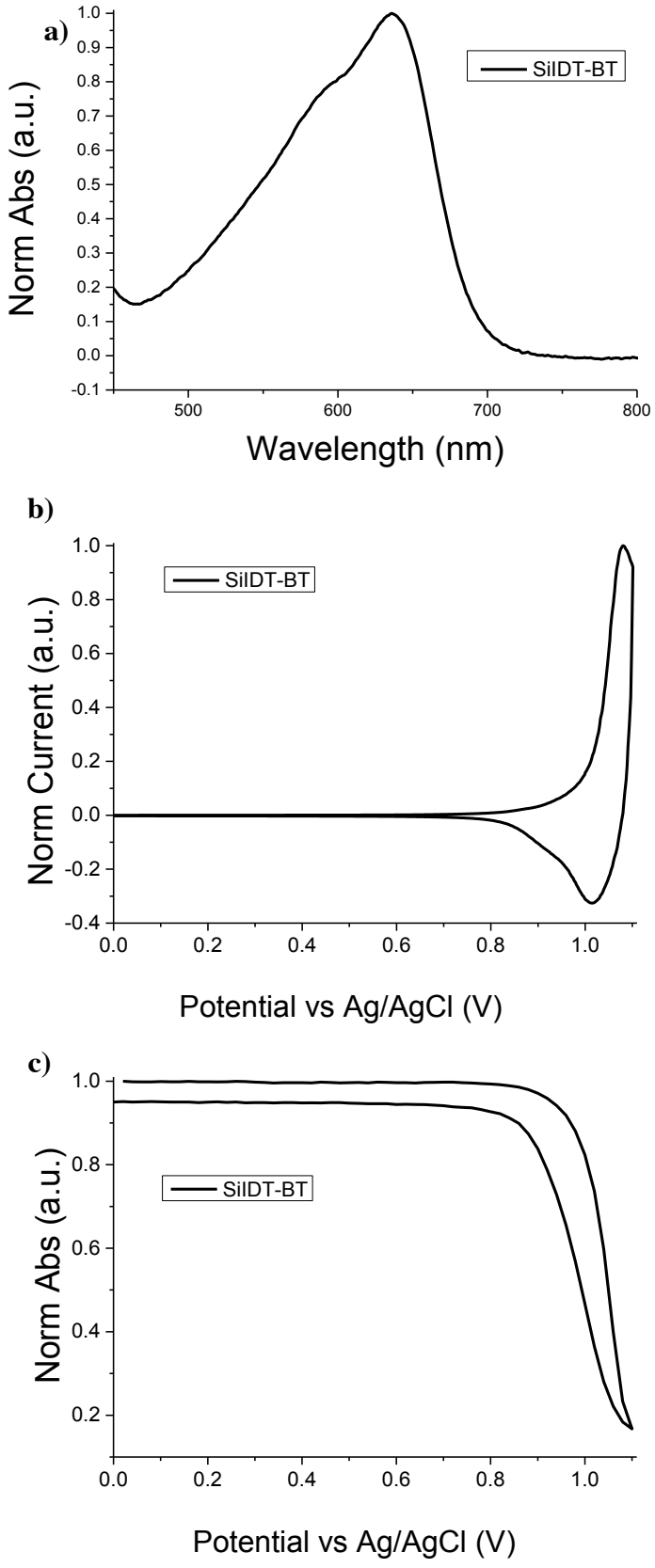

Figure 5.41 – Optical and electrochemical characterisation of an as-spun neat film of SiIDT-BT; a) normalised absorption spectrum, b) cyclic voltammogram performed with a scan rate of 20 mVs^{-1}, and c) cyclic voltabsorptogram, giving normalised absorbance at 637 nm as a function of applied potential.

Table 5.13 – Electrochemical degradation of a thin film of SiIDT-BT, at +1.00 V as displayed in Figure 5.42. The wavelength and normalised absorption intensity of the shifting main absorption peak is tabulated, as well as the normalised absorption intensity at the initial absorption peak wavelength. The overall change in each parameter is also included.

Total degradation time / seconds	λ_{max} **/ nm**	$Norm\ Abs_{max}$ **/ a.u.**	$Norm\ Abs_{443\ nm}$ **/ a.u.**
0	636	1.00	1.00
30	636	0.93	0.93
60	636	0.93	0.93
120	633	0.87	0.87
300	630	0.81	0.80
600	628	0.77	0.76
1000	624	0.74	0.72
1500	616	0.71	0.67
3000	593	0.66	0.58
6000	584	0.62	0.46
10000	560	0.58	0.33
Total change	-76	-0.42	-0.67

Electrochemical degradation of SiIDT-BT was investigated with a probing potential of +1.00 V. Normalised absorption spectra as a function of total oxidative stress time are given in Figure 5.42, and recorded in Table 5.13. After a total oxidative stress time of

10,000 s, the absorption spectrum exhibits a strong blue-shift of 76 nm and a greatly reduced intensity at both the initial absorption maximum wavelength (-67%) and the shifting absorption maximum wavelength (-42%).

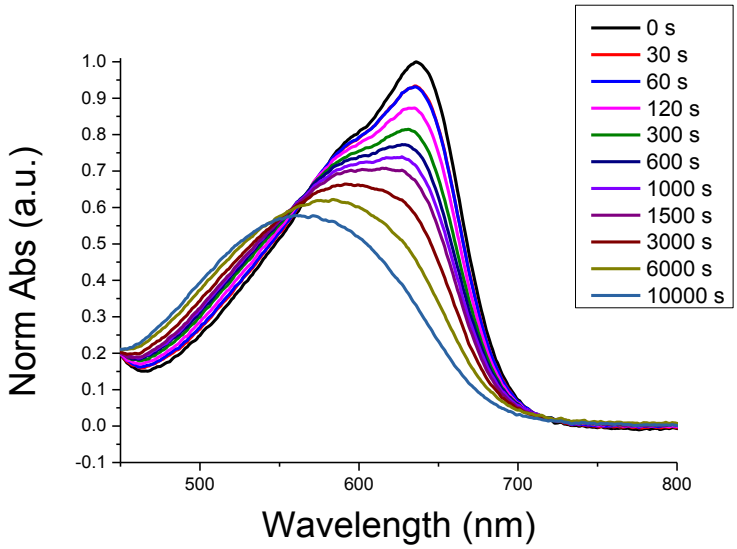

Figure 5.42 – Stability of as-spun neat film of SiIDT-BT demonstrated by evolution of absorption spectra as a function of degradation time. Film was degraded using a degrading potential of +1.00 V.

5.2.3 PDPP3Se

Spin-coating PDPP3Se from solution (0.2 mg in 1 mL dry chloroform) resulted in the absorption spectrum shown in Figure 5.43a, which features a very broad absorption profile with a maximum at 835 nm and an absorption onset wavelength of *ca* 1040 nm, corresponding to an optical bandgap of 1.19 eV.

Cyclic voltammetry was carried out using an oxidative sweep between 0.00 V and +1.20 V, in order to obtain an estimate for HOMO energy level, and is given in Figure 5.43b. An oxidation peak is observed at +0.88 V which has an oxidation onset potential of +0.67 V. An estimate of the HOMO energy level is found to be -5.03 eV by consideration of the oxidation onset potential. The absorption spectrum is found to be unstable to the cyclic voltammetry experiment; the absorption intensity at the peak wavelength reduces by 5% after three oxidative sweeps (Figure 5.43a). Absorption intensity at the polymer peak absorption wavelength (835 nm) was measured as a function of applied potential, simultaneous to the cyclic voltammetry experiment, thereby producing the normalised cyclic voltabsorptogram in Figure 5.43c. The onset of oxidation is represented by the onset of the drop in absorption intensity at +0.72 V, which corresponds to a HOMO energy level of -5.08 eV. A potential of +0.78 V caused the absorption intensity at the polymer peak absorption wavelength to decrease by 25%, and was therefore used during the degradation experiment.

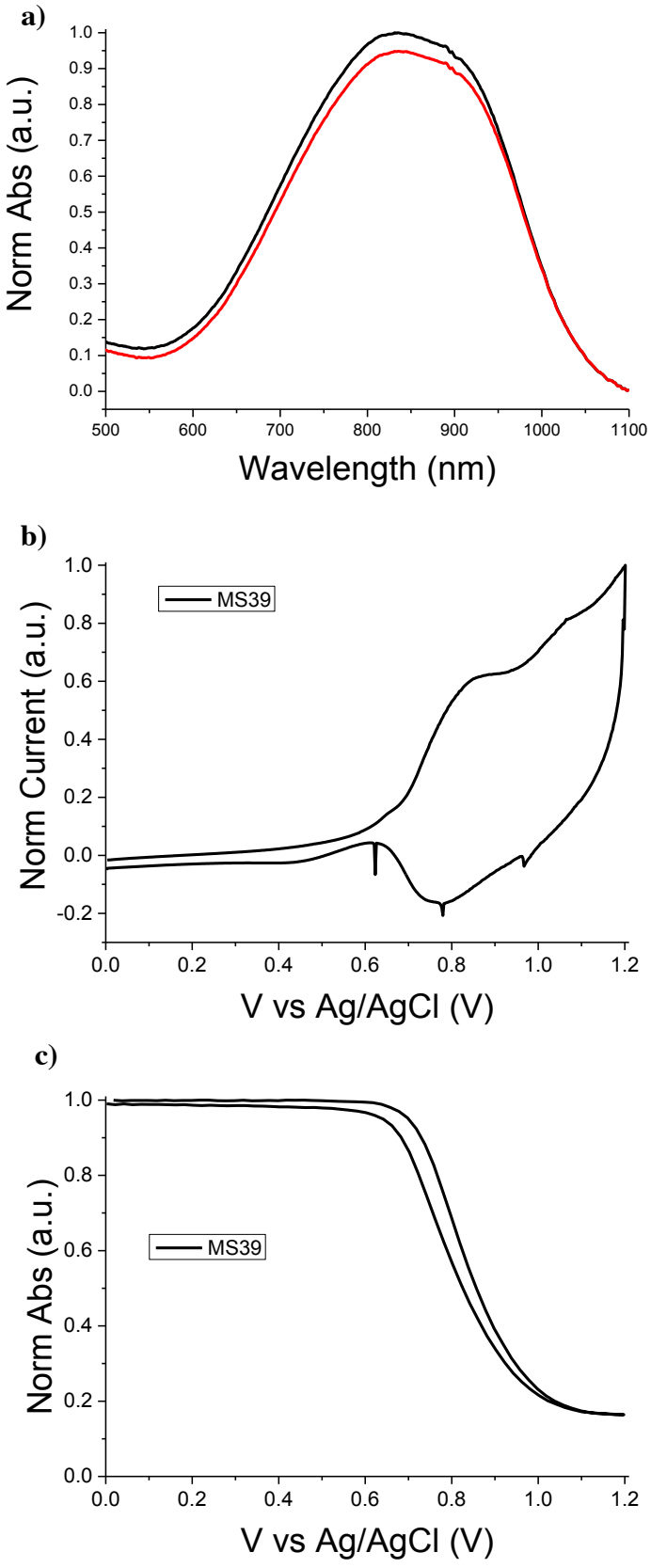

Figure 5.43 – Optical and electrochemical characterisation of an as-spun neat film of PDPP3Se; a) normalised absorption spectrum before (black) and after (red) three CV cycles, b) cyclic voltammogram performed with a scan rate of 20 mVs^{-1}, and c) cyclic voltabsorptogram, measuring normalised absorbance at 835 nm as a function of applied potential.

Table 5.14 – Electrochemical degradation of a thin film of PDPP3Se, at +0.78 V as displayed in Figure 5.44. The wavelength and normalised absorption intensity of the shifting main absorption peak is tabulated, as well as the normalised absorption intensity at the initial absorption peak wavelength. The overall change in each parameter is also included.

Total degradation time / seconds	**λ_{max} / nm**	***Norm Abs*$_{max}$ / a.u.**	***Norm Abs*$_{835\ nm}$ / a.u.**
0	835	1.00	1.00
30	835	1.00	1.00
60	835	0.99	0.99
120	835	0.99	0.99
300	832	0.99	0.99
600	831	0.98	0.98
1000	830	0.97	0.97
1500	831	0.96	0.95
3000	825	0.92	0.92
6000	817	0.87	0.86
10000	810	0.82	0.81
Total change	-25	-0.18	-0.19

Electrochemical degradation of PDPP3Se was investigated with an oxidative stress potential of +0.78 V. Normalised absorption spectra as a function of total oxidative stress time are given in Figure 5.44, and recorded in Table 5.14. After a total oxidative

stress time of 10,000 s, the main absorption peak is blue-shifted by 25 nm and is reduced in intensity by 18%. The absorption intensity at the initial peak absorption wavelength (835 nm) is reduced by 19%.

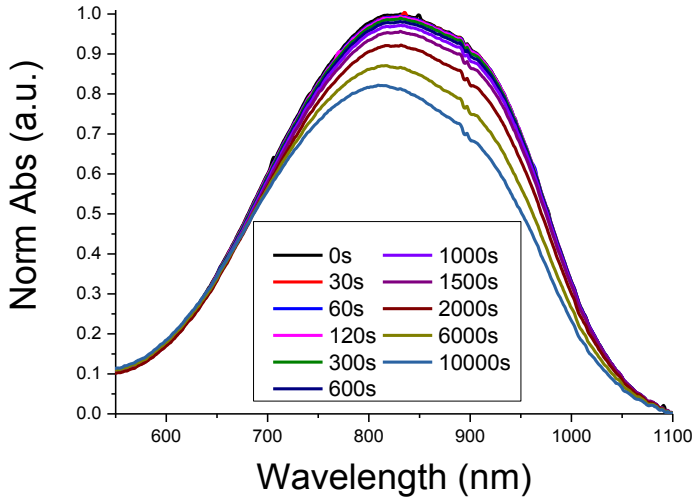

Figure 5.44 – Stability of as-spun neat film of PDPP3Se demonstrated by evolution of absorption spectra as a function of degradation time. Film was degraded using a degrading potential of +0.78 V.

5.2.4 PTB7

Spin-coating PTB7 from solution (0.2 mg in 1 mL dry chloroform) resulted in the absorption spectrum in Figure 5.45a, which features a broad absorption profile with a maximum at 670 nm, an absorption shoulder at 625 nm and an absorption onset wavelength of 745 nm, corresponding to an optical bandgap of 1.67 eV.

Cyclic voltammetry was carried using an oxidative sweep between 0.00 V and +1.20 V, in order to obtain an estimate for HOMO energy level, and is given in Figure 5.45b. An oxidation peak is observed at +1.13 V, which has an oxidation onset potential of +0.79 V. An estimate of the HOMO energy level is found to be -5.15 eV by consideration of the oxidation onset potential. The spectroelectrochemical response of PTB7 was recorded by measuring the absorption spectrum of the film as a function of applied potential and is shown in Figure 5.45c. Two trends are observed as the applied potential is increased; (i) a very broad absorption appears at *ca* 950 nm, (ii) the absorption intensity of the main peak decreases and becomes less structured. The normalised absorption intensity at 670 nm is plotted as a function of applied potential in Figure 5.45d. The onset of oxidation is represented by the onset of the drop in absorption intensity at 670 nm (+0.72 V), which corresponds to a HOMO energy level of -5.08 eV. A potential of +1.00 V caused the absorption intensity at the polymer peak absorption wavelength to decrease by 28% (considered to be close to the 25% target) and was therefore used as the oxidative stress potential during the degradation experiment.

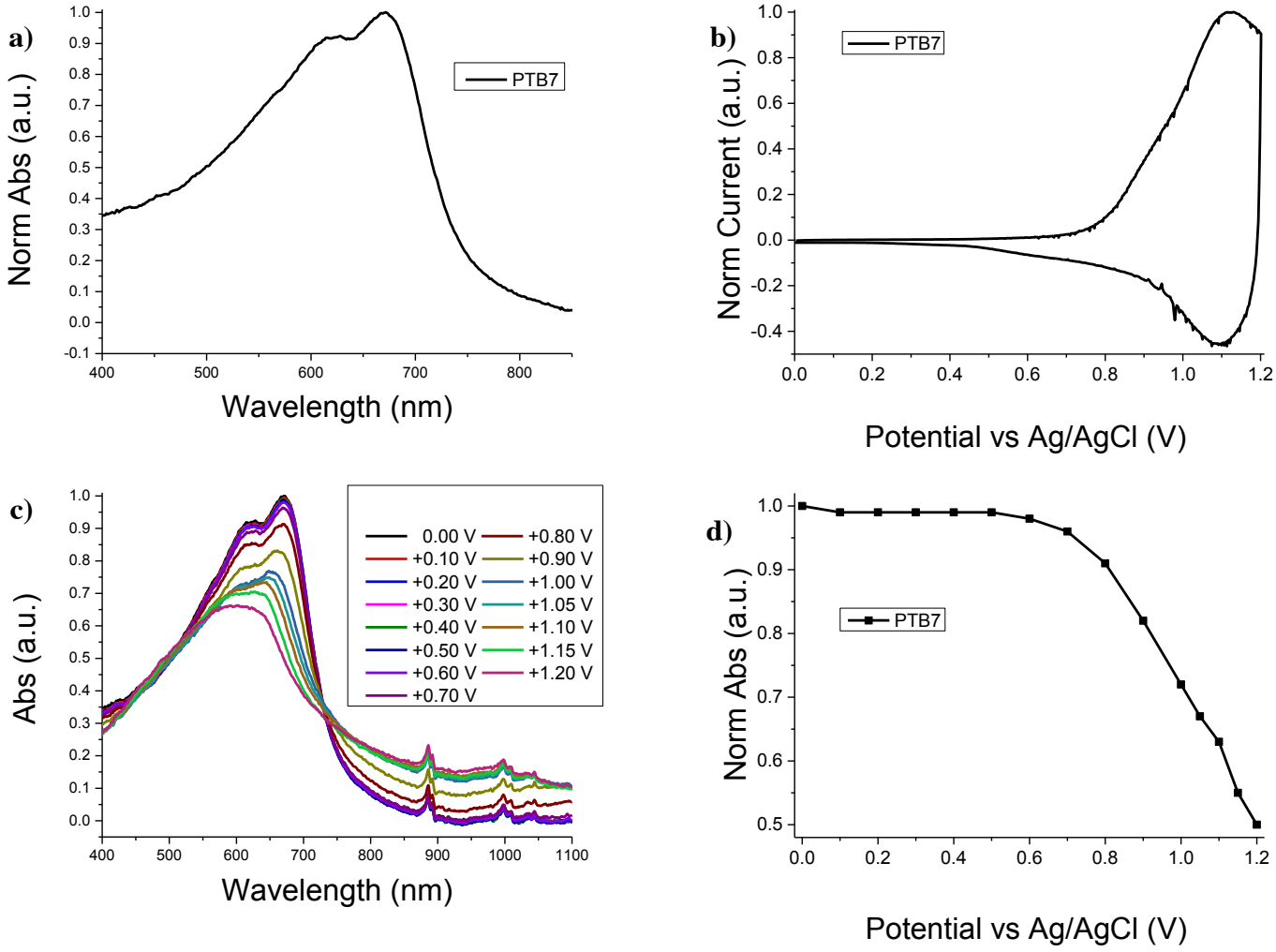

Figure 5.45 – Optical and electrochemical characterisation of an as-spun neat film of PTB7; a) normalised absorption spectrum, b) Cyclic voltammogram performed with a scan rate of 20 mVs^{-1}, c) spectroelectrochemical response at increasingly positive potentials, d) spectroelectrochemical response at 670 nm, at increasingly positive potentials.

Table 5.15 – Electrochemical degradation of a thin film of PTB7, at +1.00 V as displayed in Figure 5.46. The wavelength and normalised absorption intensity of the shifting main absorption peak is tabulated, as well as the normalised absorption intensity at the initial absorption peak wavelength. The overall change in each parameter is also included.

Total degradation time / seconds	**λ_{max} / nm**	***Norm Abs*$_{max}$ / a.u.**	***Norm Abs*$_{678\ nm}$ / a.u.**
0	678	1.00	1.00
30	676	1.01	1.00
60	673	1.01	0.99
120	671	0.99	0.97
300	667	0.98	0.93
600	664	0.97	0.89
1000	663	0.96	0.87
1500	662	0.94	0.84
3000	660	0.93	0.81
6000	658	0.91	0.78
10000	657	0.90	0.75
Total change	-21	-0.10	-0.25

Electrochemical degradation of PTB7 was investigated with an oxidative stress potential of +1.00 V. Normalised absorption spectra as a function of total oxidative stress time are given in Figure 5.46, and tabulated in Table 5.15. After a total oxidative

stress time of 10,000 s, the main absorption peak is blue-shifted by 21 nm and is reduced in intensity by 10%. The absorption intensity at the initial peak absorption wavelength (678 nm) is reduced by 25%.

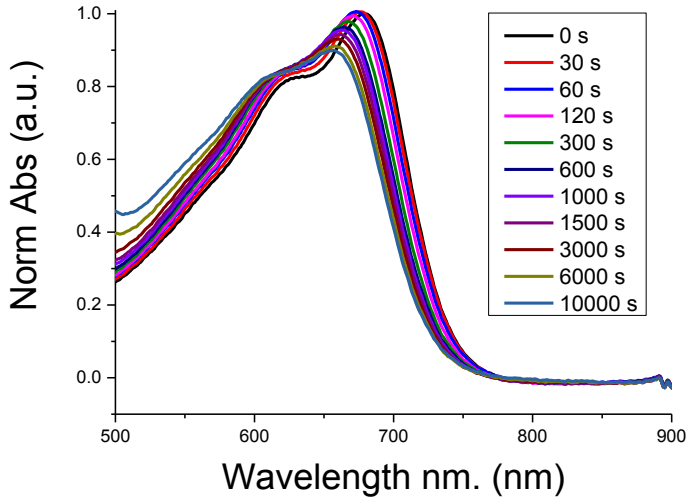

Figure 5.46 – Stability of as-spun neat film of PTB7 demonstrated by evolution of absorption spectra as a function of degradation time. Film was degraded using a degrading potential of +1.00 V.

5.2.5 PTT

Spin-coating PTT from solution (0.2 mg in 1 mL dry chloroform) resulted in the absorption spectrum given in Figure 5.47a, which features an absorption maximum at 545 nm, accompanied by an absorption shoulder at *ca* 585 nm and an absorption onset wavelength of 635 nm, corresponding to an optical bandgap of 1.95 eV.

Cyclic voltammetry was carried out using an oxidative sweep between 0.00 V and +1.00 V, in order to obtain an estimate for HOMO energy level, and is given in Figure 5.47b. An oxidation peak is observed at +0.72 V, which has an oxidation onset potential of +0.67 V. An estimate of the HOMO energy level is found to be -5.03 eV by consideration of the oxidation onset potential. The absorption spectrum is found to be fairly stable to the cyclic voltammetry experiment; the absorption intensity at the peak wavelength reduces by 3% after three oxidative sweeps (Figure 5.47a). Absorption intensity at the polymer peak absorption wavelength (545 nm) was measured as a function of applied potential, simultaneous to the cyclic voltammetry experiment, thereby producing the normalised cyclic voltabsorptogram in Figure 5.47c. The onset of oxidation is represented by the onset of the drop in absorption intensity at +0.66 V, which corresponds to a HOMO energy level of -5.02 eV. A potential of +0.68 V caused the absorption intensity at the polymer peak absorption wavelength to decrease by 25%, and was therefore used as the oxidative stress potential during the degradation experiment.

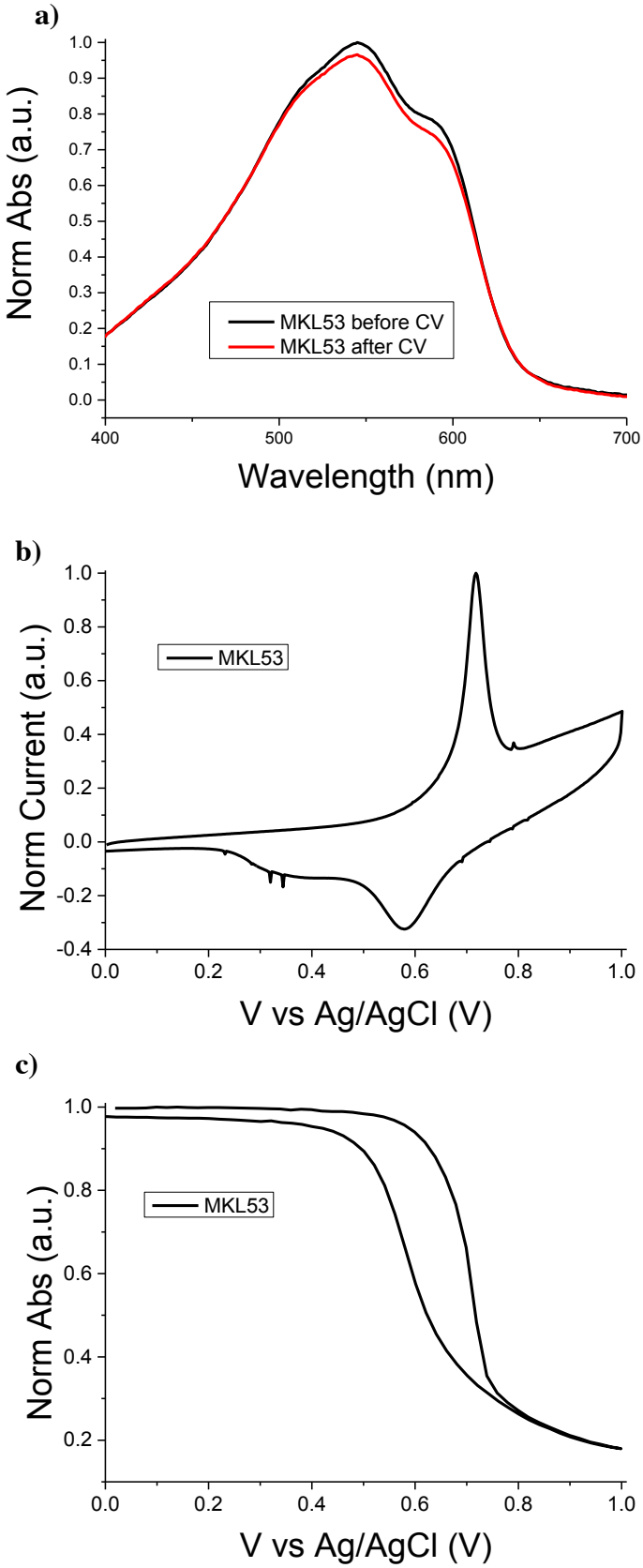

Figure 5.47 – Optical and electrochemical characterisation of an as-spun neat film of PTT; a) normalised absorption spectrum before and after three CV cycles, b) cyclic voltammogram performed with a scan rate of 20 mVs^{-1}, and c) cyclic voltabsorptogram, measuring normalised absorbance at 545 nm as a function of applied potential.

Table 5.16 – Electrochemical degradation of a thin film of PTT, at +0.68 V as displayed in Figure 5.48. The wavelength and normalised absorption intensity of the shifting main absorption peak is tabulated, as well as the normalised absorption intensity at the initial absorption peak wavelength. The overall change in each parameter is also included.

Total degradation time / seconds	λ_{max} **/ nm**	$Norm\ Abs_{max}$ **/ a.u.**	$Norm\ Abs_{545\ nm}$ **/ a.u.**
0	545	1.00	1.00
30	545	1.00	1.00
60	545	1.01	1.01
120	545	1.01	1.01
300	545	1.01	1.01
600	545	1.01	1.01
1000	544	1.00	0.99
1500	544	0.99	0.99
3000	543	0.98	0.97
6000	541	0.95	0.94
10000	536	0.91	0.89
Total change	-9	-0.09	-0.11

Electrochemical degradation of PTT was investigated with an oxidative stress potential of +0.68 V. Normalised absorption spectra as a function of total oxidative stress time are given in Figure 5.48, and recorded in Table 5.16. After a total oxidative stress time

of 10,000 s, the main absorption peak is blue-shifted by 9 nm and is reduced in intensity by 9%. The absorption intensity at the initial peak absorption wavelength (545 nm) is falls by 11%.

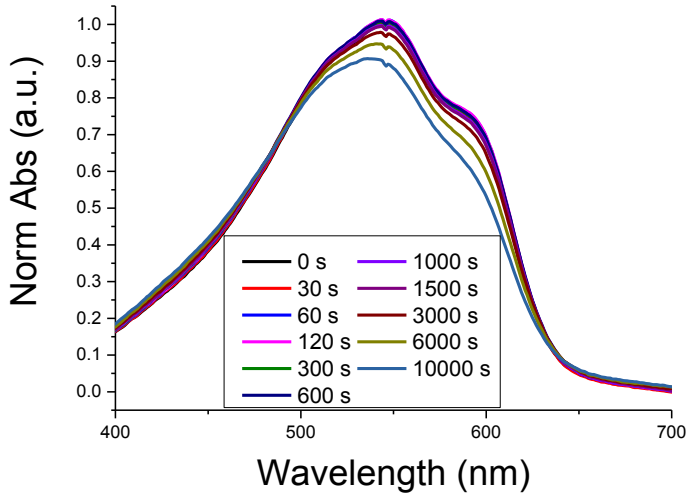

Figure 5.48 - Stability of as-spun neat film of PTT demonstrated by evolution of absorption spectra as a function of degradation time. Film was degraded using an oxidative stress potential of +0.68 V.

5.2.6 IDFBT

Spin-coating IDFBT from solution (0.2 mg in 1 mL dry chloroform) resulted in the absorption spectrum given in Figure 5.49a, which features a broad absorption at 470 nm, with an absorption onset wavelength of 520 nm, corresponding to an optical bandgap of 2.39 eV.

Cyclic voltammetry was carried out using an oxidative sweep between 0.00 V and +1.50 V, in order to obtain an estimate for HOMO energy level, and is given in Figure 5.49b. Two oxidation peaks are observed at +1.23 V and +1.43 V, which have oxidation onset potentials of +1.07 V and +1.40 V, respectively. Hence, by considering these two oxidation onset potentials, two estimates for the HOMO energy level are found to be -5.43 eV and -5.76 eV, respectively. Absorption intensity at the polymer peak absorption wavelength (470 nm) was measured as a function of applied potential, simultaneous to the cyclic voltammetry experiment, thereby producing the normalised cyclic voltabsorptogram in Figure 5.49c. The onset of oxidation is represented by the onset of the drop in absorption intensity at +1.38 V, which corresponds to a HOMO energy level of -5.74 eV. A potential of +1.40 V caused the absorption intensity at the polymer peak absorption wavelength to decrease by 25%, and was therefore used as an oxidative stress potential in the degradation experiment. In addition two potential values that were 0.05 V greater (75% oxidation) and lesser (7% oxidation) than 1.40 V were also used to degrade separate films.

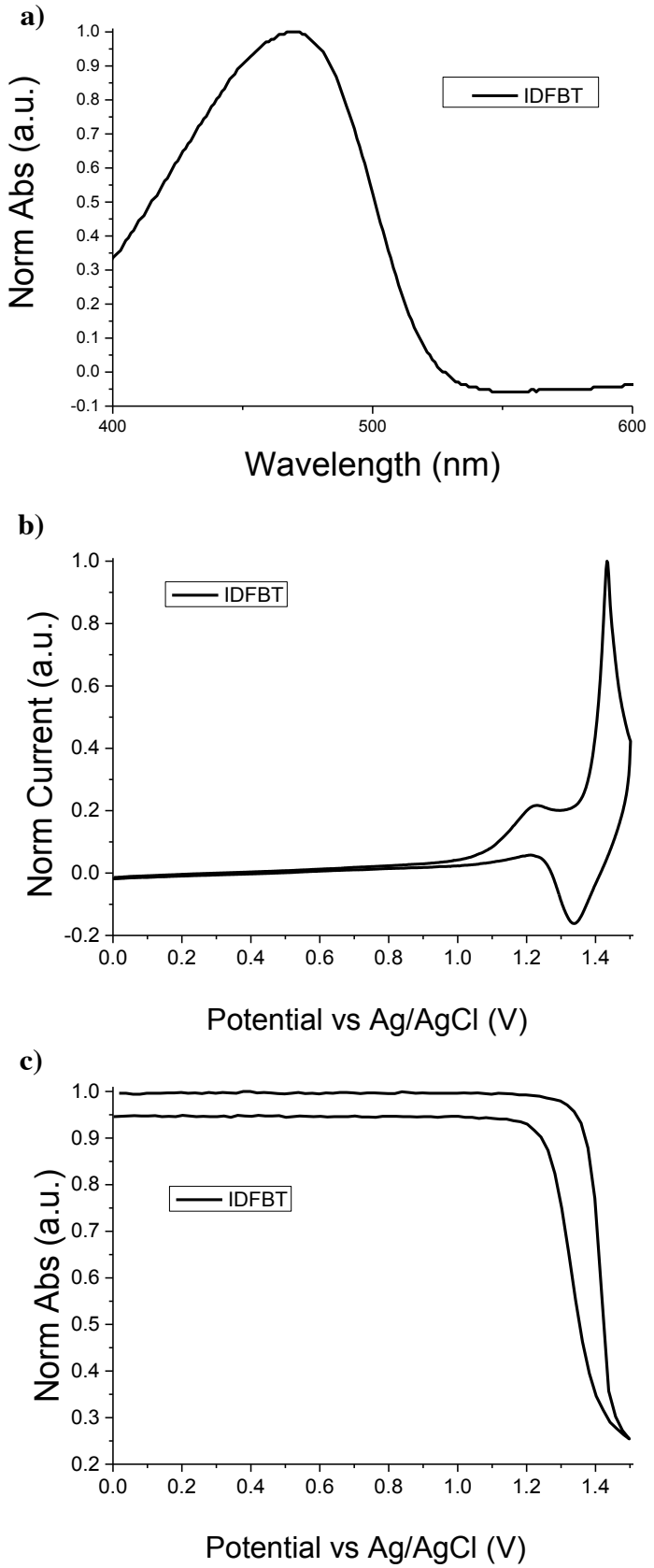

Figure 5.49 – Optical and electrochemical characterisation of an as-spun neat film of IDFBT; a) normalised absorption spectrum, b) cyclic voltammogram performed with a scan rate of 20 mVs^{-1}, and c) cyclic voltabsorptogram, measuring normalised absorbance at 470 nm as a function of applied potential.

Table 5.17 – Electrochemical degradation of thin films of IDFBT, at varying oxidative stress potentials as displayed in Figure 5.40. The wavelength and normalised absorption intensity of the shifting main absorption peak is tabulated, as well as the normalised absorption intensity at the initial absorption peak wavelength. The overall change in each parameter is also included.

Oxidative stress potential / V	***+1.35***			***+1.40***			***+1.45***		
Total degradation time / seconds	λ_{max} **/ nm**	$Norm\ Abs_{max}$ **/ a.u.**	$Norm\ Abs_{470\,nm}$ **/ a.u.**	λ_{max} **/ nm**	$Norm\ Abs_{max}$ **/ a.u.**	$Norm\ Abs_{470\,nm}$ **/ a.u.**	λ_{max} **/ nm**	$Norm\ Abs_{max}$ **/ a.u.**	$Norm\ Abs_{470\,nm}$ **/ a.u.**
0	469	1.00	1.00	469	1.00	1.00	469	1.00	1.00
30	469	0.99	0.99	468	0.96	0.96	467	1.01	1.01
60	469	0.97	0.97	468	0.93	0.93	466	1.01	1.00
120	469	0.97	0.97	467	0.90	0.90	466	0.98	0.98
300	469	0.95	0.95	466	0.88	0.88	463	0.94	0.93
600	468	0.94	0.94	464	0.85	0.85	459	0.88	0.86
1000	468	0.92	0.92	463	0.82	0.81	456	0.83	0.79
1500	467	0.91	0.91	462	0.79	0.78	451	0.79	0.72
3000	466	0.89	0.89	459	0.70	0.69	441	0.68	0.56
6000	465	0.85	0.85	448	0.59	0.53	429	0.55	0.37
10000	462	0.78	0.77	430	0.46	0.34	421	0.47	0.25
Total change	-7	-0.22	-0.23	-39	-0.54	-0.66	-48	-0.53	-0.75

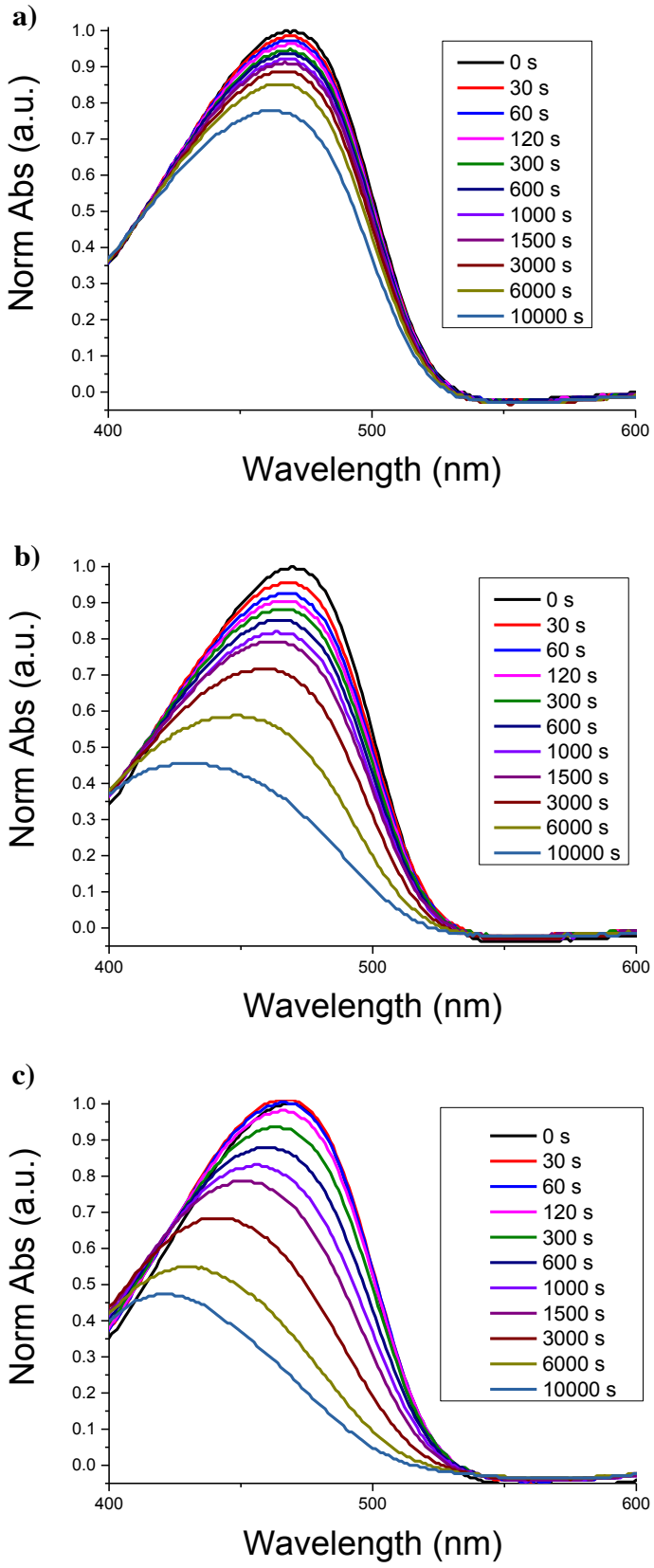

Figure 5.50 – Stability of as-spun neat films of IDFBT demonstrated by evolution of absorption spectra as a function of degradation time. Each film was degraded at a different oxidative stress potential; a) +1.35 V, b) +1.40 V, and c) +1.45 V.

Normalised absorption spectra as a function of total oxidative stress time are given in Figure 5.50. The absorption profile generally blue-shifts and reduces in intensity at both the initial absorption maximum wavelength and the shifting absorption maximum wavelength. Data from Figure 5.50 is tabulated in Table 5.17. As expected, the smallest oxidative stress potential (+1.35 V) produced a significant response in the absorption spectrum after being subjected to nearly 3 hours of oxidative stress, whereas the largest oxidative stress potential (+1.45 V) produced an even stronger response in the absorption spectrum over the same period of time. An oxidative stress potential of +1.40 V caused a blue-shift of 39 nm, and an insignificant reduction in absorption intensity after nearly 3 hours of oxidative stress.

5.2.7 PCDTBT

Spin-coating PCDTBT from solution (0.2 mg in 1 mL dry chloroform) resulted in the absorption spectrum in Figure 5.51a, which features a broad absorption at 575 nm, with an absorption onset wavelength of 660 nm, corresponding to an optical bandgap of 1.88 eV.

Cyclic voltammetry was carried out using an oxidative sweep between 0.00 V and +2.00 V, in order to obtain an estimate for HOMO energy level, and is given in Figure 5.51b. An oxidation peak is observed at +1.05 V, which has oxidation onset potential at +1.02 V. An estimate of the HOMO energy level is found to be -5.38 eV by consideration of the oxidation onset potential. Absorption intensity at the polymer peak absorption wavelength (575 nm) was measured as a function of applied potential, simultaneous to the cyclic voltammetry experiment, thereby producing the normalised cyclic voltabsorptogram in Figure 5.51c. The onset of oxidation is represented by the onset of the drop in absorption intensity at +1.06 V, which corresponds to a HOMO energy level of -5.42 eV. A potential of +1.00 V caused the absorption intensity at the polymer peak absorption wavelength to decrease by 25%, and was therefore used as the oxidative stress potential in the degradation experiment.

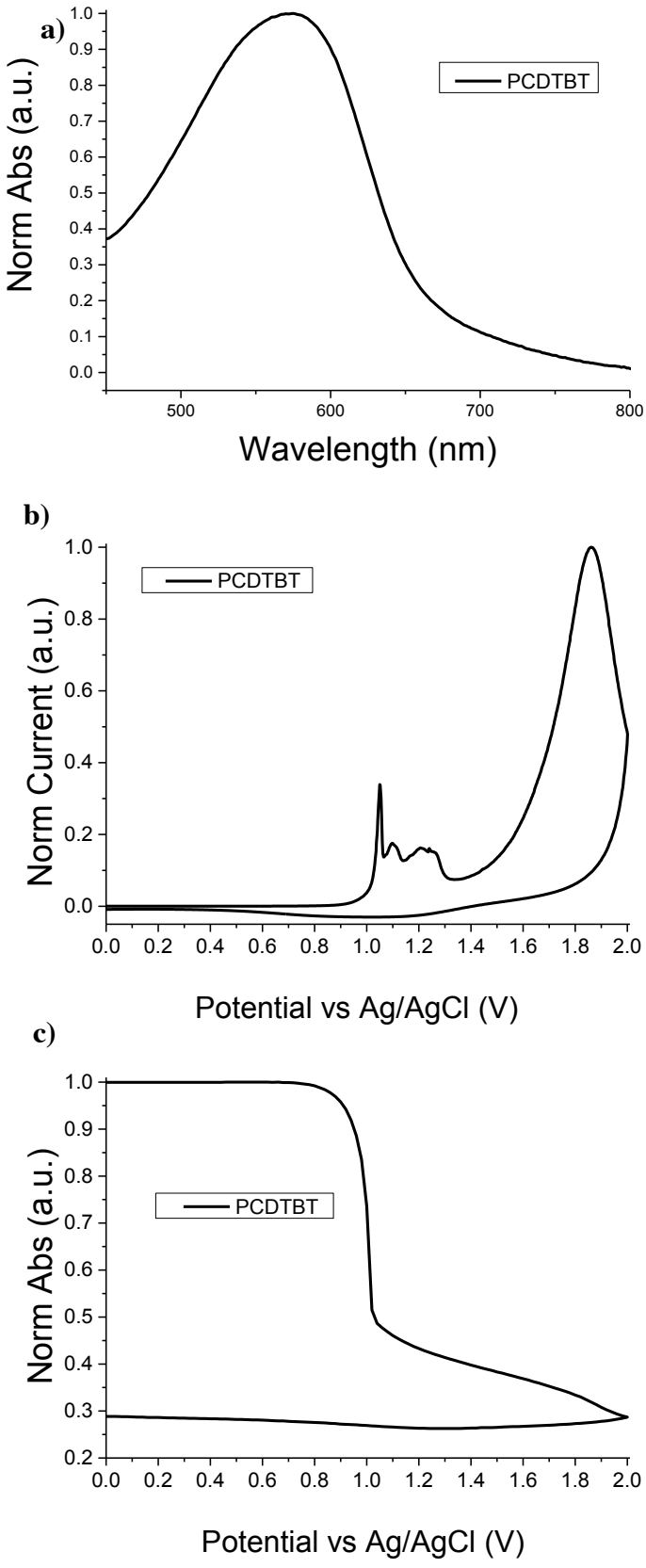

Figure 5.51 – Optical and electrochemical characterisation of an as-spun neat film of PCDTBT; a) normalised absorption spectrum, b) cyclic voltammogram performed with a scan rate of 20 mVs^{-1}, and c) cyclic voltabsorptogram, measuring normalised absorbance at 573 nm as a function of applied potential.

Table 5.18 – Electrochemical degradation of a thin film of PCDTBT, at +1.00 V as displayed in Figure 5.52. The wavelength and normalised absorption intensity of the shifting main absorption peak is tabulated, as well as the normalised absorption intensity at the initial absorption peak wavelength. The overall change in each parameter is also included.

Total degradation time / seconds	λ_{max} **/ nm**	$Norm\ Abs_{max}$ **/ a.u.**	$Norm\ Abs_{573\ nm}$ **/ a.u.**
0	573	1.00	1.00
30	573	0.98	0.98
60	572	0.97	0.97
120	571	0.96	0.96
300	563	0.93	0.92
600	557	0.88	0.86
1000	545	0.83	0.78
1500	535	0.80	0.72
3000	525	0.79	0.63
6000	519	0.79	0.60
10000	519	0.79	0.58
Total change	-54	-0.21	-0.42

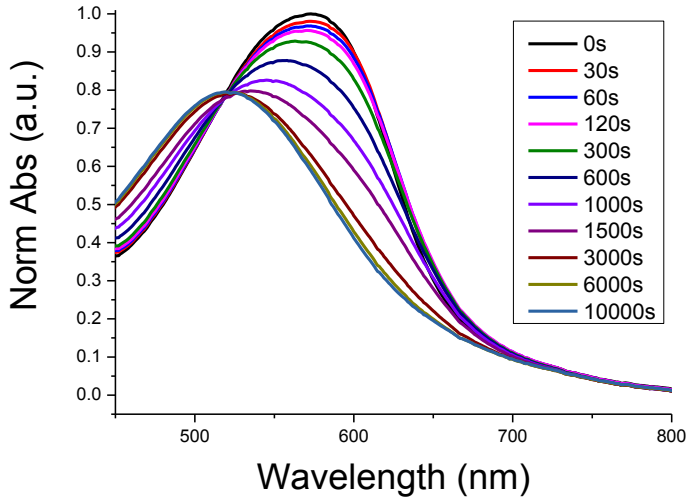

Figure 5.52 – Stability of as-spun neat film of PCDTBT demonstrated by evolution of absorption spectra as a function of degradation time. Film was degraded using an oxidative stress potential of +1.00 V.

5.2.8 Comparison figures

5.2.8.1 Optical and electrochemical characterisation

Table 5.19 – Comparison of maximum absorption wavelengths, HOMO energy levels as measured by CV, and HOMO energy levels as measured by CVA. Data for P3HT, PTTTz and PTTz is included from Chapter 4.

Polymer	Initial λ_{max} / nm	E_{HOMO} (CV)/ eV	E_{HOMO} (CVA)/ eV
Rr-P3HT	518	-4.80	-4.86
PTT	545	-5.03	-5.02
PDPP3Se	835	-5.03	-5.08
PTTTz	550	-5.12	-4.86
Ra-P3HT	440	-5.10	-5.10
PTB7	670	-5.15	-5.08
PTTz	546	-5.19	-4.96
SiIDT-BT	635	-5.38	-5.35
PCDTBT	575	-5.38	-5.42
IDFBT	546	-5.76	-4.74

5.2.8.2 Degradation

Table 5.20 – Comparison of degradation of polymer neat films after nearly 3 hours of oxidative stress (25%). Negative $\boldsymbol{\lambda_{shift}}$ values correspond to a blue-shift in absorption maxima. $\boldsymbol{\Delta E_{shift}}$ is the corresponding change in energy relating to the absorption maxima as derived in Chapter 4.4.

Polymer	$\boldsymbol{\lambda_{shift}}$ / nm	$\boldsymbol{\Delta E_{shift}}$/ meV	Change in Norm Abs at initial $\boldsymbol{\lambda_{shift}}$ / %
Rr-P3HT	-8	38	-12
PTT	-9	38	-11
PDPP3Se	-25	46	-19
PTTTz	-5	21	-14
Ra-P3HT	-10	66	-3
PTB7	-31	90	-25
PTTz	-16	69	-29
SiIDT-BT	-76	265	-67
PCDTBT	-54	224	-42
IDFBT	-39	175	-66

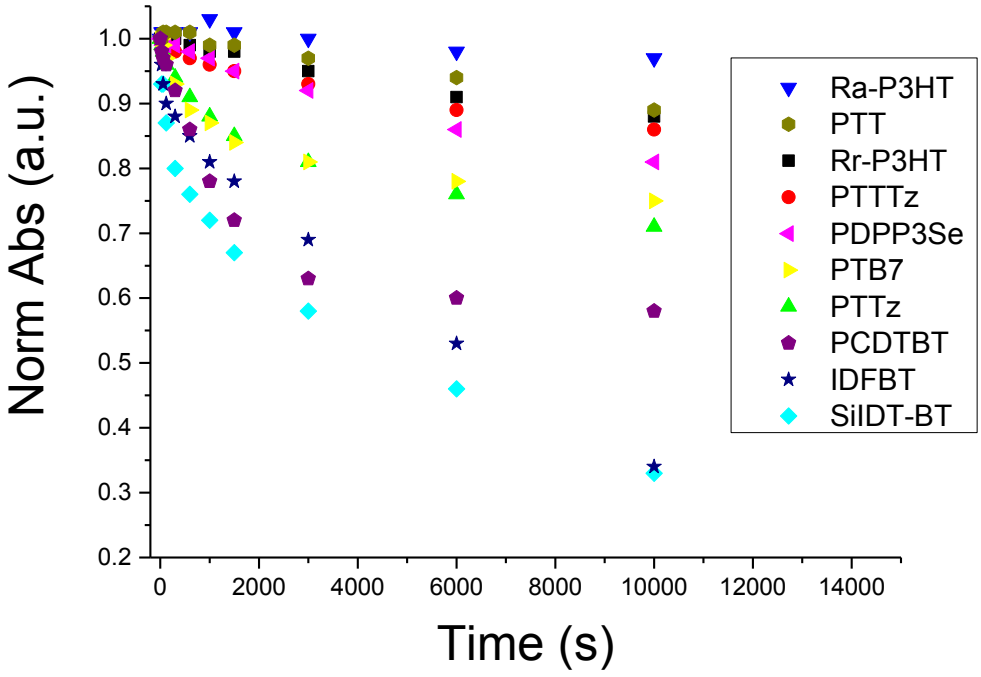

Figure 5.53 – Comparative plot of the normalised absorption at the initial absorption maxima wavelength as a function of oxidative stress time.

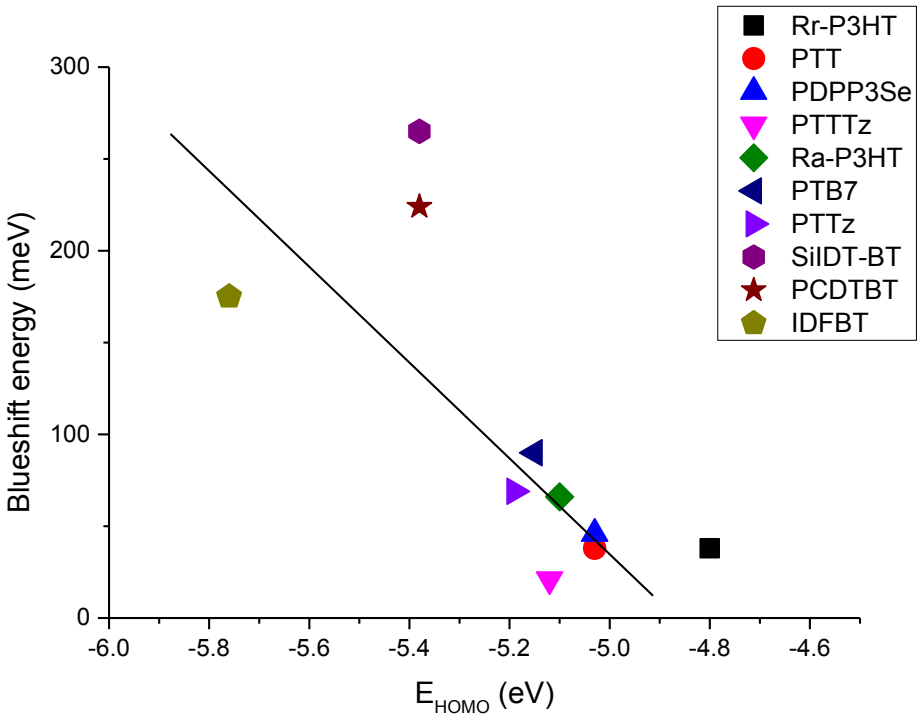

Figure 5.54 – Comparative plot showing the energy change in the peak absorption wavelength after nearly 3 hours of oxidative stress, plotted against polymer HOMO energy level.

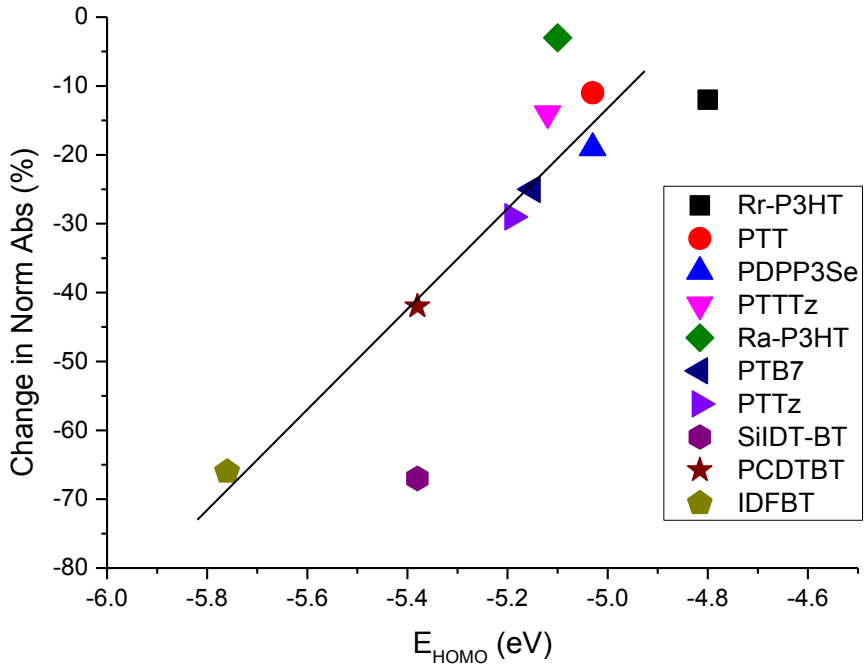

Figure 5.55 – Comparative plot of the percentage reduction in absorption intensity at the initial absorption maxima wavelength after nearly 3 hours of oxidative stress, plotted against polymer HOMO energy level.

5.3 Discussion

CV was successfully performed on neat films of polymers to determine HOMO energy levels of each polymer, as tabulated in Table 5.19. CV was largely in excellent agreement with CVA, with the exception of IDFBT. In this case two HOMO energy levels were estimated by CV as -5.43 eV and -5.76 eV; the former estimate is higher than expected for IDFBT[114], and was not observed in the CVA and so is ignored. CVA was successfully used to determine oxidative stress potentials that induced a relative degree of oxidation of 25% across the range of polymers. Chronoamperometry was then successfully used to apply 25% oxidative stress to a range of polymer films, allowing for ground state absorption spectra to be measured as a function of oxidative stress time, as described in Chapter 4.

Degradation due to the oxidative stress applied to polymer films was universally observed by a blue-shift and a reduction in absorption intensity of the absorption profile. Ra-P3HT was found to be one of the most stable polymers when an oxidative stress of 25% was applied, as evidenced by the 3% drop in absorption intensity at the initial absorption maximum wavelength, and a blue-shift of just 10 nm after 3 hours of degradation. In addition to 25% oxidative stress, Ra-P3HT was also subjected to 12% and 38% oxidative stress potentials. Interestingly, at the higher degree of oxidative stress Ra-P3HT was found to degrade to a similar extent as at 25% and 12%. At the other end of the scale, IDFBT was found to be one of the least stable polymers under oxidative stress of 25%, as evidenced by the 66% drop in absorption intensity at the initial absorption maximum wavelength, and the blue-shift of 39nm.

Figure 5.53 uses the drop in normalised absorption intensity at the initial absorption maximum wavelength as an indicator of degradation, and plots this parameter as a function of oxidative stress time for each polymer. The data refers only to films that have been subjected to a 25% oxidative stress. Each polymer appears to experience an exponential decay, which appears to tail off at longer oxidative stress times as the population of oxidisable polymer diminishes. The ordering of polymers in terms of degree of degradation roughly remains unchanged as a function of time, and is given after nearly 3 hours of oxidative stress as follows (ordered from most stable to least stable):

Ra-P3HT > **PTT** > **RrP3HT** > **PTTTz** > **PDPP3Se** > **PTB7** > **PTTz** > **PCDTBT** > **IDFBT** > **SiIDT-BT**

This trend in stability roughly follows the trend of HOMO energy level where the most stable polymers have the highest HOMO energy levels and the least stable polymers have the lowest HOMO energy levels. This trend is displayed in Figure 5.55 where the change in normalised absorption intensity at the initial absorption maximum wavelength after 3 hours oxidative stress is plotted against HOMO energy level for each polymer.

The blue-shift in absorption spectra can be explained partly by a lowering of the HOMO energy level. This lowering of the HOMO energy level is typical of conjugated systems with reduced conjugation length. We speculate that a chemical bond along the polymer backbone is broken, therefore disrupting conjugation and reducing conjugation length, thereby widening the optical bandgap, and thus lowering the HOMO. Since optical absorption is a vital function of semiconducting polymers used in organic solar cells, it

is interesting to note the change in energy corresponding to photon absorption at the polymer peak absorption wavelength, when comparing pristine and degraded films. This energy change is calculated before and after an oxidative stress was applied for nearly 3 hours for each film, and is plotted as a function of HOMO energy level in Figure 5.54. This change in energy is used as an indicator of degradation. A strong correlation is observed between HOMO energy level and stability, where polymers with high HOMOs are the most stable and polymers with the lowest HOMOs are the least stable.

This observation could have very important implications for design-rules relating to semiconducting polymer synthesis. Polymers with deep HOMO energy levels are widely considered desirable to prevent electrochemical degradation due to polymer oxidation in the presence of oxygen and/or water, thereby improving the stability of polymers under storage.[62] Based on the results presented in this thesis, this could have a detrimental effect on the stability of hole polaron species, and therefore on the lifetimes of devices that rely on the presence of hole polarons under operation. This consideration is anticipated to become increasingly relevant as encapsulation techniques improve, leading to more successful exclusion of oxygen and/or water.

References

(1) *Key World Energy Statistics 2014*, International Energy Agency, 2014.

(2) Bredas, J.-L. *Materials Horizons* **2014**, 17.

(3) Beatrup, D.; Wade, J.; Biniek, L.; Bronstein, H.; Hurhangee, M.; Kim, J.-S.; McCulloch, I.; Durrant, J. R. *Chemical Communications* **2014**, *50*, 14425.

(4) Fraunhofer Institute for Solar Energy Systems, I. *Photovoltaics Report*, 2016.

(5) *Heliatek consolidated its technology leadership by establishing a new world record for organic solar technology with a cell efficiency of 12%*, http://www.heliatek.com, 2013.

(6) Ito, T.; Shirakawa, H.; Ikeda, S. *Journal of Polymer Science: Polymer Chemistry Edition* **1974**, *12*, 11.

(7) Shirakawa, H.; Louis, E. J.; MacDiarmid, A. G.; Chiang, C. K.; Heeger, A. J. *Journal of the Chemical Society, Chemical Communications* **1977**, 578.

(8) Chiang, C. K.; Fincher, C. R.; Park, Y. W.; Heeger, A. J.; Shirakawa, H.; Louis, E. J.; Gau, S. C.; MacDiarmid, A. G. *Physical Review Letters* **1977**, *39*, 1098.

(9) Chiang, C. K.; Druy, M. A.; Gau, S. C.; Heeger, A. J.; Louis, E. J.; MacDiarmid, A. G.; Park, Y. W.; Shirakawa, H. *Journal of the American Chemical Society* **1978**, *100*, 1013.

(10) Weinberger, B. R.; Akhtar, M.; Gau, S. C. *Synthetic Metals* **1982**, *4*, 187.

(11) Karg, S.; Riess, W.; Dyakonov, V.; Schwoerer, M. *Synthetic Metals* **1993**, *54*, 427.

(12) Tang, C. W. *Applied Physics Letters* **1986**, *48*, 183.

(13) Yu, G.; Gao, J.; Hummelen, J. C.; Wudl, F.; Heeger, A. J. *Science* **1995**, *270*, 1789.

(14) Roncali, J. *Chemical Reviews* **1992**, *92*.

(15) He, Z.; Zhong, C.; Su, S.; Xu, M.; Wu, H.; Cao, Y. *Nat Photon* **2012**, *6*, 591.

(16) Nozawa, T. *Toray develops "thick" organic PV cell using polymer material*, Nikkei Technology - http://techon.nikkeibp.co.jp/english/NEWS_EN/20130925/305310/, 2013.

(17) Clarke, T. M.; Durrant, J. R. *Chemical Reviews* **2010**, *110*, 6736.

(18) Hains, A. W.; Liang, Z.; Woodhouse, M. A.; Gregg, B. A. *Chemical Reviews* **2010**, *110*, 6689.

(19) Sze, S. M. *Physics of semiconductor devices*; 2nd ed.; Wiley-Interscience: New York, 1981.

(20) Ohkita, H.; Cook, S.; Astuti, Y.; Duffy, W.; Tierney, S.; Zhang, W.; Heeney, M.; McCulloch, I.; Nelson, J.; Bradley, D. D. C.; Durrant, J. R. *Journal of the American Chemical Society* **2008**, *130*, 3030.

(21) Veldman, D.; İpek, Ö.; Meskers, S. C. J.; Sweelssen, J.; Koetse, M. M.; Veenstra, S. C.; Kroon, J. M.; Bavel, S. S. v.; Loos, J.; Janssen, R. A. J. *Journal of the American Chemical Society* **2008**, *130*, 7721.

(22) Guo, J.; Ohkita, H.; Benten, H.; Ito, S. *Journal of the American Chemical Society* **2010**, *132*, 6154.

(23) Clarke, T. M.; Ballantyne, A. M.; Tierney, S.; Heeney, M.; Duffy, W.; McCulloch, I.; Nelson, J.; Durrant, J. R. *The Journal of Physical Chemistry C* **2010**, *114*, 8068.

(24) Peumans, P.; Forrest, S. R. *Chemical Physics Letters* **2004**, *398*, 27.

(25) YOSHINO, F. W. C. M. W. W. W. H.-C. W. M.-X. K. *Acta Physica Sinica* **2001**, *50*, 1157.

(26) Sariciftci, N. S.; Smilowitz, L.; Heeger, A. J.; Wudl, F. *Science* **1992**, *258*, 1474.

(27) Ruseckas, A.; Theander, M.; Andersson, M. R.; Svensson, M.; Prato, M.; Inganäs, O.; Sundström, V. *Chemical Physics Letters* **2000**, *322*, 136.

(28) Ren, G.; Schlenker, C. W.; Ahmed, E.; Subramaniyan, S.; Olthof, S.; Kahn, A.; Ginger, D. S.; Jenekhe, S. A. *Advanced Functional Materials* **2013**, *23*, 1238.

(29) Bakulin, A. A.; Dimitrov, S. D.; Rao, A.; Chow, P. C. Y.; Nielsen, C. B.; Schroeder, B. C.; McCulloch, I.; Bakker, H. J.; Durrant, J. R.; Friend, R. H. *The Journal of Physical Chemistry Letters* **2013**, *4*, 209.

(30) Soon, Y. W.; Clarke, T. M.; Zhang, W.; Agostinelli, T.; Kirkpatrick, J.; Dyer-Smith, C.; McCulloch, I.; Nelson, J.; Durrant, J. R. *Chemical Science* **2011**, *2*, 1111.

(31) Loi, M. A.; Toffanin, S.; Muccini, M.; Forster, M.; Scherf, U.; Scharber, M. *Advanced Functional Materials* **2007**, *17*, 2111.

(32) Ohkita, H.; Cook, S.; Astuti, Y.; Duffy, W.; Heeney, M.; Tierney, S.; McCulloch, I.; Bradley, D. D. C.; Durrant, J. R. *Chemical Communications* **2006**, 3939.

(33) Yin, C.; Kietzke, T.; Neher, D.; Hörhold, H.-H. *Applied Physics Letters* **2007**, *90*, 092117.

(34) Benson-Smith, J. J.; Goris, L.; Vandewal, K.; Haenen, K.; Manca, J. V.; Vanderzande, D.; Bradley, D. D. C.; Nelson, J. *Advanced Functional Materials* **2007**, *17*, 451.

(35) Offermans, T.; van Hal, P. A.; Meskers, S. C. J.; Koetse, M. M.; Janssen, R. A. J. *Physical Review B* **2005**, *72*, 045213.

(36) Morteani, A. C.; Sreearunothai, P.; Herz, L. M.; Friend, R. H.; Silva, C. *Physical Review Letters* **2004**, *92*, 247402.

(37) Offermans, T.; Meskers, S. C. J.; Janssen, R. A. J. *Chemical Physics* **2005**, *308*, 125.

(38) McNeill, C. R.; Westenhoff, S.; Groves, C.; Friend, R. H.; Greenham, N. C. *The Journal of Physical Chemistry C* **2007**, *111*, 19153.

(39) Adams, D. M.; Brus, L.; Chidsey, C. E. D.; Creager, S.; Creutz, C.; Kagan, C. R.; Kamat, P. V.; Lieberman, M.; Lindsay, S.; Marcus, R. A.; Metzger, R. M.; Michel-Beyerle, M. E.; Miller, J. R.; Newton, M. D.; Rolison, D. R.; Sankey, O.; Schanze, K. S.; Yardley, J.; Zhu, X. *The Journal of Physical Chemistry B* **2003**, *107*, 6668.

(40) Deibel, C.; Strobel, T.; Dyakonov, V. *Advanced Materials* **2010**, *22*, 4097.

(41) Onsager, L. *Physical Review* **1938**, *54*, 554.

(42) Grancini, G.; Maiuri, M.; Fazzi, D.; Petrozza, A.; Egelhaaf, H. J.; Brida, D.; Cerullo, G.; Lanzani, G. *Nat Mater* **2013**, *12*, 29.

(43) Muntwiler, M.; Yang, Q.; Tisdale, W. A.; Zhu, X. Y. *Physical Review Letters* **2008**, *101*, 196403.

(44) Arkhipov, V. I.; Emelianova, E. V.; Bässler, H. *Physical Review Letters* **1999**, *82*, 1321.

(45) Zhu, X. Y.; Yang, Q.; Muntwiler, M. *Accounts of Chemical Research* **2009**, *42*, 1779.

(46) Hwang, I.-W.; Moses, D.; Heeger, A. J. *The Journal of Physical Chemistry C* **2008**, *112*, 4350.

(47) Bakulin, A. A.; Martyanov, D. S.; Paraschuk, D. Y.; Pshenichnikov, M. S.; van Loosdrecht, P. H. M. *The Journal of Physical Chemistry B* **2008**, *112*, 13730.

(48) Gulbinas, V.; Hertel, D.; Yartsev, A.; Sundström, V. *Physical Review B* **2007**, *76*, 235203.

(49) De, S.; Pascher, T.; Maiti, M.; Jespersen, K. G.; Kesti, T.; Zhang, F.; Inganäs, O.; Yartsev, A.; Sundström, V. *Journal of the American Chemical Society* **2007**, *129*, 8466.

(50) Turner, D. W. *German Bunsen Society for Physical Chemistry* **1970**, *75*, 181.

(51) Quinye Bao; Simone Fabiano; Fahlman, M. *Advanced Functional Materials* **2016**, *26*.

(52) Djurovich, P. *Organic Electronics* **2009**, *10*.

(53) Jørgensen, M.; Norrman, K.; Gevorgyan, S. A.; Tromholt, T.; Andreasen, B.; Krebs, F. C. *Advanced Materials* **2012**, *24*, 580.

(54) Tipnis, R.; Bernkopf, J.; Jia, S.; Krieg, J.; Li, S.; Storch, M.; Laird, D. *Solar Energy Materials and Solar Cells* **2009**, *93*, 442.

(55) Beaupre, S.; Leclerc, M. *Journal of Materials Chemistry A* **2013**, *1*, 11097.

(56) Peters, C. H.; Sachs-Quintana, I. T.; Kastrop, J. P.; Beaupré, S.; Leclerc, M.; McGehee, M. D. *Advanced Energy Materials* **2011**, *1*, 491.

(57) Zweibel, K. *Energy Policy* **2010**, *38*, 7519.

(58) Azzopardi, B.; Emmott, C. J. M.; Urbina, A.; Krebs, F. C.; Mutale, J.; Nelson, J. *Energy & Environmental Science* **2011**, *4*, 3741.

(59) Krebs, F. C. *Solar Energy Materials and Solar Cells* **2008**, *92*, 685.

(60) Lee, J. U.; Jung, J. W.; Jo, J. W.; Jo, W. H. *Journal of Materials Chemistry* **2012**, *22*, 24265.

(61) Hintz, H.; Egelhaaf, H. J.; Lüer, L.; Hauch, J.; Peisert, H.; Chassé, T. *Chemistry of Materials* **2011**, *23*, 145.

(62) de Leeuw, D. M.; Simenon, M. M. J.; Brown, A. R.; Einerhand, R. E. F. *Synthetic Metals* **1997**, *87*, 53.

(63) Li, W.; Katz, H. E.; Lovinger, A. J.; Laquindanum, J. G. *Chemistry of Materials* **1999**, *11*, 458.

(64) Lei, T.; Cao, Y.; Fan, Y.; Liu, C.-J.; Yuan, S.-C.; Pei, J. *Journal of the American Chemical Society* **2011**, *133*, 6099.

(65) Takeda, Y.; Andrew, T. L.; Lobez, J. M.; Mork, A. J.; Swager, T. M. *Angewandte Chemie International Edition* **2012**, *51*, 9042.

(66) Di Pietro, R.; Sirringhaus, H. *Advanced Materials* **2012**, *24*, 3367.

(67) Ruiz, V.; Colina, Á.; Heras, A.; López-Palacios, J. *Polymer Degradation and Stability* **2006**, *91*, 3117.

(68) Zoski, C. G.; Elsevier: 2007.

(69) Loo, Y.-L.; McCulloch, I. *MRS Bulletin* **2008**, *33*, 653.

(70) Subramanian, S.; Park, S. K.; Parkin, S. R.; Podzorov, V.; Jackson, T. N.; Anthony, J. E. *Journal of the American Chemical Society* **2008**, *130*, 2706.

(71) Li, G.; Shrotriya, V.; Huang, J.; Yao, Y.; Moriarty, T.; Emery, K.; Yang, Y. *Nature Materials* **2005**, *4*, 864.

(72) Yang, H.; Shin, T. J.; Yang, L.; Cho, K.; Ryu, C. Y.; Bao, Z. *Advanced Functional Materials* **2005**, *15*, 671.

(73) Erb, T.; Zhokhavets, U.; Gobsch, G.; Raleva, S.; Stühn, B.; Schilinsky, P.; Waldauf, C.; Brabec, C. J. *Advanced Functional Materials* **2005**, *15*, 1193.

(74) Clarke, T. M.; Ballantyne, A. M.; Nelson, J.; Bradley, D. D. C.; Durrant, J. R. *Advanced Functional Materials* **2008**, *18*, 4029.

(75) Chang, J.-F.; Sun, B.; Breiby, D. W.; Nielsen, M. M.; Sölling, T. I.; Giles, M.; McCulloch, I.; Sirringhaus, H. *Chemistry of Materials* **2004**, *16*, 4772.

(76) Masubuchi, S.; Kazama, S. *Synthetic Metals* **1995**, *74*, 151.

(77) Sirringhaus, H.; Brown, P. J.; Friend, R. H.; Nielsen, M. M.; Bechgaard, K.; Langeveld-Voss, B. M. W.; Spiering, A. J. H.; Janssen, R. A. J.; Meijer, E. W.; Herwig, P.; de Leeuw, D. M. *Nature* **1999**, *401*, 685.

(78) Sirringhaus, H.; Brown, P. J.; Friend, R. H.; Nielsen, M. M.; Bechgaard, K.; Langeveld-Voss, B. M. W.; Spiering, A. J. H.; Janssen, R. A. J.; Meijer, E. W. *Synthetic Metals* **2000**, *111–112*, 129.

(79) McCulloch, I.; Heeney, M.; Bailey, C.; Genevicius, K.; MacDonald, I.; Shkunov, M.; Sparrowe, D.; Tierney, S.; Wagner, R.; Zhang, W.; Chabinyc, M. L.; Kline, R. J.; McGehee, M. D.; Toney, M. F. *Nature Materials* **2006**, *5*, 328.

(80) Zhang, R.; Li, B.; Iovu, M. C.; Jeffries-El, M.; Sauvé, G.; Cooper, J.; Jia, S.; Tristram-Nagle, S.; Smilgies, D. M.; Lambeth, D. N.; McCullough, R. D.; Kowalewski, T. *Journal of the American Chemical Society* **2006**, *128*, 3480.

(81) Lunt, R. R.; Benziger, J. B.; Forrest, S. R. *Advanced Materials* **2010**, *22*, 1233.

(82) Renz, J. A.; Ashraf, R. S.; Erb, T.; Shokhovets, S.; Gobsch, G.; Klemm, E.; Hoppe, H. *Macromolecular Chemistry and Physics* **2010**, *211*, 1689.

(83) Chen, H.; Hsiao, Y.-C.; Hu, B.; Dadmun, M. *Journal of Materials Chemistry A* **2014**, *2*, 9883.

(84) Zhang, S.; Ye, L.; Wang, Q.; Li, Z.; Guo, X.; Huo, L.; Fan, H.; Hou, J. *The Journal of Physical Chemistry C* **2013**, *117*, 9550.

(85) Jamieson, F. C.; Domingo, E. B.; McCarthy-Ward, T.; Heeney, M.; Stingelin, N.; Durrant, J. R. *Chemical Science* **2012**, *3*, 485.

(86) Mihailetchi, V. D.; Koster, L. J. A.; Blom, P. W. M.; Melzer, C.; de Boer, B.; van Duren, J. K. J.; Janssen, R. A. J. *Advanced Functional Materials* **2005**, *15*, 795.

(87) Rance, W. L.; Ferguson, A. J.; McCarthy-Ward, T.; Heeney, M.; Ginley, D. S.; Olson, D. C.; Rumbles, G.; Kopidakis, N. *ACS Nano* **2011**, *5*, 5635.

(88) Keivanidis, P. E.; Clarke, T. M.; Lilliu, S.; Agostinelli, T.; Macdonald, J. E.; Durrant, J. R.; Bradley, D. D. C.; Nelson, J. *The Journal of Physical Chemistry Letters* **2010**, *1*, 734.

(89) Sweetnam, S.; Graham, K. R.; Ngongang Ndjawa, G. O.; Heumüller, T.; Bartelt, J. A.; Burke, T. M.; Li, W.; You, W.; Amassian, A.; McGehee, M. D. *Journal of the American Chemical Society* **2014**, *136*, 14078.

(90) Peet, J.; Heeger, A. J.; Bazan, G. C. *Accounts of Chemical Research* **2009**, *42*, 1700.

(91) Thompson, B. C.; Fréchet, J. M. J. *Angewandte Chemie International Edition* **2008**, *47*, 58.

(92) Osaka, I.; McCullough, R. D. *Accounts of Chemical Research* **2008**, *41*, 1202.

(93) McCullough, R. D. *Advanced Materials* **1998**, *10*, 93.

(94) Wang, G.; Swensen, J.; Moses, D.; Heeger, A. J. *Journal of Applied Physics* **2003**, *93*, 6137.

(95) Padinger, F.; Rittberger, R. S.; Sariciftci, N. S. *Advanced Functional Materials* **2003**, *13*, 85.

(96) Ma, W.; Yang, C.; Gong, X.; Lee, K.; Heeger, A. J. *Advanced Functional Materials* **2005**, *15*, 1617.

(97) Ho, V.; Boudouris, B. W.; Segalman, R. A. *Macromolecules* **2010**, *43*, 7895.

(98) Boudouris, B. W.; Ho, V.; Jimison, L. H.; Toney, M. F.; Salleo, A.; Segalman, R. A. *Macromolecules* **2011**, *44*, 6653.

(99) Swenberg, M. P. a. C. E. *Electronic Processes in Organic Crystals*; Clarendon, Oxford, 1982Cl.

(100) Chen, T. A. *Journal of the American Chemical Society* **1995**, *117*.

(101) Shrotriya, V.; Ouyang, J.; Tseng, R. J.; Li, G.; Yang, Y. *Chemical Physics Letters* **2005**, *411*, 138.

(102) Jiang, X. M.; Österbacka, R.; Korovyanko, O.; An, C. P.; Horovitz, B.; Janssen, R. A. J.; Vardeny, Z. V. *Advanced Functional Materials* **2002**, *12*, 587.

(103) Chen, T.-A.; Wu, X.; Rieke, R. D. *Journal of the American Chemical Society* **1995**, *117*, 233.

(104) Brown, P. J.; Thomas, D. S.; Köhler, A.; Wilson, J. S.; Kim, J.-S.; Ramsdale, C. M.; Sirringhaus, H.; Friend, R. H. *Physical Review B* **2003**, *67*, 064203.

(105) Lee, J.; Chung, J. W.; Jang, J.; Kim, D. H.; Park, J.-I.; Lee, E.; Lee, B.-L.; Kim, J.-Y.; Jung, J. Y.; Park, J. S.; Koo, B.; Jin, Y. W.; Kim, D. H. *Chemistry of Materials* **2013**, *25*, 1927.

(106) Guo, X.; Quinn, J.; Chen, Z.; Usta, H.; Zheng, Y.; Xia, Y.; Hennek, J. W.; Ortiz, R. P.; Marks, T. J.; Facchetti, A. *Journal of the American Chemical Society* **2013**, *135*, 1986.

(107) Lin, Y.; Fan, H.; Li, Y.; Zhan, X. *Advanced Materials* **2012**, *24*, 3087.

(108) Bronstein, H.; Hurhangee, M.; Fregoso, E. C.; Beatrup, D.; Soon, Y. W.; Huang, Z.; Hadipour, A.; Tuladhar, P. S.; Rossbauer, S.; Sohn, E.-H.; Shoaee, S.; Dimitrov, S. D.; Frost, J. M.; Ashraf, R. S.; Kirchartz, T.; Watkins, S. E.; Song, K.; Anthopoulos, T.; Nelson, J.; Rand, B. P.; Durrant, J. R.; McCulloch, I. *Chemistry of Materials* **2013**, *25*, 4239.

(109) Kim, Y.; Cook, S.; Tuladhar, S. M.; Choulis, S. A.; Nelson, J.; Durrant, J. R.; Bradley, D. D. C.; Giles, M.; McCulloch, I.; Ha, C.-S.; Ree, M. *Nature Materials* **2006**, *5*, 197.

(110) Loewe, R. S.; Ewbank, P. C.; Liu, J.; Zhai, L.; McCullough, R. D. *Macromolecules* **2001**, *34*, 4324.

(111) Ashraf, R. S.; Chen, Z.; Leem, D. S.; Bronstein, H.; Zhang, W.; Schroeder, B.; Geerts, Y.; Smith, J.; Watkins, S.; Anthopoulos, T. D.; Sirringhaus, H.; de Mello, J. C.; Heeney, M.; McCulloch, I. *Chemistry of Materials* **2011**, *23*, 768.

(112) Bronstein, H.; Leem, D. S.; Hamilton, R.; Woebkenberg, P.; King, S.; Zhang, W.; Ashraf, R. S.; Heeney, M.; Anthopoulos, T. D.; Mello, J. d.; McCulloch, I. *Macromolecules* **2011**, *44*, 6649.

(113) Shahid, M.; McCarthy-Ward, T.; Labram, J.; Rossbauer, S.; Domingo, E. B.; Watkins, S. E.; Stingelin, N.; Anthopoulos, T. D.; Heeney, M. *Chemical Science* **2012**, *3*, 181.

(114) Kirkpatrick, J.; Nielsen, C. B.; Zhang, W.; Bronstein, H.; Ashraf, R. S.; Heeney, M.; McCulloch, I. *Advanced Energy Materials* **2012**, *2*, 260.

Conclusions

Cyclic voltammetry has been employed to measure the HOMO energy level of crystalline/aggregate and amorphous domains in neat films of P3EHT. An energy offset of 60 meV was observed, which is thought to be significant as it might provide a thermodynamic driving force for the movement of hole polarons from less-ordered amorphous domains to more ordered crystalline/aggregate domains. This could be an important effect in polymer/fullerene solar cells as it might lead to better charge separation, less recombination, and therefore enhanced charge collection.

A new methodology, based on well-established electrochemical techniques (cyclic voltammetry and chronoamperometry) has been developed for the measurement and comparison of stability of the hole polaron species in different semiconducting polymer films. This methodology has been used to study the stability of a range of polymers subjected to similar degrees of oxidative stress. A correlation between HOMO energy level and polaron stability has been established; lowering the HOMO energy level of a polymer results in a less stable, more oxidising hole polaron species, which causes the polymer to undergo electrochemical degradation. We speculate that this degradation is due to reaction between the electron-deficient hole polaron and a source of electrons, which might be from some impurity, or from an unoxidised segment of polymer.